

The Use of Synchrotron Radiation to study Overgrowth Phenomena in InAs/GaAs Nanostructures

Dissertation der Fakultät für Physik
der
Ludwig-Maximilians-Universität München

Michael Sztucki



München 2004

The Use of Synchrotron Radiation to study Overgrowth Phenomena in InAs/GaAs Nanostructures

Dissertation der Fakultät für Physik
der
Ludwig–Maximilians–Universität München

vorgelegt von
Michael Sztucki
aus Augsburg

München, den 14. Februar 2004

Erstgutachter: Prof. Dr. Jörg P. Kotthaus
Zweitgutachter: Prof. Dr. Joachim Rädler
Tag der mündlichen Prüfung: 24. Juni 2004

Contents

Contents	v
Abstract	ix
Zusammenfassung	xi
1 Introduction	1
2 Background	7
2.1 Contrast variation by anomalous diffraction	7
2.1.1 Superstructure reflections	7
2.1.2 “Anomalous” scattering	9
2.1.3 Contrast variation	10
2.2 Experimental set-up	15
2.2.1 Beamline ID1	15
2.2.2 X-Ray Diffraction (XRD)	19
2.2.3 Grazing Incidence Diffraction (GID)	20
2.2.4 Grazing Incidence Small Angle Scattering (GISAXS)	24
2.3 Finite-Element Method (FEM)	24
2.3.1 Theory of elasticity	25
2.3.2 Finite-element technique	27
2.3.3 Example using Patran/Nastran	30
3 Quantum dots	37
3.1 Motivation	37

3.2	Atomic Force Microscopy	38
3.2.1	Experiment	38
3.2.2	Discussion	41
3.3	Grazing incidence diffraction	42
3.3.1	Contrast variation by anomalous diffraction	42
3.3.2	Shape determination from angular measurements	45
3.3.3	Towards the limits of the contrast variation technique	47
3.3.4	Discussion	48
4	Quantum rings	53
4.1	Motivation	54
4.1.1	Self-organised growth of quantum rings	54
4.1.2	Growth mechanisms	55
4.1.3	Investigated samples	59
4.2	Experiment	60
4.2.1	Atomic Force Microscopy	60
4.2.2	Grazing incidence small angle scattering (GISAXS)	63
4.2.3	Grazing incidence diffraction (GID)	67
4.3	Finite-element simulation of the GID data	72
4.4	Evaluation and discussion	74
5	Cleaved Edge Overgrowth (CEO)	85
5.1	Motivation	85
5.1.1	Technique	86
5.1.2	T-shaped quantum wires	87
5.1.3	Self-organised ordering of quantum dots	92
5.2	Experiment	93
5.3	Evaluation and discussion	101
6	General conclusions and outlook	109

A Useful formulae	111
B List of tables	113
C List of figures	115
Bibliography	121
Acknowledgements	133

Abstract

This work focuses on the investigation of overgrowth phenomena in InAs/GaAs nanostructures using synchrotron radiation. Surface-sensitive grazing incidence small angle x-ray scattering (GISAXS) and grazing incidence diffraction (GID) are applied to study shape, strain, and interdiffusion in self-organised grown nanostructures. The technique of anomalous x-ray diffraction at the weak (200) superstructure reflection enhances the chemical sensitivity of the measurements. For the investigation of (partially) buried nanostructures finite-element simulations (FEM) have been performed. The following sample systems were investigated:

Free-standing and buried $\text{In}_{0.5}\text{Ga}_{0.5}\text{As}$ quantum dots

Free-standing $\text{In}_x\text{Ga}_{1-x}\text{As}$ islands grown on GaAs (001) by molecular beam epitaxy (MBE) with a nominal concentration of $x = 0.5$ have been investigated. Contrast variation close to the K edge of As by anomalous GID at the (200) superstructure reflection is used for a direct determination of the InAs concentration as a function of the lateral strain in the quantum dots (QDs). The evaluation of intensity mappings recorded in reciprocal space close to the (200) reflection together with atomic force micrographs (AFM) allows to attribute the strain and the InAs concentration to a certain height in the quantum dots. Thereby, a three-dimensional model of the strain and interdiffusion profile of the InGaAs QDs can be reconstructed. A discussion of measurements taken on buried $\text{In}_{0.5}\text{Ga}_{0.5}\text{As}$ QDs and free-standing islands grown on the strain modulated surface of a buried QD layer shows the limits of this technique.

InGaAs quantum rings

The formation of nanoscopic InGaAs ring structures on a GaAs (001) substrate takes place when InAs quantum dots, grown by Stranski-Krastanov self-organisation, are covered by a thin layer of GaAs. The shape transformation into rings is governed by strain, diffusion and surface tension, quantities which are of importance to understand magneto-optical and electronic applications of the rings. GISAXS and GID is applied to characterise morphology and structural properties such as strain and chemical composition of the rings in three dimensions. From GISAXS the shape is found to be of circular symmetry with an outer radius of 26nm, a height of 1.5nm, and a hole in the middle, in good agreement with AFM measurements. The most surprising results are obtained from intensity mappings in reciprocal space close to the (220) and (2 $\bar{2}$ 0) reflection done in surface sensitive GID geometry. From a comparison of the intensity maps with FEM model calculations the InGaAs interdiffusion profile in the ring is determined. It strongly depends on the crystallographic orientation. In the ring a maximum InAs concentration of more than 80% along $[1\bar{1}0]$ is found while along $[110]$ it is below 20%. This is explained by the preferred diffusion of In along $[1\bar{1}0]$.

Quantum wires formed by cleaved edge overgrowth

Quantum wires (QWRs) fabricated by the cleaved edge overgrowth (CEO) technique use tensile strain to confine the charge carriers to one dimension. The cleaved edge of a pseudomorphically strained $\text{In}_{0.1}\text{Al}_{0.9}\text{As}/\text{Al}_{0.33}\text{Ga}_{0.67}\text{As}$ superlattice (SL) is overgrown by a GaAs layer of 10nm thickness. The lateral charge carrier localisation in the overgrown layer is induced by the periodic strain modulation of the SL. Using GID this strain state of the system is determined. The strain modulation due to the overgrown superlattice occurs only within $3\mu\text{m}$ of the total wafer thickness of $150\mu\text{m}$. The GID technique allows for a clear separation of the strain modulation in the cap layer and the superlattice underneath. It can be proved that the strain modulation in the GaAs cap layer is not of compositional origin but purely elastic with an average lattice parameter change of $(0.8 \pm 0.1)\%$ with respect to relaxed GaAs. The strain profile obtained is confirmed by FEM model calculations.

Zusammenfassung

Die vorliegende Arbeit befasst sich mit methodischen Entwicklungen zur Untersuchung von Strukturänderungen beim Überwachsen von InAs/GaAs Nanostrukturen mittels Synchrotronstrahlung. Die oberflächenempfindlichen Methoden der Röntgen-Kleinwinkelstreuung (GISAXS) und der Röntgenbeugung unter streifendem Einfall (GID) ermöglichen es, Form, Verspannung und Interdiffusion in selbst-organisierten Nanostrukturen zu studieren. Die Methode der anomalen Röntgenbeugung am schwachen (200) Überstruktureflex erhöht die chemische Empfindlichkeit der Messungen. Zur Untersuchung von (teilweise) vergrabenen Nanostrukturen wurden Finite-Elemente-Simulationsrechnungen (FEM) durchgeführt. Im Einzelnen wurden folgende Probensysteme untersucht:

Freistehende und vergrabene $\text{In}_{0.5}\text{Ga}_{0.5}\text{As}$ Quantenpunkte

Anomale Röntgenbeugung am (200) Überstruktureflex wurde zur Charakterisierung von freistehenden $\text{In}_{0.5}\text{Ga}_{0.5}\text{As}$ Inseln, hergestellt mittels Molekularstrahlepitaxie (MBE), verwendet. Durch die Kontrastvariationsmessungen nahe der K Absorptionskante von As kann die InAs Konzentration direkt als Funktion des lateralen Gitterparameters der Quantenpunkte bestimmt werden. Die Auswertung von 2D-Kartierungen des reziproken Raumes nahe des (200) Reflexes zusammen mit Rasterkraftmikroskopie ermöglichen es, den lateralen Gitterparameter sowie die InAs Konzentration einer bestimmten Höhe im Quantenpunkt zuzuordnen. Daraus lässt sich ein 3D-Modell des Verspannungs- und Interdiffusionsprofils der InGaAs Inseln rekonstruieren. Bei der Untersuchung von vergrabenen $\text{In}_{0.5}\text{Ga}_{0.5}\text{As}$ Quantenpunkten und von freistehenden Inseln, die auf der verspannten Oberfläche einer vergrabenen Schicht von Quantenpunkten gewachsen wurden, stößt diese Methode jedoch an ihre Grenzen.

InGaAs Quantenringe

Die Bildung von nanoskopischen InGaAs Ringen auf einer GaAs (001) Oberfläche wird beobachtet, wenn InAs Inseln, hergestellt mittels Stranski-Krastanov-Selbstorganisation, mit einer dünnen Schicht GaAs überwachsen werden. Die Oberflächenmorphologie und strukturelle Eigenschaften, wie Verspannung und chemische Zusammensetzung, dieser Strukturen wurde mittels GISAXS und GID analysiert. Gemäss der GISAXS-Auswertung, die gut mit den AFM Untersuchungen übereinstimmt, besitzen die Ringe eine kreisförmige Symmetrie mit einem äußeren Radius von 26nm und einer Höhe von 1.5nm. Das überraschendste Ergebnis liefert die Analyse von Kartierungen des reziproken Raums in der Nähe des (220) and ($2\bar{2}0$) Reflexes in GID-Geometrie. Die chemische Zusammensetzung des Rings, die durch den Vergleich der Messungen mit Modellrechnungen basierend auf FEM-Simulationen bestimmt wurde, hängt sehr stark von der kristallographischen Orientierung ab. In $[1\bar{1}0]$ Richtung wird eine maximale InAs Konzentration von über 80% beobachtet, während in $[110]$ Richtung diese unter 20% liegt. Die erhöhte Diffusion von In in $[1\bar{1}0]$ Richtung erklärt diese Beobachtung.

Quantendrähte hergestellt auf überwachsenen Spaltflächen

Die (110) Spaltfläche eines pseudomorph verspannten $\text{In}_{0.1}\text{Al}_{0.9}\text{As}/\text{Al}_{0.33}\text{Ga}_{0.67}\text{As}$ Übergitters wurde mit einer 10nm dicken Schicht GaAs überwachsen. In diesem Fall wird die Beweglichkeit der Ladungsträger in der überwachsenen Schicht lateral durch die periodische, tensile Verspannung des Übergitters auf eine Dimension beschränkt (Quantendraht). Mittels GID lässt sich die Verspannungsmodulation, die nur innerhalb von $3\mu\text{m}$ der Gesamtdicke des Wafers von $150\mu\text{m}$ auftritt, quantisieren [im Mittel $(0.8 \pm 0.1)\%$]. Hierbei erlaubt GID eine klare Trennung der Verspannungsmodulation in der überwachsenen Schicht vom darunterliegenden Übergitter. Es kann gezeigt werden, dass die Verspannungsmodulation in der überwachsenen GaAs Schicht rein elastischer Natur ist und keine Interdiffusion stattfindet. Das Verspannungsprofil lässt sich durch FEM-Modellrechnungen bestätigen.

Chapter 1

Introduction

Quantum confinement

The key to the rapid developments in microelectronics, in particular computer technology, is the ongoing trend towards *miniaturisation*. Following *Moore's Law* the lithographic feature sizes approach a dimension comparable with the *de-Broglie* wavelength of electrons where quantisation effects become important.

The latest generation of electronic devices uses already nanostructures where the charge carriers are confined to a length scale in the order of the electron de-Broglie wavelength. A well known example is the semiconductor laser, to be found in every CD and DVD player, which is based on quantum well structures.

In general, the reduction of dimensionality in quantum wells (QWs), quantum wires (QWRs), and quantum dots (QDs) results from the carrier localisation (quantum confinement) in one, two, and three dimensions, respectively. The typical length scale of a QD, for example, is in the range of 100\AA .

The reduced dimensionality results in a significant change of the electronic properties (see Fig. 1.1). While in three dimensions the electronic density of states of free electrons has a \sqrt{E} dependence, the density changes to a step function in 2D and a $1/\sqrt{E}$ dependence in 1D. Quantum

dots with charge carrier confinement to 0D have δ -function-like electronic states. Due to these atom-like discrete energy levels QDs are often called "artificial atoms". Their particular electronic and optical properties will be applied, e.g., in single electron transistors [Ishikuro97], storage devices [Okada01], QD lasers [Bimberg98], or even quantum computing [Loss98].

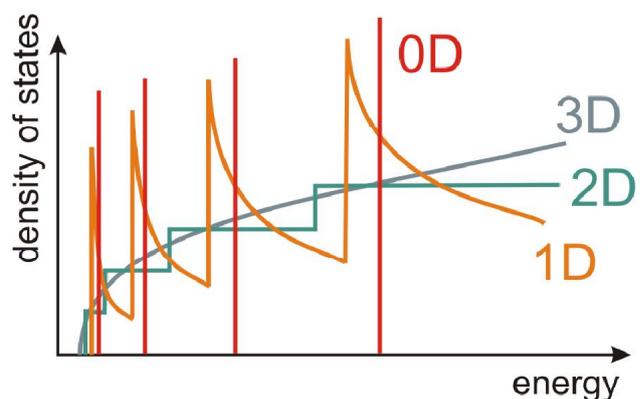


Figure 1.1: Electronic density of states when the dimensionality is varied from 3D to 0D, assuming free electrons.

GaAs/AIAs/InAs material system

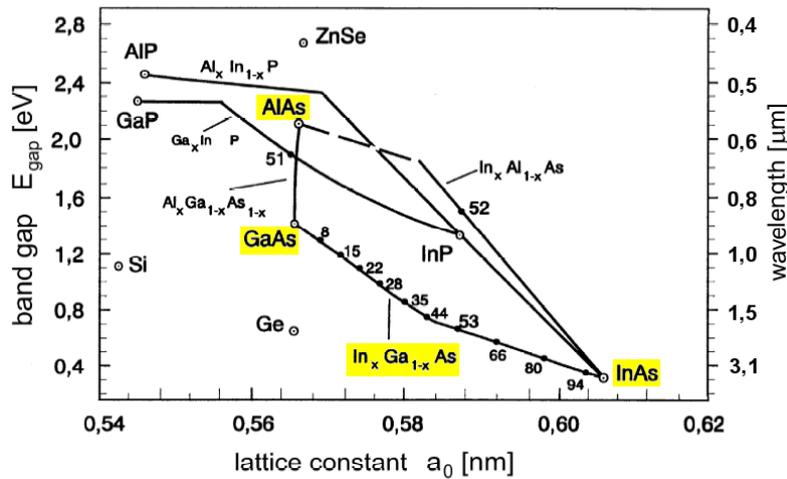


Figure 1.2: Band gaps and lattice constants of selected semiconductors at 300K.

Pseudobinary III-V compound semiconductors like $\text{Al}_x\text{Ga}_{1-x}\text{As}$, $\text{In}_x\text{Al}_{1-x}\text{As}$, and $\text{In}_x\text{Ga}_{1-x}\text{As}$ are important materials as their band gap can easily be tailored by changing the composition x in order to meet requirements for a specific application. E.g. laser diodes emitting at a particular wavelength can be fabricated. Fig. 1.2 shows the band gaps and lattice constants of selected semiconductors at 300K. GaAs and AlAs show good lattice matching, while the lattice mismatch between InAs and GaAs is about 7%. The lattice constant of alloys can linearly be approximated according to *Vegard's Law* [Vegard21].

Fabrication of nanostructures

While quantum wells are fabricated by growing superlattices with a sufficiently small individual layer thickness (smaller than the carrier de-Broglie wavelength) under conditions that guarantee smooth interfaces (e.g. MBE growth), for the fabrication of quantum wires and dots a lateral structuring on the nanometre scale is needed. The accuracy of the required surface structures with lateral dimensions of less than 100nm is beyond the capabilities of conventional lithography but can be realised by advanced lithographic techniques, like electron beam lithography, x-ray lithography, or focused ion beams. However, the disadvantage of these techniques is the high number of technological processes involved and the sequential processing of the structures. In addition, patterning by these techniques often results in imperfect interfaces which affect the optical properties of these structures, leading to radiationless recombination of excitons, for example. Atomically flat interfaces are required, e.g. to prevent a broadening of photoluminescence (PL) linewidths.

An alternative method for the formation of quantum dots is given by strained-layer heteroepitaxy.

Strained-layer heteroepitaxy

Commonly the growth modes in strained-layer heteroepitaxy are classified by thermodynamic arguments in three groups. **Layer-by-layer growth**, also called **Frank-van der Merwe growth** [Frank49], occurs if the sum of the surface free energy of the epitaxial film and the free energy of the film/substrate interface is smaller than the surface free energy of the substrate. In the opposite case **three-dimensional islands growth**, also called **Volmer-Weber growth** [Volmer26], is observed.

In the intermediate case one or several monolayers grow in the layer-by-layer mode forming the so-called *wetting layer* before the formation of 3D islands starts. This growth is called **Stranski-Krastanov mode** [Stranski38].

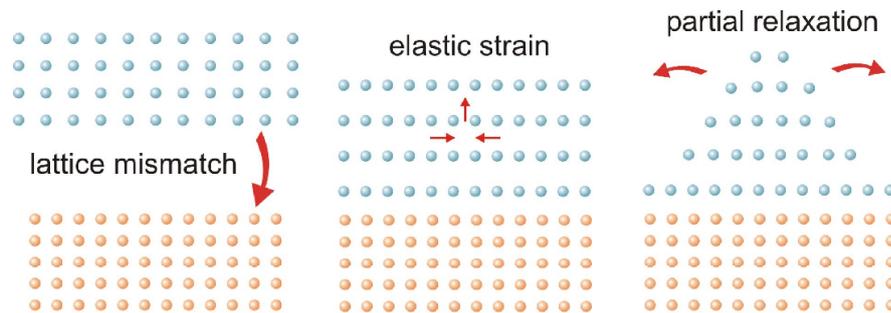


Figure 1.3: Schematic illustration of strain relief in Stranski-Krastanov growth. (*left*) The lattice constant of the film exceeds that of the substrate (7% in the case of InAs growth on GaAs). (*middle*) The pseudomorphic growth of a tetragonally distorted smooth wetting layer occurs. (*right*) After a certain number of smooth layers the formation of coherently strained 3D islands is observed. The arrows indicate the direction of elastic strain relief.

In the presence of lattice mismatch (see Fig. 1.3) strain builds up during the epitaxial film growth. The first monolayers of the lattice mismatched film grow with the lateral lattice constant of the substrate (pseudomorphic growth). In the case of InAs growth on GaAs the lattice constant of the substrate is 7% smaller than that of the film, resulting in compressive lateral strain. This strain is partly relieved vertically by tetragonal distortion of the lattice. However, in this strained wetting layer the elastic energy increases with the film thickness. After a certain number of smooth layers, depending on the given misfit, the elastic energy stored in the growing pseudomorphic layer is released by the creation of bumps on the surface (Asaro-Tiller-Grinfeld instability [Asaro72, Grinfeld86, Srolovitz89]). The resulting increase of the surface energy is overcompensated by a decrease of the strain energy due to the elastic strain relaxation towards the bulk lattice constant in the upper part of the 3D islands. If even this mechanism is no longer sufficient to relieve the strain during the growth, plastic strain relief sets in by introducing misfit dislocations.

The advantage of this self-organised bottom-up growth versus lithographic top-down methods are the very small achievable sizes and usually dislocation free structures which can be fabricated in a cost-efficient way. However, a possible size and shape distribution degrades the optoelectronic properties of QD based devices. A random arrangement of the QDs prevents their application in data storage or switching devices.

Cleaved edge overgrowth (CEO)

Cleaved edge overgrowth [Pfeiffer90], a molecular beam epitaxy (MBE) technique that uses high-quality overgrowth on the cleaved edge of a sample, has proven to be a powerful technique for the fabrication of T-shaped QWRs which form at the intersection of two QWs [Chang85, Gōni92]. The formation of QDs at the juncture of three QWs by two-fold cleaved edge overgrowth is possible, as well [Grundmann97, Wegscheider97b, Wegscheider97c, Wegscheider98]. The CEO technique uses the atomic precision of MBE and allows to produce QWRs with a thickness of only a few atomic layers. A further development of the T-shaped QWRs, as proposed by [Regelman99] and theoretically calculated by [Grundmann00], are purely strain modulated quantum wires. In this case the cleaved edge of a multilayer heterostructure acts as a substrate with an in-plane modulated lattice constant. This gives rise to a periodic strain modulation in the epitaxial layer grown on the cleaved edge. This strain modulation can be used to control size and position of Stranski-Krastanov grown islands on the cleaved edge, as well [Arai97a, Usami98].

Buried nanostructures

For all technological application the nanostructures have to be overgrown. As the growth of quantum dots is a process far from thermodynamic equilibrium further interdiffusion through the island surface takes place when the islands are capped. This results in a change of the island shape and their chemical composition [Liu00].

Interesting nanostructures which form during capping of InAs quantum dots with a thin layer of GaAs are *quantum rings* [Garcia97]. These structures are nowadays systematically fabricated as they show interesting magneto-optical and electronic properties [Lorke03].

More information about nanostructures which exceed the scope of this short introduction can be found in excellent reviews and textbooks.

A recent review on self-organisation of nanostructures in semiconductor heteroepitaxy has been published by C. Teichert [Teichert02]. The focus of this work is on experimental results for the growth of SiGe alloys on Si(001), but also examples for nanostructure formation in III-V, II-VI, and IV-VI heteroepitaxial systems are presented.

An overview about nanostructured materials, their synthesis, and optoelectronic applications has been given by P. Moriarty [Moriarty01].

A comprehensive report on applications and physical properties of semiconductor quantum dots is published in the book "Quantum dot heterostructures" by D. Bimberg [Bimberg98].

Investigation methods

A detailed knowledge about structural parameters like size, shape, strain, and chemical composition is required for a better understanding and finally a good predictability of optoelectronic properties of nanostructures produced by CEO or self-organisation. In addition, the structural changes during the overgrowth of the objects is of importance.

Diffuse x-ray scattering is the only method that can yield all this information. Within this thesis *grazing incidence diffraction* (GID) and *grazing incidence small angle x-ray scattering* (GISAXS) has been applied. GID has the advantage of being depth sensitive and improving the ratio of scattered radiation from the nanostructures and from the substrate due to the low incident angles. Measuring under grazing incidence *and* grazing exit angles only the in-plane lattice parameters of the structures can be investigated, which leaves the question ambiguous whether a certain in-plane lattice parameter results from relaxation or composition.

This problem can be solved by performing asymmetrical x-ray diffraction under grazing incidence and large exit angles [Stangl01, Hesse02]. The finite vertical momentum transfer Q_z makes the geometry sensitive for vertical strain components. In this case, the composition of an alloy is determined from the equilibrium lattice constant by comparing the measured lateral and vertical lattice strain assuming a tetragonal distortion of the cubic lattice in case of the (001) surface [Schüllli03b]. However, this technique is only applicable for isotropic materials if hydrostatic compression of the structure can be excluded.

Another possibility to reconstruct the composition profile offers the chemical sensitivity of *anomalous x-ray diffraction* which will be discussed in the following in more detail. Complementary information about the sample surface is gained by applying the locally resolving *atomic force microscopy* (AFM).

For the interpretation of the GID data measured on InGaAs nanostructures the technique of *Iso-Strain Scattering (ISS)* [Kegel01] is used. However, this technique works only for *free-standing* quantum dots where the vertical lattice relaxation is a *monotonic function* of height in the dots. Especially buried structures cannot be evaluated with this technique.

Therefore, numerical simulations of the elastic strains and displacement fields in the nanostructures are needed for the interpretation of the measured data. Within this thesis the method of *finite-element calculations* (FEM) has been applied. Using Fourier transformation techniques, the simulated displacements in the nanostructures are converted into reciprocal space maps and compared to the measured data. In an iterative process the input parameter of the FEM simulation have to be refined until a good agreement between experiment and simulation is achieved.

From the resulting concentration and deformation profile it is possible to gain insight in the growth mechanism.

Outline of the thesis

The thesis is structured as follows. In *chapter 2* an overview of the techniques used for the experiments and the data evaluation is given. The chapter starts with a description of the x-ray techniques, in particular the contrast variation by anomalous scattering. After an introduction to the experimental set-up the data evaluation using the finite-element method is addressed. In *chapter 3* the technique of anomalous x-ray diffraction is applied for the investigation of free-standing and buried InGaAs quantum dots. *Chapter 4* deals with the investigation of shape, strain, and interdiffusion in InGaAs quantum rings using grazing incidence diffraction (GID) and grazing incidence small angle x-ray scattering (GISAXS). In *chapter 5* strain modulations in a quantum wire system produced by cleaved edge overgrowth are investigated. The last *chapter 6* gives an overview of the achieved results and the advancement of the x-ray methods. In a short *appendix* useful formulas for x-ray measurements in the GID geometry are summarised.

Chapter 2

Background

This chapter gives an overview of the techniques which have been used within this thesis for experiments and data evaluation. The first sub-chapter introduces the technique of contrast variation by anomalous diffraction. In the following section the experimental set-up and the applied scattering geometries are described. The last sub-chapter discusses finite-element calculations, which have been used for the interpretation of the x-ray diffraction data.

2.1 Contrast variation by anomalous diffraction

The basic principles of the kinematic scattering theory are assumed to be well known [Warren69, Cowley81, AlsNielsen01]. A general discussion of x-ray scattering at surfaces and interfaces can be found e.g. in the book by H. Dosch [Dosch92].

The aim of the following sections is to introduce the technique of contrast variation by anomalous scattering for the investigation of InAs/GaAs nanostructures.

At a weak *superstructure* (200) *reflection* this technique uses the change in the *anomalous dispersion corrections* close to the *K* absorption edge of As to enhance the scattering of InGaAs quantum dots on a GaAs substrate. Measurements at different energies below and above the absorption edge allow for a direct determination of the material composition of the pseudobinary alloy InAs/GaAs.

2.1.1 Superstructure reflections

The unit cell structure factor depends on the atomic positions \vec{r}_j . These are expressed by fractional coordinates x_j, y_j, z_j ($0 \leq x, y, z \leq 1$) along the basis vectors of the lattice $\vec{a}_1, \vec{a}_2, \vec{a}_3$ [Warren69].

$$\text{With } \vec{r}_j = x_j \vec{a}_1 + y_j \vec{a}_2 + z_j \vec{a}_3 \quad (\text{atomic positions}) \quad (2.1)$$

$$\vec{G} = h \vec{a}_1^* + k \vec{a}_2^* + l \vec{a}_3^* \quad (\text{lattice site in reciprocal space}) \quad (2.2)$$

$$\vec{Q} = \vec{G} \quad (\text{Bragg condition fulfilled}) \quad (2.3)$$

$$\text{and } \vec{a}_1^* = 2\pi \frac{\vec{a}_2 \times \vec{a}_3}{\vec{a}_1 \cdot (\vec{a}_2 \times \vec{a}_3)} \quad \text{and cyclic (reciprocal lattice basis vector)} \quad (2.4)$$

$$h, k, l \quad \text{integer} \quad (2.5)$$

$$\vec{a}_i \cdot \vec{a}_j^* = 2\pi \delta_{ij} \quad (2.6)$$

the unit cell structure factor of an h, k, l -reflection is given by

$$\begin{aligned} F_{hkl}^{\text{unit}} &= \sum_{r_j} f_j \exp(i \vec{Q} \vec{r}_j) = \\ &= \sum_{r_j} f_j \exp(i (h \vec{a}_1^* + k \vec{a}_2^* + l \vec{a}_3^*) (x_j \vec{a}_1 + y_j \vec{a}_2 + z_j \vec{a}_3)) = \\ &= \sum_j f_j \exp(i 2\pi (hx_j + ky_j + lz_j)) \end{aligned} \quad (2.7)$$

$f(\vec{Q})$ is the *atomic form factor*

$$f_0(\vec{Q}) = \int \rho(\vec{r}) e^{i \vec{Q} \vec{r}} d\vec{r} \quad (2.8)$$

The electron distribution is assumed as a charged cloud surrounding the nucleus with a number density $\rho(\vec{r})$. The integral over $\rho(\vec{r})$ is equal to the total number of electrons Z in the atom. $\vec{Q} = \vec{k}_{\text{in}} - \vec{k}_{\text{out}}$ describes the total wavevector transfer, $|\vec{k}| = 2\pi/\lambda$ being the wavevector, λ the wavelength of the x-rays.

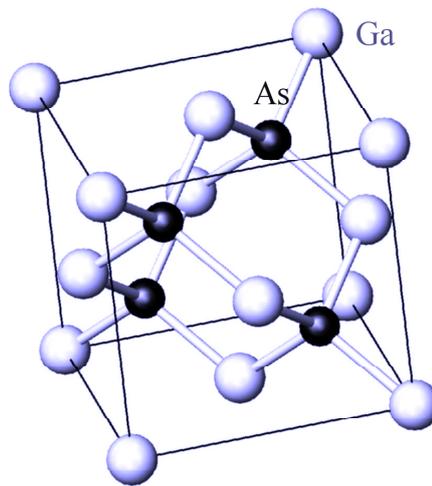


Figure 2.1: Zinc-blende structure of GaAs.

In case of the *zinc-blende structure* in which GaAs or InAs crystallises the face-centred cubic cell contains 4 *Ga* and 4 *As* atoms at the following positions:

$$Ga \begin{pmatrix} 0 & 0 & 0 \\ \frac{1}{2} & \frac{1}{2} & 0 \\ \frac{1}{2} & 0 & \frac{1}{2} \\ 0 & \frac{1}{2} & \frac{1}{2} \end{pmatrix} \quad As \begin{pmatrix} \frac{1}{4} & \frac{1}{4} & \frac{1}{4} \\ \frac{3}{4} & \frac{3}{4} & \frac{1}{4} \\ \frac{4}{3} & \frac{4}{1} & \frac{4}{3} \\ \frac{4}{1} & \frac{4}{3} & \frac{4}{4} \end{pmatrix}$$

Inserting these positions into Eq. 2.7 the squared structure factor $F_{hkl}^2 = F_{hkl}F_{hkl}^*$ takes 4 forms:

$$F_{hkl}^2 = 16(f_{Ga} - f_{As})^2 \quad \text{for} \quad h + k + l = (2n + 1) * 2 \quad (2.9)$$

$$F_{hkl}^2 = 16(f_{Ga} + f_{As})^2 \quad h + k + l = 4n \quad (2.10)$$

$$F_{hkl}^2 = 16(f_{Ga}^2 + f_{As}^2) \quad h, k, l \text{ all odd} \quad (2.11)$$

$$F_{hkl}^2 = 0 \quad h, k, l \text{ mixed} \quad (2.12)$$

Of particular interest are Eqs. 2.9 and 2.10 in the following discussion. The (200) superstructure reflection in the zinc-blende structure is a weak reflection, proportional to the *difference* of the atomic form factor of the involved atoms (Eq. 2.9). It is evident that this reflection can be highly suppressed if the form factors of the two contributing atoms are made almost equal. This is often achieved using the effect of anomalous dispersion corrections.

In contrast, the (400) reflection is according to Eq. 2.10 a strong reflection, proportional to the *sum* of the atomic form factor of the involved atoms.

It has to be noted that Eqs. 2.9 to 2.11 are valid in case of a stoichiometric binary alloy with long-range atomic ordering. Especially, the intensity of the superstructure reflections [e.g. (200)] scales with the degree of ordering (see [Warren69]).

2.1.2 “Anomalous” scattering

According to Eq. 2.8 the atomic form factor is given by the Fourier transform of the distribution of electrons in an atom. Its Q dependence originates from the non-negligible spatial distribution of the electrons in an atom. For forward scattering ($Q = 0$) all electrons scatter in-phase, so that $f_0(Q = 0)$ equals the total number of electrons Z in the atom. With increasing Q the electrons scatter more and more out of phase. Therefore, f_0 decreases for higher momentum transfer Q .

To describe the resonant behaviour close to absorption edges one has to take into account that electrons in an atom have discrete energy levels. The most tightly bound electrons are the ones in K shells. The K absorption edge is accessible for typical x-ray energies above 2keV for P ($Z = 15$) and all heavier elements. (The L edges can only be reached if $Z \geq 37$, the M edges if $Z \geq 66$.)

If the x-ray energy is much less than the binding energy of the K shell the response of these electrons to an external field is reduced by the fact that they are bound which is by convention

denoted as f' . If the x-ray energy is much greater than the binding energy, electrons can be treated as quasi free and f' is zero. For energies between these limits, f' displays *resonant behaviour* at energies corresponding to the atomic absorption edges. The bound electrons can be described by the model of a forced harmonic oscillator. Their *phase shift* ϕ with respect to the driving field is of importance close to an absorption edge, when electrons of a specific shell are in resonance, and scatter with a certain phase shifted by $\pi/2$. The phase shift is allowed for by including a term if'' , representing the dissipation in the system.

Therefore, the atomic form factor is described by a momentum dependent part (Eq. 2.8) and an energy dependent correction. The latter is usually referred to as the *anomalous dispersion corrections*, but since they are now mostly understood, it is generally agreed that there is in fact nothing anomalous about them [AlsNielsen01]. f' and f'' have their highest response when the x-ray energy is equal to one of the absorption edges of an atom.

$$f(\vec{Q}, \hbar\omega) = f_0(\vec{Q}) + f'(\hbar\omega) + if''(\hbar\omega) = |f|e^{i\phi} \quad (2.13)$$

with

$$\phi = \arctan \frac{f''}{f_0 + f'} \quad (2.14)$$

$$|f| = \sqrt{(f_0 + f')^2 + (f'')^2} \quad (2.15)$$

2.1.3 Contrast variation

It is a well-established technique [Materlik94] to tune the x-ray energy close to an absorption edge to enhance the sensitivity for a particular element. This effect is enhanced significantly for crystals with more than one element in their unit cells. In this case the anomalous dispersion correction can be used to annihilate or at least to strongly suppress superstructure reflections.

In the case of nanostructures this technique satisfies two aims. First, the *strong scattering contribution of the substrate* is suppressed. Therefore, the method is ideally suited for the investigation of strain, shape, and interdiffusion of free-standing nanostructures.

Secondly, the technique is chemically sensitive. Thus, it is possible to determine the *material composition* of a binary alloy from the ratio of the diffracted intensity measured at two x-ray energies close to an absorption edge. This results in a direct link between strain and composition.

Principle of the technique

In the following the technique is discussed for the InAs/GaAs material system. Both materials crystallise in the zinc-blende structure. Thus, weak superstructure reflections like the (200) Bragg peak exist (see Eq. 2.9). As the structure factor of this reflection is proportional to the *difference* of the atomic form factor of the involved atoms it is possible to suppress this reflection almost completely by tuning the x-ray energy close to the K absorption edge of As. This uses the energy dependence of the anomalous dispersion corrections to the atomic scattering factor (see Eq. 2.13).

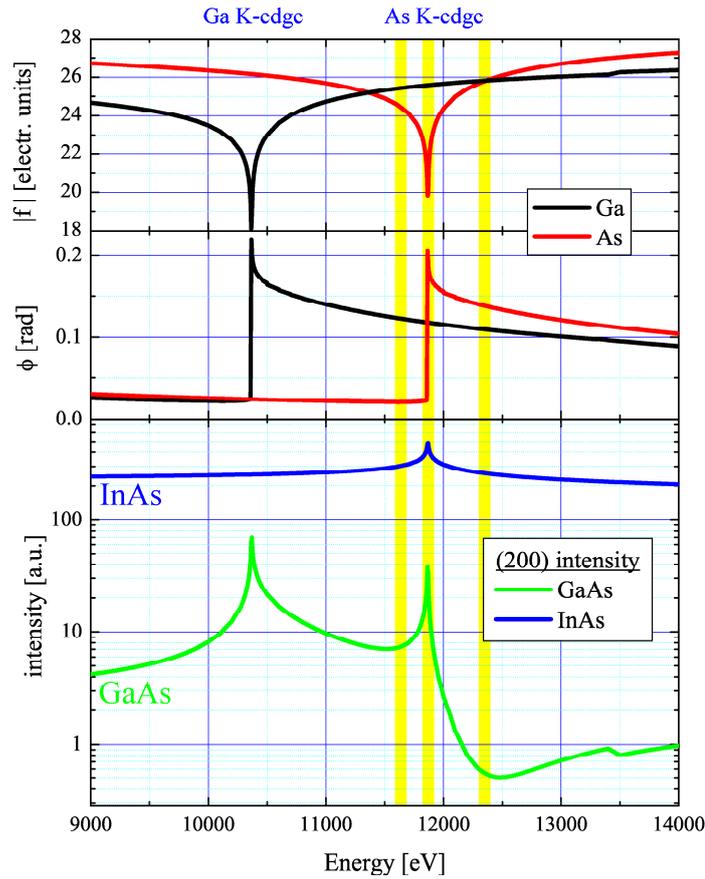


Figure 2.2: The absolute value of $|f_{Ga}|$ (black) and $|f_{As}|$ (red) is plotted together with the corresponding anomalous phases ϕ_{Ga} and ϕ_{As} . The graph at the bottom shows the calculated (200) intensity for GaAs (green) and InAs (blue) as a function of the x-ray energy. The yellow bars mark the three energies (11.630keV, 11.856keV, and 12.380keV) at which anomalous x-ray diffraction measurements have been performed.

Fig. 2.2 shows the absolute value of $|f_{Ga}|$ and $|f_{As}|$ together with the corresponding anomalous phases ϕ_{Ga} and ϕ_{As} . The atomic form factors and anomalous dispersion corrections of the elements are well known. Values of $f_0(Q)$, as well as for $f'(\hbar\omega)$, and $f''(\hbar\omega)$ are tabulated [Creagh92, Henke93, Baró94, Kissel95]. For a more precise evaluation of the momentum dependent behaviour of $f_0(Q)$ Baró et al. derived a parameterisation with a set of five parameters for every element [Baró94], which has been used for the calculations presented in this thesis. The anomalous dispersion correction was taken from [Henke93]. Data in this table have been determined semi-empirically, based upon experimental measurements of the atomic photoabsorption cross-section and theoretical calculations. The absorption measurements provide values for the imaginary part of the atomic scattering factor f'' . The real part f' is calculated from the absorption measurements using the Kramers-Kronig integral relations. Since the publication of the tables in 1993, the tabulated values have been revised based on new measurements.

From Eqs. 2.9 and 2.13 it becomes clear that once the absolute values of the scattering factors *and* their phases are equal, the scattered amplitude is completely annihilated. As is shown in Fig. 2.2 the absolute values of $|f_{Ga}|$ and $|f_{As}|$ are equal at two energies 11.373keV and 12.352keV above and below the K absorption edge of As. However, a complete annihilation is not possible as the anomalous phase has to be taken into account as well.

The calculated intensity $|F_{200}^2|$ (see Eq. 2.9) for GaAs and InAs is depicted in Fig. 2.2 at the bottom. Three energies which have been used for the experiments are marked by the yellow bars. In the whole range the diffracted intensity of InAs is practically unchanged. On the other hand, for GaAs a clear variation with energy is observed: above the absorption edge the contribution of GaAs is strongly suppressed as compared to energies below the K absorption edge of As.

In the following the contrast between the (200) intensities of InAs and GaAs is considered as a function of the x-ray energy E

$$\text{contrast}(E) = \frac{I_{\text{InAs}}(E)}{I_{\text{GaAs}}(E)} \quad (2.16)$$

At 11.856keV, slightly below the edge, a contrast factor of about 13 has been calculated. At 12.380keV the factor amounts to about 484. In this case the energy can be chosen in a broad minimum of the calculated F_{200}^2 intensity of GaAs. However, the contrast factor determined at 11.860keV depends crucially on a very accurate determination of the x-ray energy (accuracy of 1eV). To be less susceptible to alignment errors a third energy at 11.630keV was chosen. In this case the contrast between InAs and GaAs scattering is slightly larger (factor 4) than in the case of 11.856keV but still much smaller than at 12.380keV.

Energy in keV	11.630	11.856	12.380
(200) contrast	41	13	484
(400) contrast	1.8	2.6	1.7

Table 2.1: Theoretical contrast factors between InAs and GaAs scattering as a function of energy. The contrast was calculated according to Eq. 2.16.

The (400) reflection is a strong reflection (see Eq. 2.10). In this case the contrast between InAs and GaAs scattering as a function of the x-ray energy does practically not change at all. The contrast factors for the three energies 11.630keV, 11.856keV, and 12.380keV are 1.8, 2.6, and 1.7, respectively.

Thus, the (200) Bragg reflection at an energy of 12.380keV is best suited to suppress the scattering from the GaAs substrate.

Determination of a concentration profile

To use these effects for the material determination in nanostructures the intensity contrast measured at two energies (Energy1, Energy2) is important.

$$\text{contrast}(\text{Energy1}, \text{Energy2}) = \frac{I_{200}^{\text{Energy1}}}{I_{200}^{\text{Energy2}}} = \frac{|F_{200}^{\text{Energy1}}|^2}{|F_{200}^{\text{Energy2}}|^2} \quad (2.17)$$

F_{200} is the structure factor of the weak (200) reflection (see Eq. 2.9)

$$F_{200}^2 = 16(f_{\text{InGa}} - f_{\text{As}})^2 \quad (2.18)$$

The composition dependence of the scattering factor is given by

$$f_{\text{InGa}} = x \cdot f_{\text{In}} + (1 - x) \cdot f_{\text{Ga}} \quad (2.19)$$

x being the In concentration.

According to these equations only the ordered part of the “pseudobinary” alloy $\text{In}_x\text{Ga}_{1-x}\text{As}$ is taken into account. However, ordering in the sense that the group III positions in the zinc-blende structure are occupied by Ga or In atoms and the group V positions only by As atoms can be assumed from the MBE growth conditions (temperature and As overpressure) [Shahid88]. These are optimised to grow stoichiometric GaAs or InAs in the zinc-blende structure suppressing unwanted phases (orthorhombic or rhombohedral). In this case, the minimisation of the bonding energies between Ga and As or In and As, respectively, favours the ordering of the III-V atoms in the zinc-blende structure. The described x-ray techniques are not sensitive to the arrangement of the In and Ga atoms on the group III positions in the crystal.

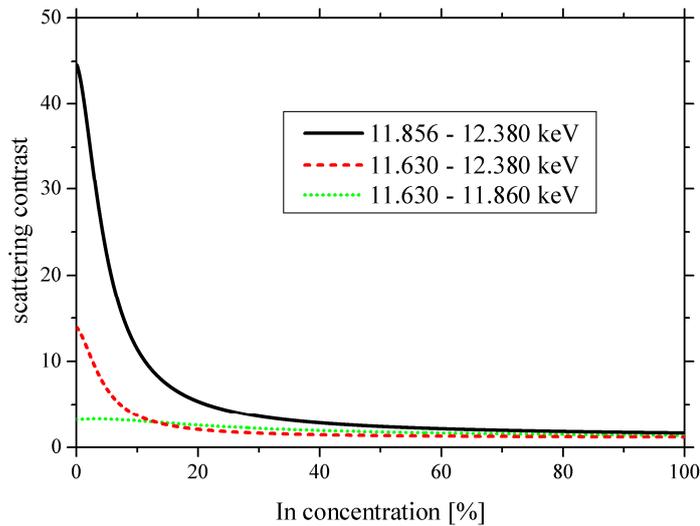


Figure 2.3: Calculation of the material composition from the (200) contrast between two x-ray energies according to Eqs. 2.17 to 2.19. The energy pairs are indicated in the legend.

With Eqs. 2.17 to 2.19 a relation between the measured scattering contrast at two energies and the corresponding In concentration is derived. Fig. 2.3 shows this relation for three pairs of energies. Due to the non-linearity of the equations the technique is especially sensitive for regions with low In concentration.

The largest contrast is achieved when comparing the intensity at 11.856keV and 12.380keV. In this case the energy close to the absorption edge has to be determined with an accuracy of 1eV to retain an error of less than 4% for the calculated InAs concentration. The comparison of measurements at 11.630keV and 12.380keV is less susceptible to alignment errors. However, only a weaker maximum scattering contrast is achieved (factor 3 less). Comparing the intensities measured at 11.630keV and 11.856keV the maximum contrast is with 3.2 too small for an accurate determination of the In concentration.

As an alternative the composition could be determined by comparing a strong [e.g. (400)] and weak [e.g. (200)] reflection. In this case no energy change is necessary. On the other hand, a direct comparison of different reflections is questionable, especially when both strain *and* form factor strongly contribute to the measured profile. The form factor distribution in Q -space does not depend on the investigated reflection. In contrast, the strain-induced distribution is spread out on a larger Q -range for higher indexed reflections.

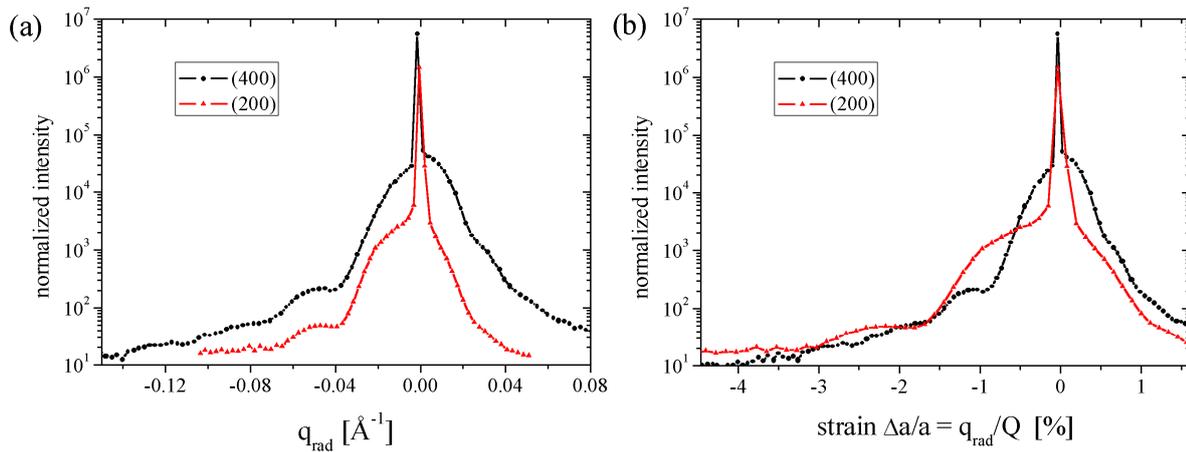


Figure 2.4: Comparison of radial measurements at the (200) and (400) reflection. Fig. (a) shows the measurements as a function of the radial momentum transfer q_{rad} , Fig. (b) as a function of strain $\Delta a/a$.

This is illustrated in Fig. 2.4. It shows a radial scan (see Sect. 2.2.3) at the (200) and (400) reflection at an energy of 11.856keV of a sample with quantum rings at its surface. In Fig. 2.4(a) the measurements are plotted as a function of the relative radial momentum transfer q_{rad} . The shape-induced oscillation for $q_{\text{rad}} < 0$ appear at the same position for both reflections. However, different lattice spacings $d = a/\sqrt{h^2 + k^2 + l^2}$ (with lattice parameter a) are investigated at the two Bragg reflections (hkl). Therefore, for a direct comparison the measurements have to be plotted as a function of $\Delta a/a = q_{\text{rad}}/Q$ which is shown in Fig. 2.4(b). The radial momentum transfer $Q_{200} = 2.2\text{\AA}^{-1}$ and $Q_{400} = 4.4\text{\AA}^{-1}$ differ by a factor of two. Then, the shape-induced oscillations for $q_{\text{rad}} < 0$ measured at the (400) reflection are

compressed by a factor two as compared to the (200) measurement, as well. This prohibits a direct comparison of the two reflections.

In addition, it has to be pointed out that the simple relation between scattering contrast and concentration (Eqs. 2.17 to 2.19) is only valid if the so-called *iso-strain scattering* model (see [Kegel01]) can be applied. In this model a free-standing dome-shaped island is vertically sliced in discs with a unique lattice parameter which changes monotonically with height. This lattice parameter is directly linked to a radial momentum transfer q_{rad} . Moreover, each individual iso-strain slice gives rise to a certain form factor of the scattered intensity distribution around the corresponding q_{rad} position. These distributions might overlap in reciprocal space with the scattering from other iso-strain areas. The model breaks down when the form factor of different strain states contributes to the same point in reciprocal space.

2.2 Experimental set-up

In this chapter an overview of the experimental set-up is given. It starts with a description of the beamline ID1 at the European Synchrotron Radiation Facility (ESRF) where all the x-ray measurements have been performed. A short description of the x-ray source, the diffractometer, the sample environment, and the detectors used is presented. A general introduction to synchrotron radiation can be found e.g. in [AlsNielsen01].

In the following three sections the different applied scattering geometries are described: coplanar x-ray diffraction (XRD), grazing incidence diffraction (GID), and grazing incidence small angle scattering (GISAXS). The use of an analyser crystal for GID at energies close to an absorption edge is discussed in the according sub-chapter.

2.2.1 Beamline ID1



Figure 2.5: The experimental hall of the ESRF seen from the fifth floor of the administration building. The neutron reactor of the Institute Laue-Langevin (ILL) can be seen on the left.

All measurements have been performed at the European Synchrotron Radiation Facility (ESRF) in Grenoble, France. The ESRF is a third generation synchrotron, working at an energy of

6GeV. The storage ring for the electron beam has a circumference of 844m, with 40 beamlines (see Fig. 2.5).

At the beamline ID1 [Lequien94] two insertion devices (a wiggler and an undulator) are available to produce synchrotron radiation of high brilliance. An energy range of 2.1keV to 40keV can be covered. This makes the beamline very suitable for *anomalous scattering*.

Fig. 2.6 shows the tunnel of the storage ring close to ID1. The shielding concrete blocks forming the roof of the tunnel have temporarily been removed. On the left side the x-ray beam is guided in the direction of the beamline ID1 (in the background). The insertion devices of this experimental station are situated up-stream and cannot be seen on the photo. The blue painted bending magnet produces x-ray radiation for the beamline BM1 (Swiss-Norwegian beamline), the insertion device further downstream (purple) produces the radiation for the beamline ID2.

Using an undulator the energy is set by an appropriate gap of the insertion device. Depending on the required energy, the first, third or fifth harmonic can be chosen. At ID1 a double crystal monochromator allows for a fine tuning of the x-ray energy, with the beam always fixed at the sample position. The second monochromator crystal also serves as a focussing device (sagittal focussing) in the horizontal direction. Two mirrors, installed before and after the monochromator, facilitate the suppression of higher harmonics. This is achieved by choosing an appropriate incident angle right below the critical angle of total external reflection of the desired harmonic, but well above the critical angle of the next higher harmonic. The second mirror is used for vertical focussing.

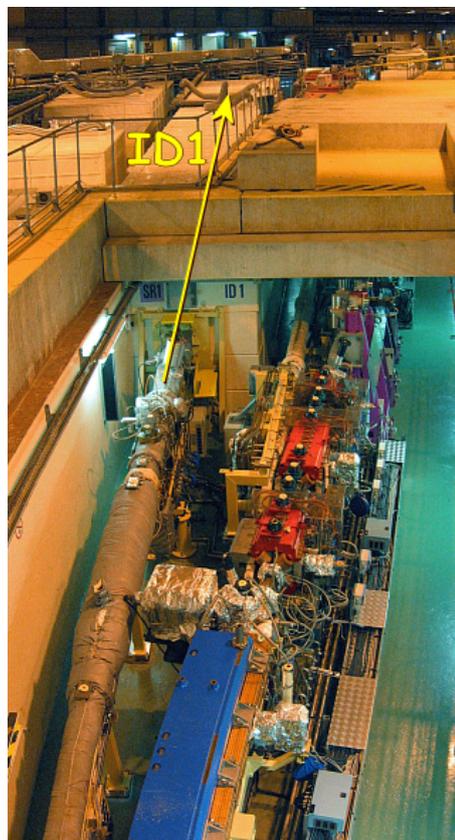


Figure 2.6: View of the storage ring. The concrete shielding has been temporarily removed. See text for more details.

The beamline ID1 was designed to be used in a large energy range. At lower energies absorption and scattering by air plays a more and more important role. To cope with this problem the beamline can be operated completely in vacuum, windowless from the x-ray source to the detector (using differential pumping). For this reason a big vessel was constructed (13m³ volume), housing a 4+2 axes diffractometer (see Fig. 2.7). In a 4S+2D circle diffractometer as described by H. You [You99] four degrees of freedom are used for the sample positioning (*eta*, *chi*, *phi*, and *mu*), two independent circles are for the orientation of the detector (*del* and *nu*). When necessary *oma* and *tha* are used to set the Bragg angle of an optional analyser crystal. A particular difference of a 4+2 axes diffractometer to a 6 circle diffractometer [Vlieg97] is the nonexistence of a common rotation of the sample *and* the detector circles.

Fig. 2.8 shows a picture of the diffractometer with a typical set-up in grazing incidence diffraction geometry. The x-ray beam arrives from the right. A scattering foil in front of the sample position serves as an intensity monitor for the primary beam. The sample is fixed vertically under the orange tent in the centre of rotation of the diffractometer. The diffracted intensity

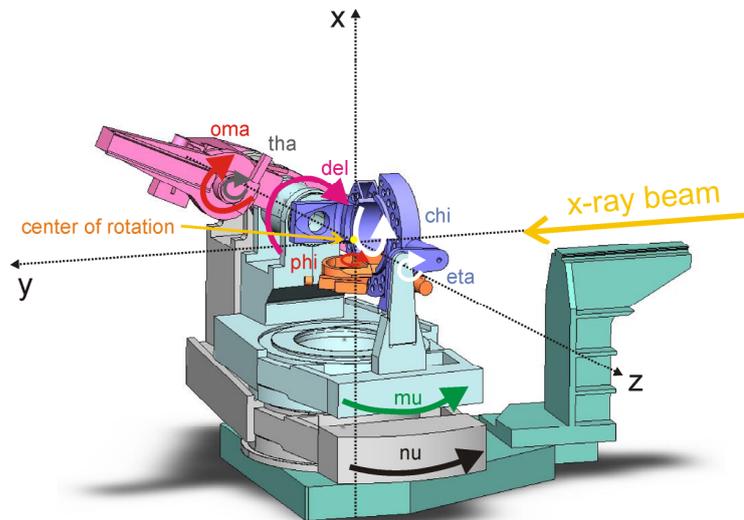


Figure 2.7: The 4S+2D circle diffractometer at the beamline ID1. The axes of the four sample circles (*eta*, *chi*, *phi*, and *mu*) and the two independent detector circles (*del* and *nu*) are indicated. *oma* and *tha* are used to set the Bragg angle of an analyser crystal.

is detected with a linear position sensitive detector mounted at the end of the detector arm (*del*). To gain energy resolution a graphite analyser is mounted at the *tha* rotation. Optionally a single crystal could be used for high-resolution x-ray scattering with an angular resolution up to a few thousands of a degree.

The experiments presented in this thesis were all performed in an energy range between 8keV and 12keV. In this range it is not necessary to evacuate the whole diffractometer vessel. To reduce air scattering evacuated flight tubes are sufficient. The sample itself is protected by a Kapton tent flushed with He. This prevents the formation of ozone which is known to chemically attack the sample surface. In air, ozone is generated due to ionisation by the x-rays.

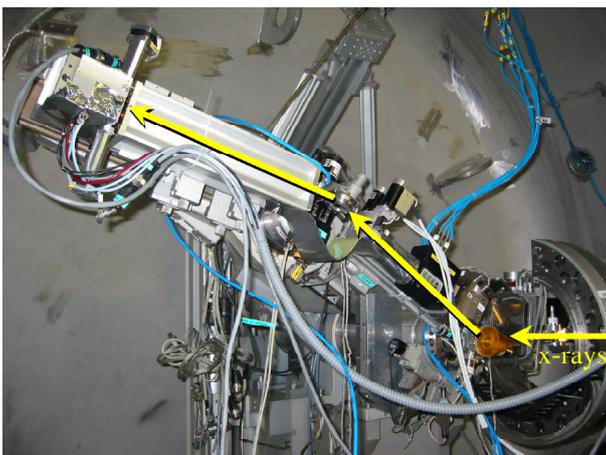


Figure 2.8: GID set-up using a graphite analyser. Flight tubes are used to reduce air scattering.

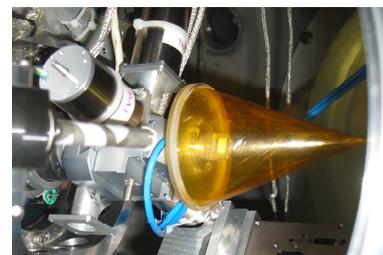


Figure 2.9: Sample environment: a Kapton tent flushed with He is used to protect the sample.

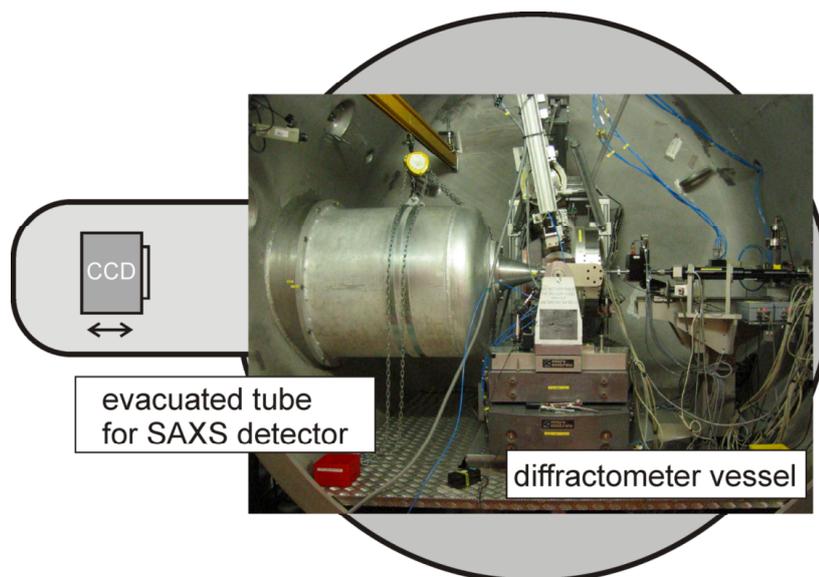


Figure 2.10: Set-up for small angle scattering. The detector (CCD) can be moved between 0.6m and 4.6m from the sample. The whole tube containing the CCD is evacuated up to the sample position. For this the SAXS vacuum cone is mounted, as shown in the picture.

In addition, the beamline ID1 is well-suited for small angle x-ray scattering (SAXS). Fig. 2.10 shows a suitable set-up. The x-ray beam enters from the right side and hits the sample mounted horizontally in the centre of rotation of the diffractometer. A large evacuated cone is mounted reaching as close as possible to the sample. This cone expands into a 4.6 metre long evacuated tube containing a two-dimensional detector (CCD) to record the small angle scattering with an angular resolution of a few thousands of a degree.

Detectors

Two different detectors have been used. A linear position sensitive detector (PSD) and a two-dimensional detector (CCD).

The PSD produced by Braun is very well suited to record α_f -resolved maps in grazing incidence diffraction and can be easily mounted on the detector arm. It is based on gas ionisation. Photons enter the counting tube via a thin beryllium window ($400\mu\text{m}$) and ionize the counting gas $[\text{Ar}_{0.9}(\text{CH}_4)_{0.1}]$. The electrons produced are accelerated towards the *counting wire* (5cm long) in the centre of the counting tube. A *spatial resolution* with an accuracy of $100\mu\text{m}$ is achieved by a cathode structure of pairs of triangular teeth at the back of the tube. The x-ray induced ions cause a charge on the cathode surface. The triangular teeth which are isolated with respect to each other induce an differential signal which determines the spatial position.

The two-dimensional CCD camera by Princeton was used for GISAXS measurements. The detector is a 1242×1152 pixel fibre-optic taper CCD camera with a resolution of $110\mu\text{m}$. X-rays pass through a thin beryllium window and are absorbed by a circular phosphor screen, which emits visible light reaching the CCD chip by a system of fibre-optics. The CCD detects

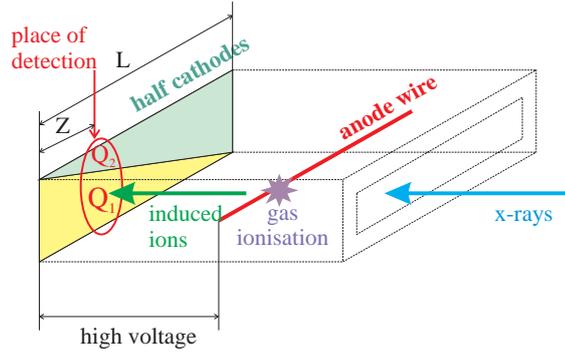


Figure 2.11: Functional principle of the PSD. The spatial position of the detected radiation is determined by the ratio of the induced charges on the triangular pairs of cathodes: $Z = L(Q_1/(Q_1 + Q_2))$

one or more visible photons per x-ray photon that is absorbed. The camera in use at ID1 was adapted for use in vacuum down to $1.3 \cdot 10^{-3}$ mbar.

2.2.2 X-Ray Diffraction (XRD)

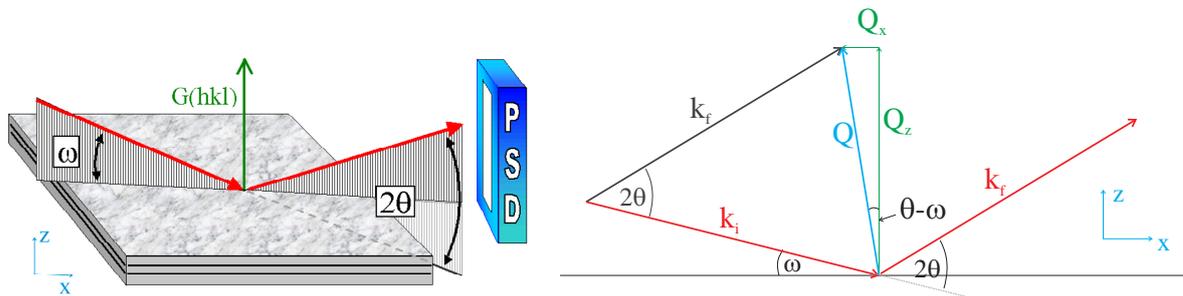


Figure 2.12: Sketch of the XRD geometry. The wavevectors of the incident and scattered waves k_i , k_f , respectively, are shown together with the commonly used notation of scattering angles.

Fig. 2.12 shows the set-up for co-planar high angle x-ray diffraction (XRD). The common notation of the diffraction angles is given in the figure. The incident angle is denoted by ω . The diffracted intensity is measured under an angle of 2θ relative to the incident beam. Due to the co-planar geometry only two coordinates of the momentum transfer \vec{Q} have to be considered:

$$Q_x = 2k \sin \theta \sin(\omega - \theta) \quad (2.20)$$

$$Q_z = 2k \sin \theta \cos(\omega - \theta) \quad (2.21)$$

$|\vec{k}_i| = |\vec{k}_f| = k = 2\pi/\lambda$ is the wavevector of the incident and elastically scattered waves, λ denotes the wavelength of the x-ray beam.

2.2.3 Grazing Incidence Diffraction (GID)

The grazing incidence diffraction geometry combines a diffraction process at crystal planes perpendicular to the sample surface with the depth sensitivity of x-rays.

The depth sensitivity originates from the fact that for x-rays the refractive index $n = 1 - \delta + i\beta$ of condensed matter is slightly smaller than 1. Therefore, according to Snell's law, total external reflection at surfaces is observed for incident angles α_i smaller than a critical angle α_c

$$\alpha_c = 90^\circ - \arcsin n \approx \sqrt{2\delta} \quad (2.22)$$

δ and β are the dispersive and absorptive part of the refractive index, respectively.

The scattering depth Λ defines the depth, where the observed scattering originates from [Dosch92]:

$$\Lambda = \frac{\lambda}{2\pi(l_i + l_f)} \quad (2.23)$$

with

$$l_{i,f} = \frac{\sqrt{2}}{2} \sqrt{(2\delta - \sin^2 \alpha_{i,f}) + \sqrt{(\sin^2 \alpha_{i,f} - 2\delta)^2 + 4\beta^2}} \quad (2.24)$$

The scattering depth (Eq. 2.23) depends on the incident and exit angle (α_i and α_f), while the penetration depth $L = \lambda/2\pi l_i$ only takes into account the incident angle α_i .

When the condition of total external reflection holds, the penetration depth of the incident x-ray beam is only a few tens of angstroms, and the reflectivity is near unity. As the angle is increased past the critical angle, the reflectivity decrease rapidly, while the penetration depth increases.

Therefore, the GID technique is near-surface sensitive and allows to enhance the ratio of scattering from near-surface nanostructures to the bulk crystal.

α_f resolved measurements under grazing incidence and exit show a cumulative depth resolution, i.e. the measured intensity for a certain α_f contains contributions from the surface to the corresponding scattering depth Λ . Furthermore one has to keep in mind that the scattering depth of x-rays is not a sharp border. Rather it is defined as the depth at which the exponential intensity decay within the sample reaches $1/e$.

Fig. 2.13 shows the set-up for the GID technique. The incident wavevector impinges under a grazing incidence angle α_i on the surface and is reflected in a α_f distribution of wavevectors \vec{k}_f . The exit angle-resolved signal can be efficiently recorded with a linear position sensitive detector (PSD). This signal contains the α_f resolved information about the sample.

The scattering process depends on four angles: α_i , α_f , ω , and 2θ . As the momentum transfer \vec{Q} only has three components one parameter can be chosen freely. This is usually the incident angle α_i which defines the maximum penetration depth.

For the measurements a relative (radial/angular) coordinate system ($Q_{\text{rad}}, Q_{\text{ang}}, Q'_z$) is commonly used. Q_{rad} defines the radial distance from the origin of reciprocal space, Q_{ang} depicts the deviation of the reciprocal space position from the radial path $\omega = \theta$.

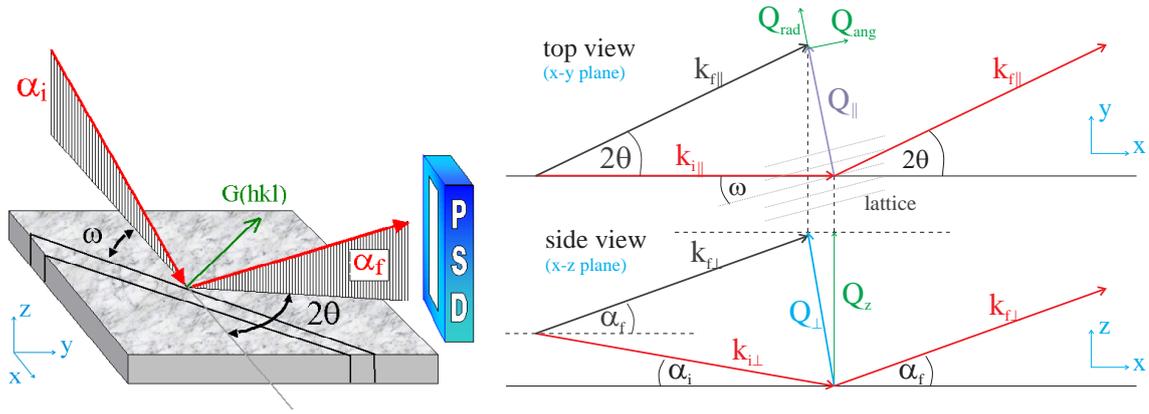


Figure 2.13: Sketch of the GID geometry. A position sensitive detector (PSD) can be used for an efficient recording of the α_f -resolved scattered signal. On the right the wavevectors of the incident and scattered waves k_i , k_f , respectively, are shown in a projection into the x - y and x - z plane. The incidence and exit angles α_i , α_f are very small compared to the scattering angles ω and 2θ .

The reciprocal space coordinates in small angle approximation can be derived from the diffractometer angles as

$$Q_{\text{ang}} = 2k \sin \theta \sin(\omega - \theta) \quad (2.25)$$

$$Q_{\text{rad}} = 2k \sin \theta \cos(\omega - \theta) \quad (2.26)$$

$$Q'_z = k \left[\sqrt{\sin^2 \alpha_i - 2\delta} + \sqrt{\sin^2 \alpha_f - 2\delta} \right] \quad (2.27)$$

$$Q_z = k (\alpha_i + \alpha_f) \quad (2.28)$$

with $|\vec{k}_i| = |\vec{k}_f| = k = 2\pi/\lambda$. In this case Q'_z defines the momentum transfer in the material, δ being the dispersive part of the index of refraction. For $\alpha_i < \alpha_c$ the momentum transfer $Q'_z = 0$. The external momentum transfer is defined by Q_z .

GID using an analyser crystal

When performing GID experiments using anomalous scattering the background increases significantly due to inelastic scattering processes. These contributions to the background arise from fluorescence and resonant Raman scattering which are enhanced when the incident x-ray energy is close to an absorption edge. The position sensitive detector used has only a energy resolution of about $\Delta E/E \approx 10\%$ in the energy range used. Therefore, a graphite mosaic analyser crystal was used to separate the inelastic scattering (see Fig. 2.14). The possibly smaller diffraction efficiency of mosaic crystals is more than compensated for by the increased signal to background ratio.

Mosaic crystals are formed by a large number of small perfect crystallites of microscopic size [Rio98, Ice90]. The crystallites are assumed to be oriented almost parallel to the crystal surface following a Gaussian distribution with a FWHM τ , the so-called *mosaic spread*. The mosaic spread of the graphite analyser used was determined experimentally to be $\tau = 0.42^\circ$.

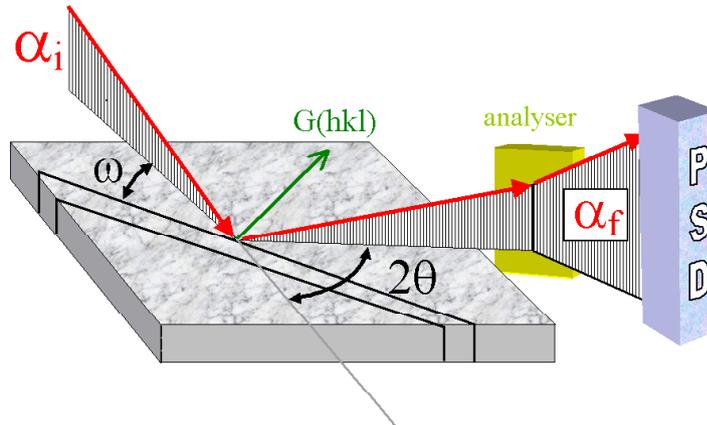


Figure 2.14: To separate inelastic scattering from the elastically diffracted intensity a graphite analyser was added to the standard GID set-up.

In the diffraction plane the crystallites inside a flat mosaic crystal produce a monochromatic focussing effect of the x-ray beam in a 1 : 1 magnification configuration. This is sketched in Fig. 2.15(b). The position of the focal spot S' in the diffraction plane depends on the Bragg angle (and thus on the photon energy) producing spots in different spatial positions for different photon energies, which implies that the focusing circle (dashed line in Fig. 2.15) changes with energy. This focussing effect depending on the photon energy is called *parafocussing*.

In the plane perpendicular to the diffraction plane a defocussing effect is observed [see Fig. 2.15(a)]: the beam divergence ω is increased from ω to $\omega + 2\tau \sin \theta_{\text{Bragg}}$, θ_{Bragg} being the Bragg angle [Rio98]. As all measured intensities recorded close to the K absorption edge of As were integrated along the linear detector this doesn't play a role for the evaluation of the data.

The energy resolution of the graphite analyser was determined to be

$$\frac{\Delta E}{E} = \Delta\theta \cot(\theta_{\text{Bragg}}) \approx 1\% \quad (2.29)$$

with a FWHM $\Delta\theta = 0.11^\circ$ measured at an energy of $E = 11.866\text{keV}$ and a Bragg angle of $\theta_{\text{Bragg}} = 9.0^\circ$. Therefore, it is possible to separate the As fluorescence K_β emission at 11.726keV .

Fig. 2.16 shows a radial scan of a sample with quantum ring structures on its surface. The measurement was taken at the (200) Bragg reflection at an energy of 12.380keV with and without using a graphite analyser. It becomes obvious that the inelastic background can be suppressed. With the analyser crystal the dynamic range of the measurement is enlarged by more than one order of magnitude.

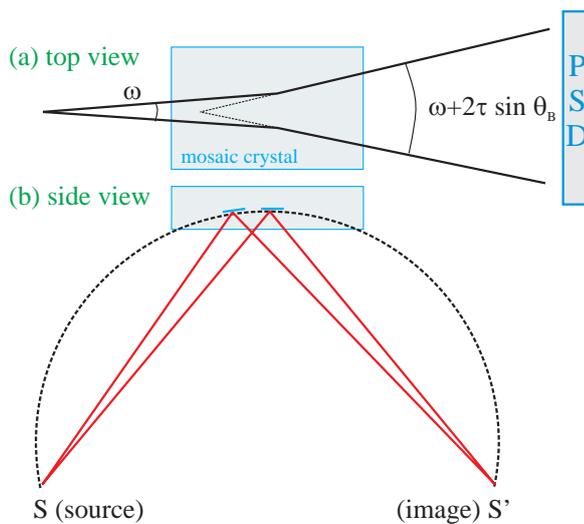


Figure 2.15: Parafocusing effect of a mosaic crystal in the diffraction plane (b). Only photons with a certain energy are focused in S' . The distances crystal- S' and S -crystal are equal. Fig. (a) shows the defocusing effect in the plane perpendicular to the diffraction plane.

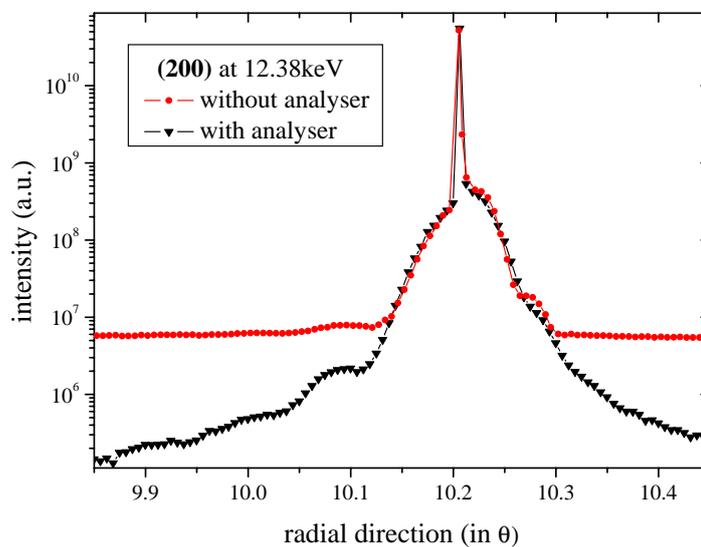


Figure 2.16: Inelastic scattering background. Using an analyser crystal the dynamic range of the measurement can be enlarged by more than one order of magnitude.

2.2.4 Grazing Incidence Small Angle Scattering (GISAXS)

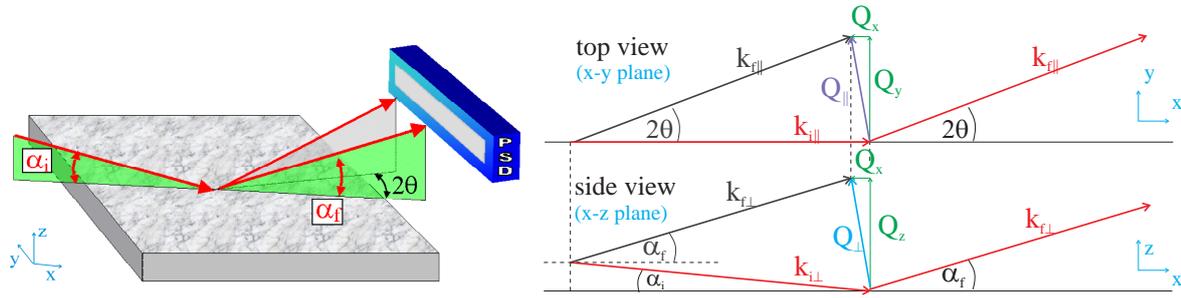


Figure 2.17: Sketch of the GISAXS geometry. On the right the wavevectors of the incident and scattered waves k_i , k_f , respectively, are shown in a projection into the x - y and x - z plane.

Fig. 2.17 shows the set-up for the GISAXS geometry. The scattered intensity is recorded in an efficient way either using a linear position sensitive detector (PSD) or a two-dimensional detector (CCD).

The technique is insensitive to strain due to the small momentum transfer. Thus, only the variation of the average electron density is probed. The momentum transfer is calculated from the diffractometer angles as

$$Q_x = k (\cos \alpha_i - \cos \alpha_f \cos 2\theta) \quad (2.30)$$

$$Q_y = k \cos \alpha_f \sin 2\theta \quad (2.31)$$

$$Q_z = k (\sin \alpha_i + \sin \alpha_f) \quad (2.32)$$

2.3 Finite-Element Method (FEM)

X-ray diffraction is a powerful tool for the investigation of shape, strain and interdiffusion in nanostructures [Schmidbauer03]. For the interpretation of the measured data a simulation technique of the elastic strains and displacement fields in these nanostructures is needed. Using Fourier transforms the simulated data are converted into reciprocal space maps, which are compared to the measured data.

The most common methods of strain calculation is based on the elasticity continuum approximation. It consists in the numerical solution of the equilibrium equations using a *finite-element approach* (FEM). Several software packages are available yielding the space distribution of the components of the strain tensor and the displacement vector for any structure.

Section 2.3.1 contains a short summary of the theory of elasticity. A more detailed description can be found in [Love44, Sokolnikoff56, Zener55]. Section 2.3.2 presents the basic ideas of the FEM approach. More details can be found in the literature: [Braess97, Goering93, Zienkiewicz87]. A last section (2.3.3) demonstrates the most important steps of the FEM simulation of a buried quantum dot. This simulation uses the PATRAN/NASTRAN software package which is briefly introduced as well.

2.3.1 Theory of elasticity

In heteroepitaxy, the lattice mismatch of a coherently grown island (e.g. in the Stranski-Krastanov mode - see chapter 1) induces elastic strain in the island and the host crystal.

The corresponding **displacement field**

$$\vec{u}(\vec{x}) = \vec{x}' - \vec{x} \quad (2.33)$$

describes the translation of a point $P(\vec{x})$ from a position \vec{x} to \vec{x}' . Thereby the displacement field is indexed by the position x in the undeformed matrix.

Changes in finite *volume elements* are characterised by the transformation of vectors. Two points $P_0(\vec{x}_0)$ and $P(\vec{x})$ are joined by a vector

$$\Delta\vec{x} = \vec{x} - \vec{x}_0 \quad (2.34)$$

As the volume containing P_0 and P undergoes a deformation, the points move to $P'_0(\vec{x}'_0)$ and $P'(\vec{x}')$ in the deformed matrix. They are now joined by a vector

$$\Delta\vec{x}' = \vec{x}' - \vec{x}'_0 = [\vec{x} + \vec{u}(\vec{x})] - [\vec{x}_0 + \vec{u}(\vec{x}_0)] = \Delta\vec{x} + \Delta\vec{x}(\vec{\nabla} \otimes \vec{u}) \quad (2.35)$$

using the Taylor expansion of a vector field

$$\vec{u}(\vec{x} + \vec{\varepsilon}) \approx \vec{u}(\vec{x}) + (\vec{\varepsilon} \cdot \vec{\nabla})\vec{u} = \vec{u}(\vec{x}) + \vec{\varepsilon}(\vec{\nabla} \otimes \vec{u}) \quad (2.36)$$

\otimes denotes the dyadic product

$$\vec{x} \otimes \vec{y} := \begin{pmatrix} x_1y_1 & x_1y_2 & x_1y_3 \\ x_2y_1 & x_2y_2 & x_2y_3 \\ x_3y_1 & x_3y_2 & x_3y_3 \end{pmatrix} \quad (2.37)$$

The absolute square of the vector 2.35 is

$$|\Delta\vec{x}'|^2 = |\Delta\vec{x}|^2 + 2\varepsilon_{ij}\Delta x_i\Delta x_j \quad (2.38)$$

using *Einstein's summation convention*. ε_{ij} is defined as the **strain tensor**. In linear elasticity theory, the components of the strain tensor are related linearly to the deviations of the displacement components:

$$\varepsilon_{ij} := \left(\frac{\delta u_i}{\delta x_j} + \frac{\delta u_j}{\delta x_i} \right) \quad (2.39)$$

The strain tensor is symmetric by definition. Its diagonal elements ε_{ii} are called *principal strains* or *normal strains*. They cause elongations ($\varepsilon_{ii} \geq 0$) or contractions ($\varepsilon_{ii} \leq 0$) along the corresponding axes of the coordinate system. The non-diagonal components are called shear strains. While the principal strains preserve the angle of a control element, but change the length of the sides, shear strains preserve the length, and change the angles.

If an *external force* acts on an element or if one part of the element applies force on another part, the element is in the state of stress. Stress is defined in units of force per unit area and is characterised by the **stress tensor** σ_{ij} .

σ_{ij} denotes the force per unit area on the i^{th} face in the j^{th} direction. The equations of static equilibrium are obtained from the divergence of the stress tensor:

$$\begin{aligned}\frac{\delta}{\delta x}\sigma_{xx} + \frac{\delta}{\delta y}\sigma_{xy} + \frac{\delta}{\delta z}\sigma_{xz} &= -f_x \\ \frac{\delta}{\delta x}\sigma_{yx} + \frac{\delta}{\delta y}\sigma_{yy} + \frac{\delta}{\delta z}\sigma_{yz} &= -f_y \\ \frac{\delta}{\delta x}\sigma_{zx} + \frac{\delta}{\delta y}\sigma_{zy} + \frac{\delta}{\delta z}\sigma_{zz} &= -f_z\end{aligned}\quad (2.40)$$

f gives the acting force. The stress tensor σ_{ij} is symmetric (otherwise the element would start rotating).

In linear elasticity theory the components of the stress tensor are related linearly to the components of the strain tensor. This is expressed by the **generalised Hooke's law**:

$$\boxed{\sigma_{ij} = c_{ijkl}\varepsilon_{kl}} \quad (2.41)$$

c_{ijkl} is the **tensor of the elastic constants**. It is a fourth-rank tensor containing $3^4 = 81$ elements. As σ_{ij} and ε_{kl} are symmetric tensors c_{ijkl} has only 36 independent components. Therefore, it can be described with *compressed indices (Voigt's notation)* in a 6×6 matrix:

$$ij \rightarrow \begin{cases} i & \text{for } i = j \\ 9 - i - j & \text{for } i \neq j \end{cases} \quad (2.42)$$

or in better readable form

$$\begin{aligned}xx &\rightarrow 1 \\ yy &\rightarrow 2 \\ zz &\rightarrow 3 \\ yz &\rightarrow 4 \\ xz &\rightarrow 5 \\ xy &\rightarrow 6\end{aligned}\quad (2.43)$$

The only drawback of this shorthand notation is that c_{ij} , unlike c_{ijkl} , is *not* a tensor any more. A coordinate transformation for the elastic constants e.g. cannot be executed in compressed indices.

A further reduction of the number of independent elastic constants is achieved taking into account the *symmetry of the crystal lattice*.

For cubic crystals there are only three independent elastic constants:

$$\begin{aligned}c_{11} &= c_{22} = c_{33} \\ c_{12} &= c_{23} = c_{31} \\ c_{44} &= c_{55} = c_{66}\end{aligned}\quad (2.44)$$

Therefore the tensor has the form

$$\mathbf{c} = \begin{pmatrix} c_{11} & c_{12} & c_{12} & 0 & 0 & 0 \\ c_{12} & c_{11} & c_{12} & 0 & 0 & 0 \\ c_{12} & c_{12} & c_{11} & 0 & 0 & 0 \\ 0 & 0 & 0 & c_{44} & 0 & 0 \\ 0 & 0 & 0 & 0 & c_{44} & 0 \\ 0 & 0 & 0 & 0 & 0 & c_{44} \end{pmatrix} \quad (2.45)$$

In the case of an elastically isotropic cubic crystals two constants are sufficient:

$$\mu = \frac{1}{2}(c_{11} - c_{12}) = c_{44} \quad (\text{shear modulus}) \quad (2.46)$$

$$\nu = \frac{c_{12}}{c_{11} + c_{12}} \quad (\text{Poisson's ratio}) \quad (2.47)$$

Therefore, an elastically isotropic cubic material which is compressively strained in one direction will perpendicularly react with an expansion.

2.3.2 Finite-element technique

The basic idea of the finite-element method is to divide the investigated volume into smaller elements of finite dimensions, so-called "*finite elements*". The original structure is then composed by an assembly of these elements which are connected to each other at joints, called "nodes". The equations of equilibrium for the entire structure are obtained by combining the equilibrium equation of each element such that the continuity is ensured at each node. By analysing only the individual elements, a summation over the entire volume consisting in a *finite number* of elements of *finite dimensions* is carried out - instead of carrying out an integration over the volume consisting of an infinite number of elements of infinitesimally small dimensions. Several FEM software packages are available to obtain a solution of these equations.

Boundary conditions

The division of a given structure into finite elements is one of the first steps in the analysis of a structural model. The necessary boundary conditions are then imposed and the equations of equilibrium are solved to obtain the required variables such as strain and displacements. Boundary conditions are defined e.g. by the symmetry and the shape of the element. External forces could also cause constraints. For the investigation of nanostructures, lattice mismatch is the *only* source for elastic deformations. No other loads or volume forces are applied. Consequently any surface is either free of external forces or fixed by a displacement constraint. Within the FEM simulation the mismatch-induced deformations can be described in two entirely equivalent ways:

1. *Mismatched materials.* The investigated task can be simplified by a volume A (lattice parameter a) containing a volume B (lattice constant b). Due to the lattice mismatch

$$\kappa = \frac{b - a}{a} \quad (2.48)$$

the matrix B will deform. This causes an uniform strain in this volume of $\varepsilon_{ij}^M = -\kappa\delta_{ij}$ with respect to its strain-free state. Taking into account the macroscopic strain $\varepsilon_{ij}(\vec{x})$ with respect to the reference state (stress-free state of volume A), the actual strain in volume B is described by

$$\varepsilon_{ij}^B(\vec{x}) = \varepsilon_{ij}(\vec{x}) + \varepsilon_{ij}^M = \varepsilon_{ij}(\vec{x}) - \kappa\delta_{ij} \quad (2.49)$$

The stress tensor is according to Eq. 2.41

$$\sigma_{ij}^B(\vec{x}) = c_{ijkl}^B \varepsilon_{kl}^B(\vec{x}) = c_{ijkl}^B [\varepsilon_{kl}(\vec{x}) - \kappa\delta_{kl}] \quad (2.50)$$

where c_{ijkl} are the elastic constants of volume B.

2. *Thermo-Elasticity.* The thermal strain ε_{ij}^T in an elastic medium due to isotropic thermal expansion is

$$\varepsilon_{ij}^T = \alpha\Delta T\delta_{ij} \quad (2.51)$$

α describes the thermal expansion coefficient, ΔT is the temperature deviation from the reference temperature T_0 . Together with the elastic strain $\varepsilon_{ij}^E(\vec{x})$ the total strain is

$$\varepsilon_{ij}(\vec{x}) = \varepsilon_{ij}^T + \varepsilon_{ij}^E(\vec{x}) \quad (2.52)$$

The medium is stress free if $\varepsilon_{ij} = \varepsilon_{ij}^T$. Therefore, only deviations by the elastic strain yield stress

$$\sigma_{ij}(\vec{x}) = c_{ijkl}^E \varepsilon_{kl}^E(\vec{x}) = c_{ijkl}^E [\varepsilon_{kl}(\vec{x}) - \alpha\Delta T\delta_{kl}] \quad (2.53)$$

Comparing Eqs. 2.50 and 2.53, one can see that mismatch can be described as a thermo-elastic problem. In practise this second possibility is more convenient for FEM modelling. The strain fields are calculated by defining the pseudomorphic structures at a reference temperature $T_0 = 300\text{K}$ and equilibrating the structures after increasing the temperature to $T = 301\text{K}$. The thermal expansion coefficient has to be

$$\alpha = \frac{\kappa}{\Delta T} \quad (2.54)$$

with $\Delta T = 1\text{K}$.

Symmetry

The symmetry of the elastic model plays an important role for the calculation time. If it possesses mirror symmetry, it is sufficient to solve the equations of elasticity for just one half of the space. If it shows n -fold rotational symmetry, it is even sufficient to calculate only one sector $2\pi/n$. In both cases appropriate boundary conditions for the interfaces have to be assumed.

Corresponding to the cylindrical symmetry of the nanostructures a sector of 45° was simulated. Taking into account these considerations the following boundary conditions have been used:

- Points at the bottom of the defined grid are fixed.
- Points lying in the front or the back plane of the defined solid can move within this plane.
- Points in the centre (at radius = 0) and at the maximum radius can only move along the z direction, perpendicular to the sample surface.
- All material parameters were defined for a reference temperature of $T_0 = 300\text{K}$. The “load” consists of a hypothetical temperature increase of 1K.

FEM calculation

Taking into account these constraints the finite-element program calculates the displacements at the node points and determines the strains in the element centres from the displacement values.

The substrate size has been chosen large enough so that a further increase does not influence the calculated displacement field. On the other hand, the range in reciprocal space which can be simulated is limited by the size of the simulated area in real space. The maximum resolution of the simulation along q_{ang} , q_{rad} , and q_z is determined by $\Delta q = 2\pi/L$, with L being the size of the simulated area. The step width of the FEM calculation Δl limits the maximum range of the simulated reciprocal space map: $q_{\text{max}} = 2\pi/\Delta l$.

To simulate reciprocal space maps, which have been recorded in grazing incidence diffraction, the in-plane displacement field u_x has to be determined by FEM. Although a 3D model has been calculated taking the full elastic anisotropy into account, for the transformation into reciprocal space a 2D displacement field in a plane through the centre of the dot has been used. It can be shown that the anisotropy of the InAs/GaAs system is negligible by extracting the displacement fields in different vertical planes from the calculated 3D displacement distribution. No significant differences have been observed for the investigated structures. On the other hand, this restriction to rotational symmetry of the displacement field helps to speed up the calculations for the transformation into reciprocal space.

Limitations

The advantage of the FEM approach is that any shape and any arbitrary concentration profile can be analysed. On the other hand, the data handling is rather complicated (use of different applications) and does not allow data fitting.

One problem which arises from the FEM approach is that only a single dot solution is calculated. However, superposition is essential for growth simulations since it is impossible to compute a numerical solution of the equations of elasticity for an ensemble of 10^3 dots. P. Mayer [Mayer01] has shown that, despite the linearity of the equations of elasticity, the superposition

of single-dot solutions is not a rigorous solution for a multi-dot problem due to the different elastic constants of the dots and the surrounding material. However, the approximation is good (error $< 1\%$) as long as the inter-dot distance is larger than the base edge length of a dot, which is fulfilled for the investigated quantum ring samples.

Another important question is the applicability of the linear continuum description as the dimensions of the dots are on a nanoscale. FEM program packages (just like elasticity theory in general) are conceived in order to solve macroscopic problems. They ignore the discontinuous atomic structure of matter and the existence of crystal lattices in solids. C. Pryor et al. have compared the calculated strain distribution of an InAs dot grown on a GaAs substrate using *continuum elasticity* and *atomistic elasticity* [Pryor98]. Deviations of the results between the two theories were found at the highly strained interfaces of the dot. In these regions the system is outside the linearity regime of the continuum theory. In the surrounding material the results agreed within 0.5%.

The problem with atomistic calculations is that they can be used only for a limited number of atoms. Assuming a simulated volume with a lateral size of 200nm and 35nm in height about 20000 unit cells have to be considered for a two-dimensional simulation. For a three-dimensional calculation taking into account the full elastic anisotropy of the system several millions of unit cells have to be analysed.

Another method [Flocken70, Holý99] based on a continuum approximation can calculate a numerical solution of the strain profile. This method contains rather simple calculations - but only for flat surfaces.

2.3.3 Example using Patran/Nastran

For the FEM calculations the commercial software package PATRAN/NASTRAN by MSC. Software has been used. This program is installed on a SGI Origin 3800 server with 128 CPUs at the computer centre of the University of Linz, Austria.

PATRAN is the pre- and post-processor for the model analysis, having an interface for NASTRAN, which is the numerical processor to solve the equations of elasticity. It was used in the version 2001 r2, 2001 r3, 2003, and 2003 r2. PATRAN has a CAD-like user interface for the construction of the finite-element model, but it can also be completely controlled by batch files. This latter option has been used, as it allows for an easier modification of fit parameters of the simulation, like radius, height, concentration profile, etc. The batch files were created using MATLAB scripts.

In the following the fundamental steps for the FEM simulation of a buried quantum dot structure using PATRAN/NASTRAN will be explained. Fig. 2.18 shows a screenshot of the user interface of PATRAN. A detailed description can be found in the online documentation or in the diploma thesis of Peter Mayer, who has used this FEM package for the simulation of strain in quantum dots [Mayer01].

The first step for the design of the FEM model is to define the **crystal orientation**. For the models which are discussed within this thesis the z direction was chosen for the surface normal [generally the (001) direction, but (110) in the case of the CEO sample]. The x axis defines the in-plane direction.

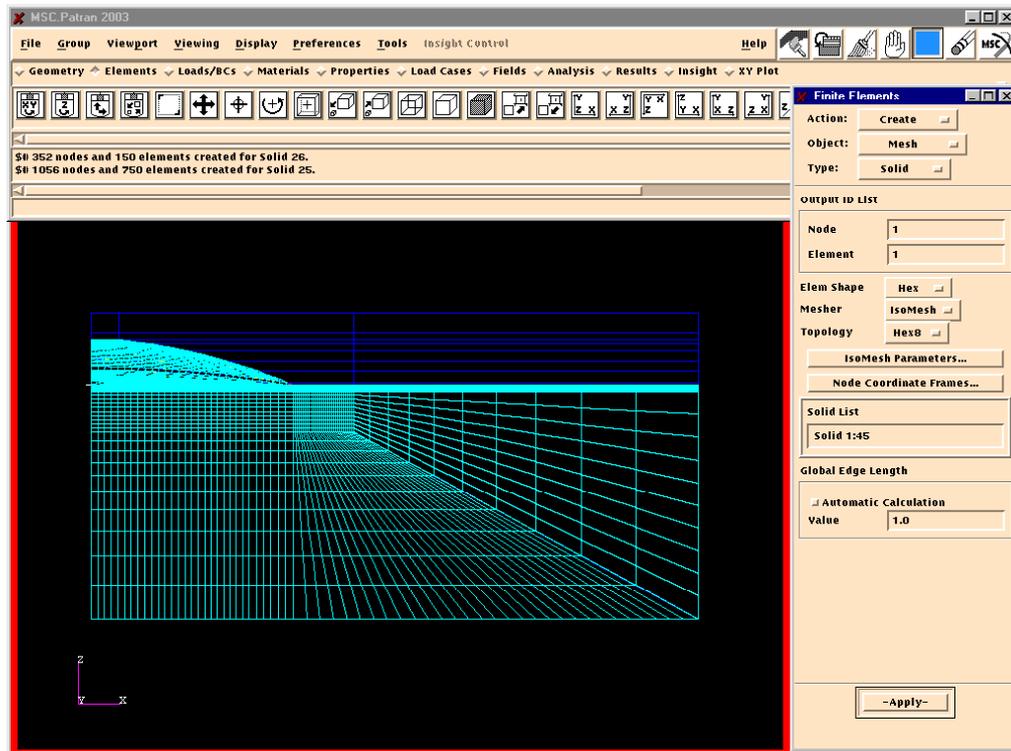


Figure 2.18: User interface of the FEM preprocessor PATRAN showing the design of a buried quantum dot.

The shape of the quantum structures is based on assumptions and AFM data, if available. It has to be refined in the following fitting process. Therefore, care should be taken that the design allows for an easy change of fit parameters, like radius and height of the quantum dot. For the present example a GaAs (001) substrate is assumed. On top of it an $\text{In}_{0.5}\text{Ga}_{0.5}\text{As}$ wetting layer is grown. After a few monolayers Stranski-Krastanov growth starts and forms a quantum dot having a concentration gradient of InAs towards its apex. This structure is completely buried in a GaAs cap layer.

The model is first constructed in the (110) plane and extruded to a 45° wedge later on. The 2D design is shown in Fig. 2.19. The simulation starts with the definition of the **points** building up the structure. After that each two points are used to form **curves**. Here it is important to pay attention on the direction in which these lines are defined. If necessary several curves are combined to **chains**. In the present case this has been used to create curved lines limiting the different iso-concentration planes within the dot volume. Now, each two curves (or chains) are used to define **surfaces**. Again one has to pay attention on the correct orientation of the curves to form *plane* surfaces.

The next step is to extrude the 2D design into a 45° wedge transforming the surfaces into so-called **solids**. Fig. 2.20 shows the extruded FEM model. It consists of 88 points, 84 lines, 8 chains, 45 surfaces, and therefore 45 solids.

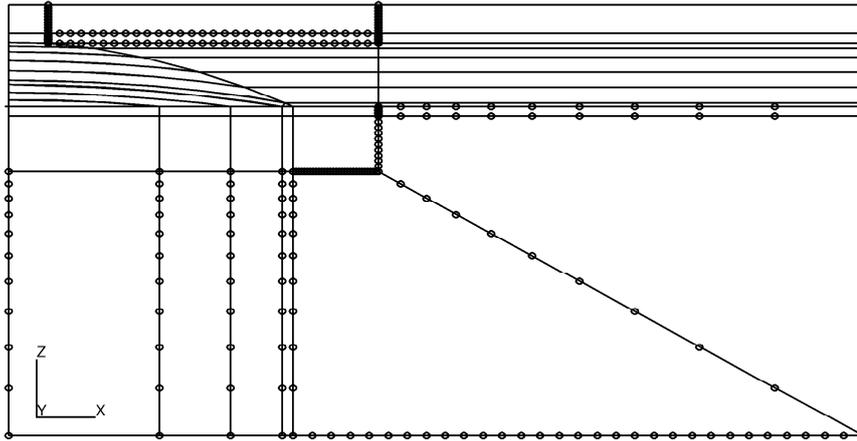


Figure 2.19: FEM model of a buried quantum dot in 2D. The dot volume and the surrounding matrix has already been subdivided for an appropriate definition of the concentration profile and mesh size, respectively.

In the following the solids have to be divided into “**finite elements**”. In the design shown in Figs. 2.19 and 2.20 the dot volume and the surrounding matrix has already been subdivided to facilitate an appropriate definition of the concentration profile and mesh size, respectively. A high mesh density is necessary for regions where strong gradients of the strain field are expected, whereas the remaining part is meshed with lower density to keep the total number of nodes as small as possible. Another important constraint is that the number of nodes on lines (or surfaces) which several elements have in common has to be the same on both sides. Otherwise the “*equivalence*” process (see later) doesn’t work correctly. It could cause solids which are not connected to each other. This fact has to be taken into account especially for the construction of the substrate and the cap layer: due to the subdivision of the dot volume into different iso-concentration planes the neighbouring cap layer or substrate cannot be created as a single solid. In contrast, each point on the surface of the dot has to define a new solid. In the region below the dots several solids have to be created for the same reason.

In the region in the dot and very close to it stronger strain gradients are expected. Therefore, the mesh density in this region is increased. The FEM grid extends far into the substrate. Here the density of the grid is gradually decreasing with distance from the island, because the distortions are very small. The mesh density is controlled by defining a **mesh seed**. Curves having a mesh seed are marked with little circles in Figs. 2.19 and 2.20. For the remaining lines a default value is defined.

Fig. 2.21 shows the finished mesh for one plane. It was created with so-called “Hex8” elements (hexahedral elements with 8 nodes) using “Isomesh”, which creates equally spaced nodes along the edges, if not defined differently. The next step is to analyse the “**equivalence**” of the created nodes. In this process all nodes that co-exist at a certain point are reduced to a single node. At the end of this procedure the structure contains 97660 nodes (before it had 115033 nodes). The aim of the following **optimisation** is to re-number the nodes or elements of a model in such a way that the stiffness matrix assembled in the finite-element analysis can be solved by using a minimum of CPU time, memory, and disc space.

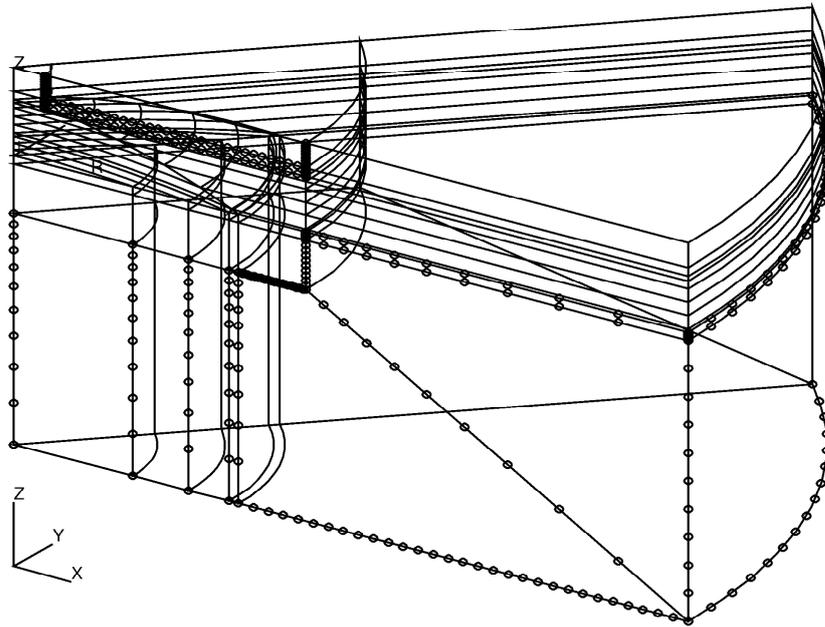


Figure 2.20: FEM model extruded to a 45° wedge. It consists of 88 points, 84 lines, 8 chains, 45 surfaces, and therefore 45 solids.

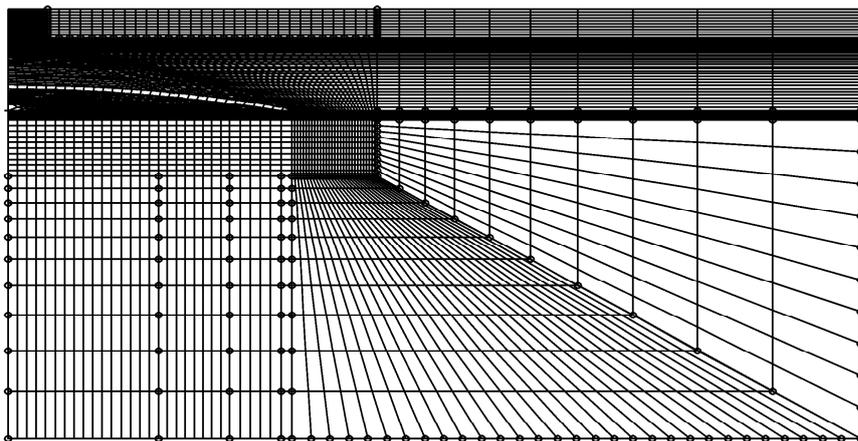


Figure 2.21: FEM model filled with an appropriate mesh. In regions where higher strain gradients are expected the mesh density is increased.

The next important step is the definition of **boundary conditions and loads**. As no external forces act on the model structure, the only boundary conditions which have to be defined have already been explained in the previous sub-chapter. The nodes at the bottom and at the circumference of the wedge are fixed. The nodes at the side faces of the wedge can move only within the faces, but cannot move perpendicularly, according to the symmetry. The top surface of the grid is completely free and can relax elastically. In addition, a temperature increase of 1K to 301K has been defined as boundary condition. The last step before the FEM calculation can be started is to define the used **materials** and to assign these materials to the created solids. For each alloy a new “material” has to be defined. For each material the elastic constants c_{ijkl} and the thermal expansion coefficient α according to Eq. 2.54 for a reference temperature of 300K has to be assigned. The full 3D anisotropy of the system is taken into account. The elastic constants for InAs and GaAs have been taken from Ref. [Madelung92], all properties of alloys are obtained by linear interpolation between these two materials. According to the orientation of the surface normal (z direction) the tensor of the elastic constants c_{ijkl} may have to be transformed to another coordinate system (see chapter 5).

After the pre-processing stage is finished, the equations of elasticity are solved numerically by the numerical processor NASTRAN. It calculates the displacement field in x - and z direction as well as the components of the strain tensor.

The result is imported again to PATRAN and visualised together with the mesh grid. The calculated displacement field of the buried quantum dot in x direction u_x is shown in Fig. 2.22 for the 45° wedge. In this graph the displacement per calculated finite element is plotted. Therefore, interfaces of the iso-displacement areas look rough. Fig. 2.23(a) shows the same information. However, in this graph only the u_x - u_z plane is shown and the results are smoothed. Fig. 2.23(b) shows the x component of the strain tensor ε_{xx} . Clearly the strong compressive strain at the lower right corner of the quantum dot can be observed. For this reason a high mesh density was chosen for this region.

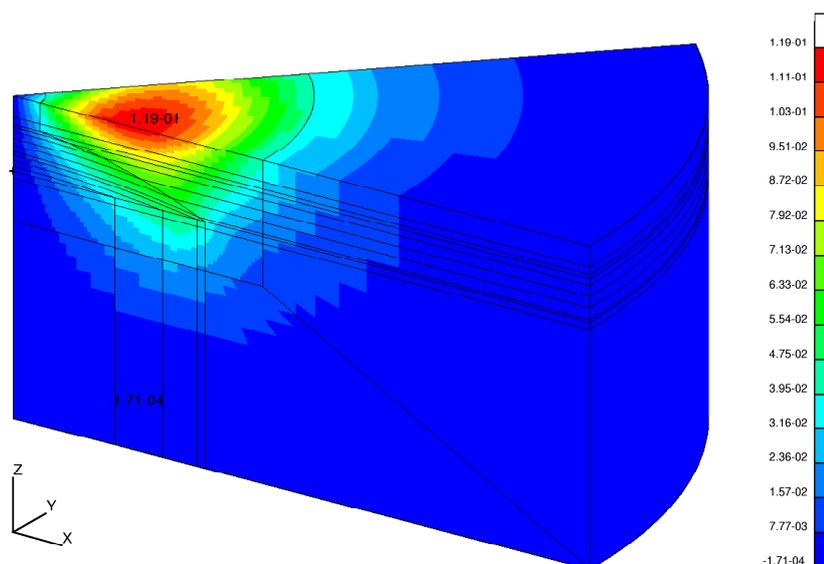


Figure 2.22: FEM simulation of the displacement field u_x calculated for the 45° wedge. The colour scale is given in nm.

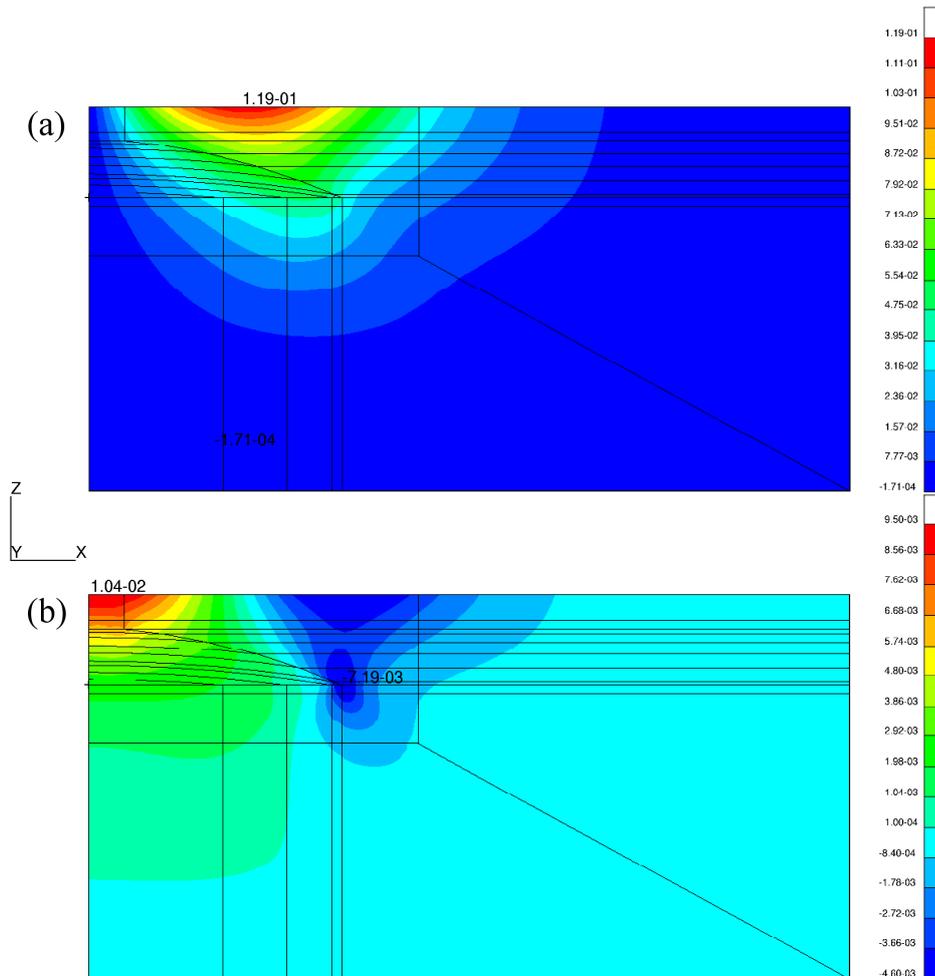


Figure 2.23: FEM simulation of the displacement field u_x (a) and strain ε_{xx} (b) calculated for the x - z plane.

By simulating the same quantum dot with different sizes of the substrate one has to make sure that the simulation cell has no influence on the calculated displacement field, i.e. the cell is “quasi-infinite”.

For the calculation of the reciprocal space maps the calculated displacement field is exported into a two-dimensional rectangular lattice with equally spaced points. These maps will be shown in chapter 4 in more detail. The input parameter of the FEM simulation (especially shape, size, and concentration profile of the dots) have to be refined until a good agreement between experiment and simulation is achieved.

Chapter 3

Quantum dots

3.1 Motivation

Interdiffusion plays an important role during the growth of quantum dots by Stranski-Krastanov self-organisation [Joyce98]. However, difficulties in the quantification of the composition profile inside the dots along the growth direction remain [Liu00, Rosenauer00, Walther01, Crozier01, Hsu03]. On the other hand, the knowledge on interdiffusion and the resulting strain is important for device applications as electrons and holes are not confined by rigid structural boundaries, but only by the composition gradient [Liu00]. Therefore, the composition profile inside the dots plays a more important role for the effective confining potential of the charge carriers than the shape of the islands.

In the following contrast variation by anomalous diffraction at a weak superstructure reflection is used for a direct determination of the strain and interdiffusion profile of free-standing InGaAs quantum dots.

Investigated samples

The samples investigated in this chapter have been provided by E. Beham of the group of Prof. G. Abstreiter at the Walter Schottky Institute in Garching, Germany.

All samples are based on GaAs (001) wafers which were overgrown by a buffer layer of 6000Å GaAs. In the following one sample with free-standing $\text{In}_{0.5}\text{Ga}_{0.5}\text{As}$ QDs, one sample with buried QDs, and two samples with a double layer of QDs were prepared by molecular beam epitaxy (MBE). The differences between these samples are summarised in table 3.1. The $\text{In}_{0.5}\text{Ga}_{0.5}\text{As}$ quantum dots were grown by Stranski-Krastanov self-organisation at a temperature of 500°C. The buffer layer and the capping layer were deposited after a growth interruption of 10sec, each.

The growth of a double layer of self-assembled QDs separated by a thin barrier is one approach towards vertically aligned coupled QDs. The use of such “artificial molecules” has been suggested as a possible implementation of one- or two-QuBIT gates for quantum computing [Loss98].

Sample	QD layer	coverage	QD layer
free-standing QDs	8ML $\text{In}_{0.5}\text{Ga}_{0.5}\text{As}$		
buried QDs	8ML $\text{In}_{0.5}\text{Ga}_{0.5}\text{As}$	100Å GaAs	
double layer 1	8ML $\text{In}_{0.5}\text{Ga}_{0.5}\text{As}$	70Å GaAs	8ML $\text{In}_{0.5}\text{Ga}_{0.5}\text{As}$
double layer 2	8ML $\text{In}_{0.5}\text{Ga}_{0.5}\text{As}$	130Å GaAs	8ML $\text{In}_{0.5}\text{Ga}_{0.5}\text{As}$

Table 3.1: Important growth parameters of the investigated InGaAs quantum dot samples.

The electronic coupling of a two-fold stack of self-aligned $\text{In}_{0.5}\text{Ga}_{0.5}\text{As}$ QDs embedded in a n-i-Schottky junction has been investigated by Krenner et al. using photoluminescence (PL) experiments [Krenner02].

The surface morphology of the four samples was investigated by atomic force microscopy (AFM). Grazing incidence small angle scattering (GISAXS) was used to look for vertical correlations between the two-fold stack of self-assembled QDs. However, according to these investigations there is no evidence for a coupling between the two layers. Therefore, in the following only the measurements in grazing incidence diffraction (GID) are described in detail. Anomalous diffraction is used to determine the composition of the free-standing InGaAs QDs as a function of the lateral lattice parameter ("strain"). The simulation of angular measurements together with the AFM investigations allow to attribute the strain and the InAs concentration to a certain height in the quantum dots.

However, the discussion of the measurements taken on the buried $\text{In}_{0.5}\text{Ga}_{0.5}\text{As}$ QDs and free-standing islands grown on the strain modulated surface of a buried QD layer will show the limits of the contrast variation technique.

3.2 Atomic Force Microscopy

3.2.1 Experiment

The four samples listed in table 3.1 have been investigated using a *Digital Instruments Nanoscope Dimension 3100* atomic force microscope at the Center for Nanoscience in Munich. The ex-situ micrographs have been taken in Tapping Mode. In Figs. 3.1 to 3.4 two images per sample are shown, one with a side length of $5\mu\text{m} \times 5\mu\text{m}$, the other one with a side length of $500\text{nm} \times 500\text{nm}$.

Fig. 3.1 shows the surface morphology of the free-standing single layer of InGaAs QDs. The nanostructures are dome-shaped with a circular base of an average diameter of $(30 \pm 10)\text{nm}$ and a height of about $(7 \pm 1)\text{nm}$. The images show the formation of clusters with a preferred orientation along one of the $\langle 110 \rangle$ directions. A similar arrangement of nanostructures has already been reported [Sudijono92, Brault98] and is explained by the greater In adatom surface diffusion along the $[1\bar{1}0]$ direction for As-stabilised surfaces. Therefore, it is very likely that the observed preferential orientation occurs along $[1\bar{1}0]$.

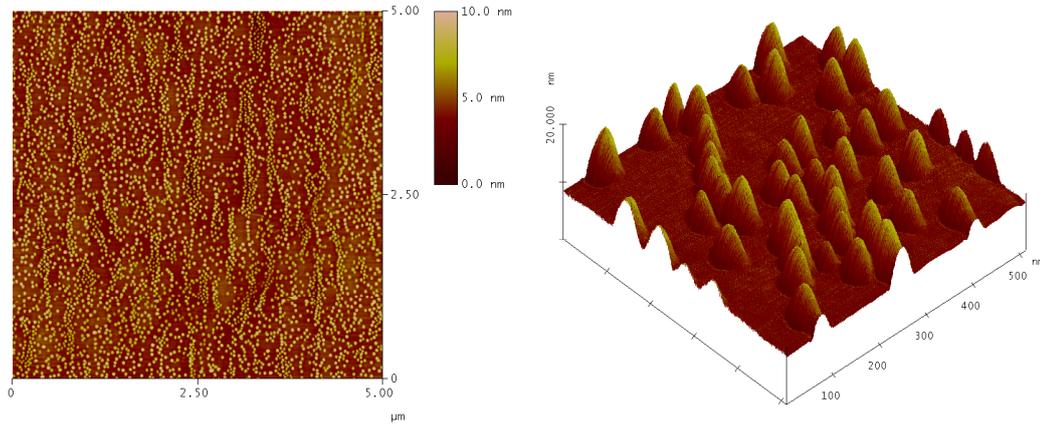


Figure 3.1: AFM image of a free-standing single layer of InGaAs QDs. The formation of clusters with a preferred orientation along $[1\bar{1}0]$ is observed.

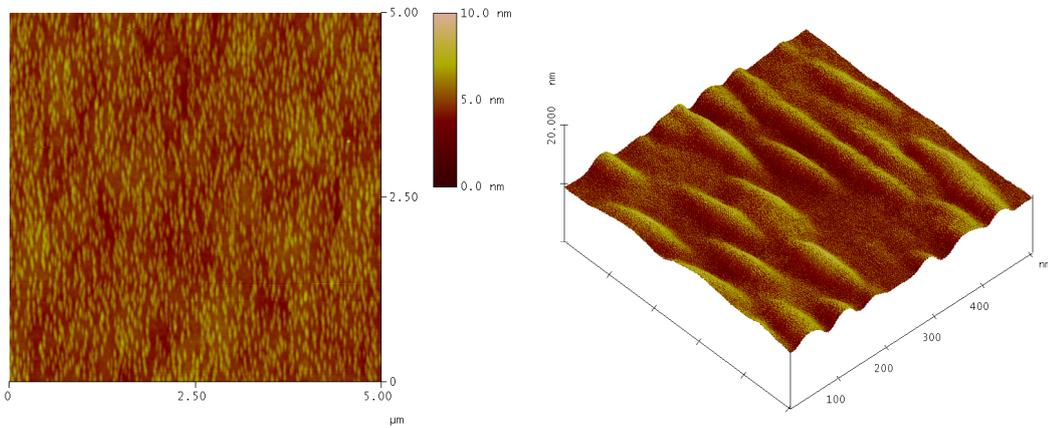


Figure 3.2: AFM image of a single layer of InGaAs QDs overgrown by 100\AA GaAs. The formation of elongated nanostructures with an average height of about $(2 \pm 1)\text{nm}$ along $[1\bar{1}0]$ is observed.

Fig. 3.2 shows the surface morphology after capping a single layer of QDs with 100\AA GaAs. The overgrowth results in elongated nanostructures with an average height of about $(2 \pm 1)\text{nm}$. Again, the orientation of the nanostructures is most likely along $[1\bar{1}0]$.

In Figs. 3.3 and 3.4 micrographs of the two samples with a double layer of QDs are presented. The free-standing InGaAs QDs in the second layer are again dome-shaped with a circular base of an average diameter of $(30 \pm 10)\text{nm}$ and a height of about $(7 \pm 1)\text{nm}$. In the case of the spacer layer with a thickness of 70\AA GaAs (Fig. 3.3) the surface morphology is very similar to the sample with a single layer of free-standing QDs (Fig. 3.1). In both cases the formation of clusters with an preferred orientation along the $[1\bar{1}0]$ direction is observed. However, the second layer of the quantum dots grown on top of a spacer layer of 130\AA GaAs (Fig. 3.4) shows a more homogeneous distribution of the nanostructures.

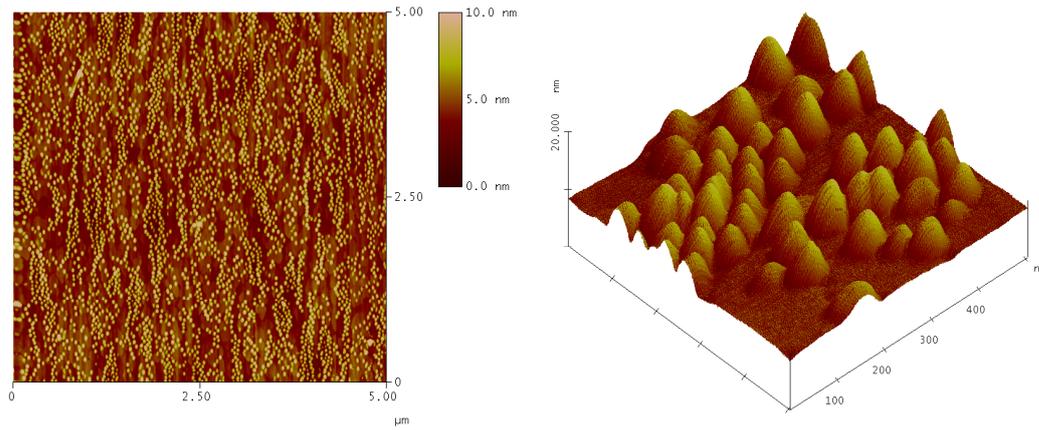


Figure 3.3: AFM image of the sample with a double layer of InGaAs QDs separated by a spacer layer of 70\AA GaAs. The surface morphology is very similar to the micrographs shown in Fig. 3.3 (single layer of QDs).

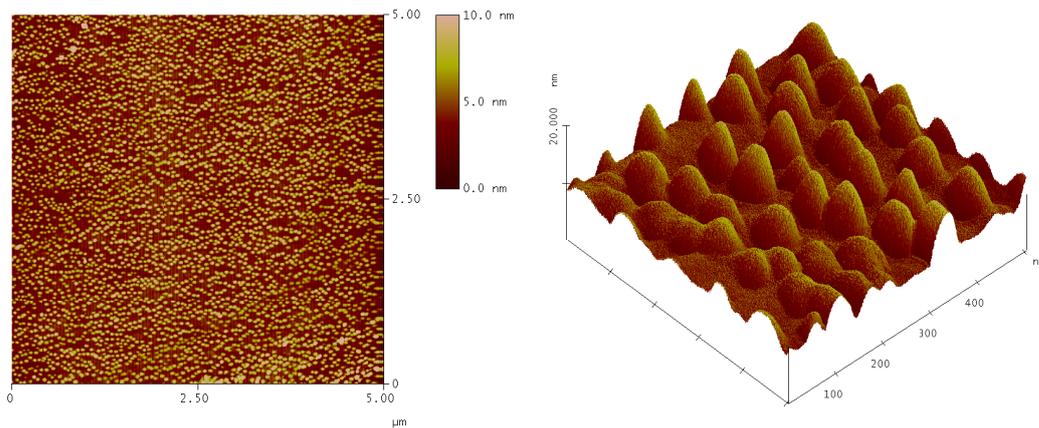


Figure 3.4: AFM image of the sample with a double layer of InGaAs QDs separated by a spacer layer of 130\AA GaAs. The nanostructures are distributed homogeneously on the surface.

These observations might explain the results from PL measurements by Krenner et al. [Krenner02]. They observe pronounced coupling effects between the two layers of $\text{In}_{0.5}\text{Ga}_{0.5}\text{As}$ QDs embedded in a n-i-Schottky junction for a spacer layer thickness of 70\AA . The identical (not embedded) structure (see Fig. 3.3) shows a strong replication of the cluster formation as it occurred most likely during the growth of the first layer of QDs. This suggests vertical correlations between the two QD layers. A strong decrease of the electronic coupling was observed with increasing spacer thickness up to 130\AA , though. Due to the homogeneous QD arrangement of the corresponding sample shown in Fig. 3.4 vertical correlation between the two layers should be less pronounced, assuming again a first QD layer with strong cluster formation.

3.2.2 Discussion

In order to estimate the influence of the buried dot layer on the growth of a second layer of QDs, the distribution of the elastic energy density at the cap layer surface has been calculated. To this end, a Fortran program by V. Holý [Holý99, Chamard03b] was used. The model is based on elasticity theory and assumes a buried InGaAs dot with a circular base of 30nm diameter and a height of 3nm grown on a GaAs (001) substrate. The thickness of the capping layer varies between 70Å and 130Å GaAs. The calculated difference ΔE between the local energy density and the energy density of a homogeneous pseudomorphic wetting layer is presented in Fig. 3.5.

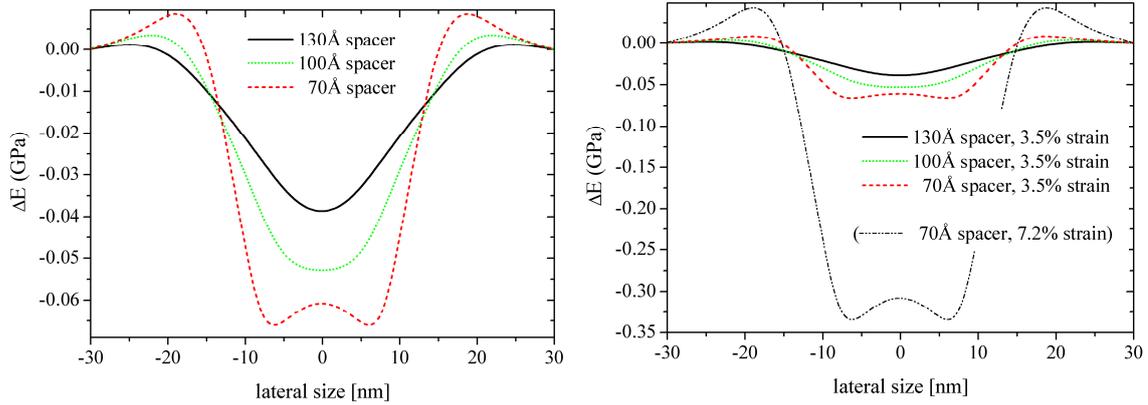


Figure 3.5: Difference ΔE between the energy density of a homogeneous pseudomorphic wetting layer and the local energy density above buried $\text{In}_x\text{Ga}_{1-x}\text{As}$ QDs assuming different thicknesses of the capping layer. The left image shows calculations for an concentration of $x = 0.5$ (3.5% lattice mismatch). In the right figure additionally ΔE for InAs islands ($x = 1.0$, 7.2% lattice mismatch) buried under 70Å GaAs is presented.

In Fig. 3.5 (left) the elastic energy distribution above $\text{In}_{0.5}\text{Ga}_{0.5}\text{As}$ QDs assuming different thicknesses of the capping layer is calculated. For a spacer layer of 70Å two minima located on both sides of the origin (i.e. centre of the dot base) can be observed. However, as the distance between the minima is smaller than the base size of the dot (30nm diameter) the growing QDs are only sensitive to a broad and flat minimum as in the case of 100Å and 130Å capping. The size of the energy minimum is comparable to the base diameter of the overgrown islands. For the nucleation of the next layer of QDs on the thereby strained surface, the most probable location is at the origin. This suggests that vertical ordering can be expected.

However, with increasing spacer layer thickness from 70Å to 130Å the depth of the energy minimum is decreased by a factor of two. This explains the decreasing tendency of vertical ordering for increasing thicknesses of the spacer layer.

Furthermore, the InAs concentration and therefore the elastic strain originating from the buried QDs is of importance. For the calculations presented in Fig. 3.5 (left) an InAs concentration of 50% has been assumed, i.e. a lattice mismatch of 3.5%. In Fig. 3.5 (right) the same curves are plotted again together with the calculation for a buried island of pure InAs (mismatch 7.2%). The increase of ΔE is tremendous (factor of 6.5). Thus, the expected strain induced vertical ordering of $\text{In}_{0.5}\text{Ga}_{0.5}\text{As}$ islands (being already less pronounced as compared to other systems, e.g. GaN/AlN [Chamard03b]) is strongly reduced and might explain why in GISAXS measurements vertical intensity modulations due to vertical coupling could not be observed.

3.3 Grazing incidence diffraction

The x-ray measurements have been performed in the grazing incidence diffraction geometry at the beamline ID1 of the ESRF in Grenoble. The incident angle was set to $\alpha_i = \alpha_c - 0.05^\circ = 0.15^\circ$.

For the characterisation of the shape, strain, and interdiffusion profile of the (free-standing) QDs the technique of iso-strain scattering (ISS) has been applied [Kegel01].

Note that within this model (lateral) “strain” is always used in the sense of lateral “*lattice parameter compared to the GaAs lattice constant*” and does *not* depend on the actual InAs concentration. For example, $\text{In}_{0.5}\text{Ga}_{0.5}\text{As}$ with a lattice mismatch of about 3.5% relative to GaAs is relaxed. However, it is regarded as an iso-strain area with 3.5% strain with respect to GaAs.

The ISS technique is well suited to analyse free-standing QDs where the in-plane lattice parameter is a monotonic function of the height. The QDs are expected to be pseudomorphically grown on the substrate and elastically relaxed towards the top. In this case each height in the dot has its own lattice parameter, and scattering from that region will appear at a certain value of q_{rad} in reciprocal space. Each of these iso-strain areas gives rise to a characteristic form factor of the scattered intensity. The lateral size of an iso-strain area is determined by investigating its form factor in angular direction. The composition can be determined using the technique of contrast variation introduced in the previous chapter. The ISS model is best applicable if the lattice parameter gradient in growth direction, the lateral size of the nanostructures, and their height are large. The larger radius results in a smaller width of the corresponding shape function and together with the other preconditions in a better separation of the iso-strain areas. Measuring higher indexed reflections can be of advantage as the strain-induced distribution is spread out on a larger Q -range, whereas the form factor distribution in Q -space does not depend on the studied reflection.

For the investigation of the four QD samples, radial scans around the (200) surface reflection have been recorded at 11.630keV, 11.856keV, and 12.380keV to determine the InAs concentration as a function of the lateral lattice parameter. At 12.380keV angular scans for several radial positions have been recorded to determine the lateral size of the corresponding iso-strain area. This size information is fitted into the cross-section profile of a quantum dot as derived from AFM micrographs to associate the iso-strain area to a certain height within the dot. If all results are combined a three-dimensional model of the strain and interdiffusion profile of the free-standing InGaAs quantum dots can be reconstructed.

It has to be noted that the contrast variation technique in combination with the ISS model is limited to the analysis of single layers of free-standing QDs (see Sect. 3.3.3 and 3.3.4).

3.3.1 Contrast variation by anomalous diffraction

As has been demonstrated in Fig. 2.3, the contrast between measurements at an energy of 11.856keV and 12.380keV provide the highest possible contrast between InAs and GaAs. Therefore, measurements at these two energies have been used for the determination of the InAs concentration. Since the composition is calculated from the ratio between two intensities, all background contributions have to be subtracted before comparison.

Fig. 3.6 shows the measurements (without background) for the sample with a single layer of free-standing quantum dots. The measurement at 11.856keV is plotted with circular symbols in black, the measurement at 12.380keV with triangular symbols in red. The thin lines are theoretically calculated intensities for an easy quantitative interpretation of the graph. The curves are calculated from the measurement at 11.856keV (10eV below the K edge of As) which is used as a reference. By increasing the x-ray energy to 12.380keV (above the K edge of As) the relative intensities from the dots and the substrate undergo a significant change. The scattered intensity of GaAs is suppressed by a factor of 44.6 as compared to the GaAs intensity at the lower energy. The InAs scattering is reduced only by a factor of 1.7. Thus, assuming nanostructures of pure GaAs, at 12.380keV an intensity 44.6 times lower as compared to the measurement at 11.856keV is expected. This is plotted as the thin black (solid) curve. On the other hand, the scattered intensity of QDs of pure InAs would be only lowered by a factor of 1.7 which is depicted as the light blue line (dash dot dot). Additionally, the expected intensity for an InAs concentrations of 10%, 30%, and 60% have been calculated. The technique is especially sensitive for small InAs concentrations due to the non linearity of the relation between contrast and concentration. The InAs concentration as a function of the lateral lattice parameter (i.e. strain with respect to GaAs) can now be easily determined by comparing the intersections of the measured curve at 12.380keV with the theoretically calculated curves of a particular InAs concentration. As the measurement never crosses the dark blue line (dash dot) the maximum InAs concentration in the structure is below 60%.

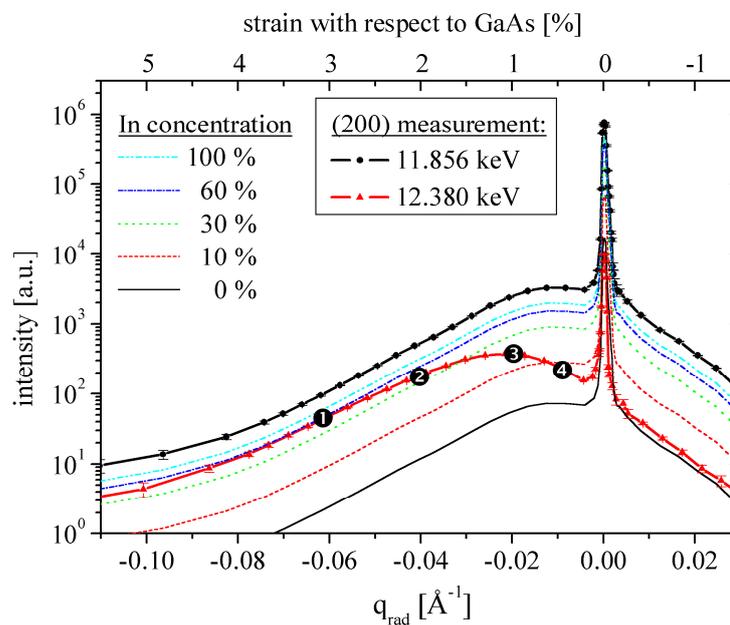


Figure 3.6: Investigation of free-standing InGaAs QDs by radial scans around the (200) reflection at 11.856keV and 12.380keV. The thin lines, calculated from the measurement at 11.856keV, indicate iso-concentration lines for the interpretation of the scan at 12.380keV. See text for more details. The scattering background is already subtracted. The black dots mark the radial positions where angular measurements have been taken (see next sub-chapter).

The results are summarised in Fig. 3.7 which shows the evaluated composition as a function of the local in-plane lattice parameter for the free-standing single layer of QDs. For $q_{\text{rad}} < -0.06 \text{ \AA}^{-1}$ the measured intensity is very close to the background level, which increases the error of the determined concentration. Due to the non-linear relation between contrast and concentration, the error bars (yellow hatched area) lie asymmetrically around the determined value (red line). The black dots mark the radial positions where angular measurements have been taken. The evaluation of these scans is discussed in the following sub-chapter and will give information about the size and thus the height of the corresponding local in-plane lattice parameter in the QD.

A preliminary interpretation of Fig. 3.7 shows that interdiffusion plays an important role during the QD formation. This is concluded from the fact that in areas of the QDs with a lattice parameter close to GaAs the determined InAs concentration is clearly below the nominal InGaAs concentration of 50%. On the other hand, in the states with highest strain relative to GaAs the InAs concentration is in the order of the nominal value.

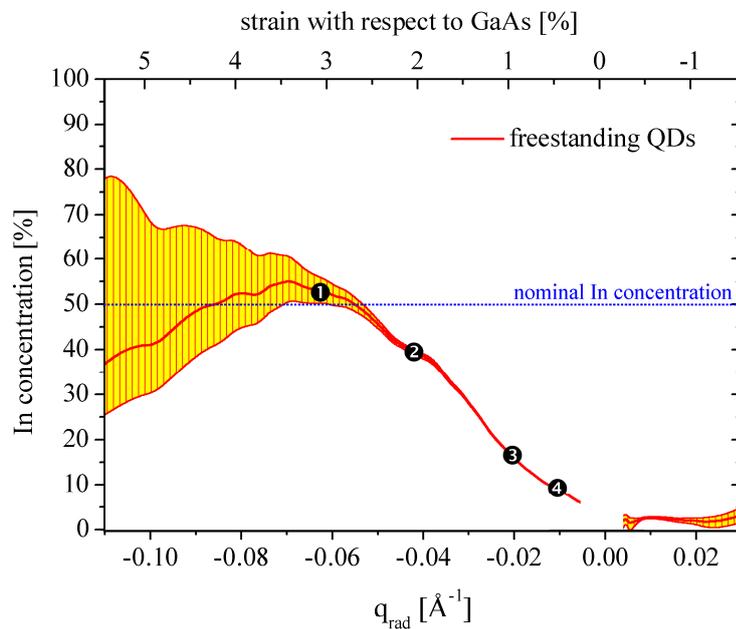


Figure 3.7: InAs concentration in a single layer of free-standing InGaAs QDs as a function of the local in-plane strain with respect to GaAs (upper scale). The black dots mark the radial positions where angular measurements have been taken (see next sub-chapter). Close to the GaAs substrate peak a determination of the composition is not possible because of the large gradient of the measured curves.

Another interesting conclusion can be drawn from the measurement at $q_{\text{rad}} > 0 \text{ \AA}^{-1}$. In this part in-plane lattice parameters are investigated which are compressed to values below the lattice constant of GaAs. Since the determined InAs concentration in this area is larger than zero ($\approx 3\%$) the scattering is attributed to a compressive ring situated in the substrate around the base of the QD. This is illustrated in Fig. 3.17 showing the FEM simulation of a free-standing InGaAs QD. The maximum lattice expansion (6.8% for the chosen simulation parameters) is located at the apex of the QD. The maximum compression (-1.9%) can be found in a compressed ring surrounding the QD in the wetting layer and the substrate directly beneath.

The intensity measured at the position of the substrate Bragg reflection would provide valuable information about the InGaAs wetting layer in-between the dots which is pseudomorphically strained to the GaAs in-plane lattice parameter. The concentration measured at this position gives directly the composition of the wetting layer which is expected to be the only area in the QD structure with an InAs concentration larger zero and an in-plane lattice parameter of the GaAs substrate. This measurement requires a very accurate determination of the intensity in the Bragg peak which was not achieved during the performed experiments.

To prove the reliability of the technique, especially concerning the accuracy of the energy determination close to the absorption edge (see chapter 2.1.3), the InAs composition for one sample has been determined from measurements at 11.856keV/12.380keV *and* 11.630/12.380keV (not shown). Since the determined InAs concentration of both ratios agrees within the error bars, the accuracy of the energy calibration is sufficient to use an energy very close to the K absorption edge of As which provides the larger contrast range.

3.3.2 Shape determination from angular measurements

The lateral size of the iso-strain areas can be determined from the simulation of the form factor in an angular scan.

The shape of QDs with a cylindrical symmetry is approximated by a disc. The form factor F of a disc with radius R calculated in polar coordinates is:

$$\begin{aligned} F(q, h) &= \int_0^{R(h)} \int_0^{2\pi} 1 \cdot \exp(iqr \cos \phi) r d\phi dr = \int_0^{R(h)} 2\pi r J_0(qr) dr = \\ &= \frac{2\pi R(h) J_1(q \cdot R(h))}{q} \end{aligned} \quad (3.1)$$

using the recursion formula for Bessel functions:

$$\frac{d}{dx} [x^n J_n(x)] = x^n J_{n-1}(x) \quad (3.2)$$

The radius R is expected to change with the height h in the QD. For the simulation a size distribution of 10% of the radius was considered and a background taking into account the thermal diffuse scattering was added.

Fig. 3.8 shows best fits for the angular measurements performed on the sample with a single layer of free-standing QDs at the surface. The angular scans have been taken at different radial positions as indicated by the numbers in Fig. 3.7. In the radial range between -0.011\AA^{-1} and -0.065\AA^{-1} which corresponds to a strain relaxation with respect to GaAs between 0.5% and 3.0% the determined radius decreases from 12.5nm to 4.4nm, respectively.

These radii were fitted into a cross-sectional profile through a QD as determined from AFM micrographs (see Fig. 3.9). In this way the lateral size as derived from the angular scans - together with the corresponding composition and lattice parameter - is associated with a certain height within the dots. For the described sample the height varies between 6.5nm and 0.7nm. This information is summarised together with the corresponding error bars in Figs. 3.10 and 3.11.

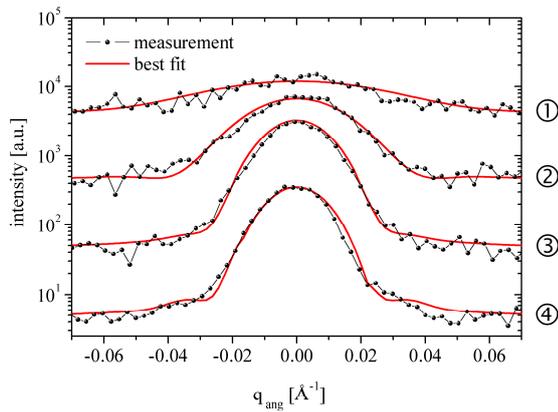


Figure 3.8: Best fits for angular measurements performed on the sample with a single layer of free-standing QDs.

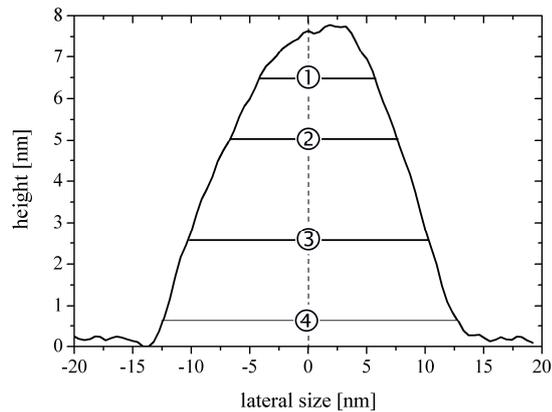


Figure 3.9: Cross-sectional profile through a QD as determined from AFM micrographs. The radii as determined from the simulation of the angular measurements shown in Fig. 3.8 are fitted into the graph.

Fig. 3.10 shows the composition profile of the investigated InGaAs QDs as a function of the height in the dots. According to the AFM studies the average height of the observed dots is about (7 ± 1) nm. Close to the base of the QDs the InAs concentration is considerably reduced as compared to the nominal growth parameter of 50% ($< 10\%$ InAs). In the case of the free-standing single layer of QDs the InAs concentration increases up to $(54 \pm 5)\%$ at the top. In Fig. 3.11 the lattice mismatch with respect to GaAs is shown as a function of the height in the dots. At the base of the dots pseudomorphic growth occurs. Towards the apex of the dot the lattice mismatch with respect to GaAs increases to about 3%.

Fig. 3.12 which combines the information of Figs. 3.10 and 3.11 gives information about the lattice relaxation with regard to the InAs concentration. According to Vegard's law [Vegard21],

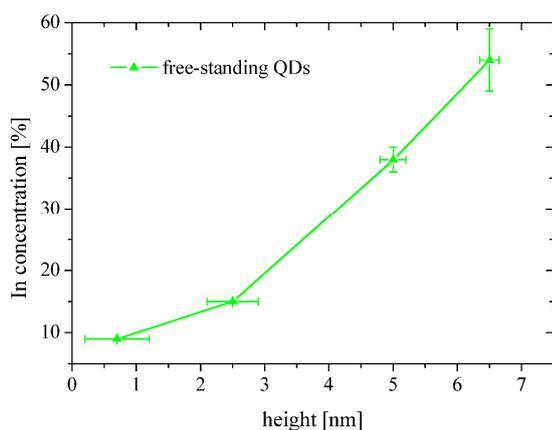


Figure 3.10: Composition profile of free-standing InGaAs QDs as a function of the height in the dots.

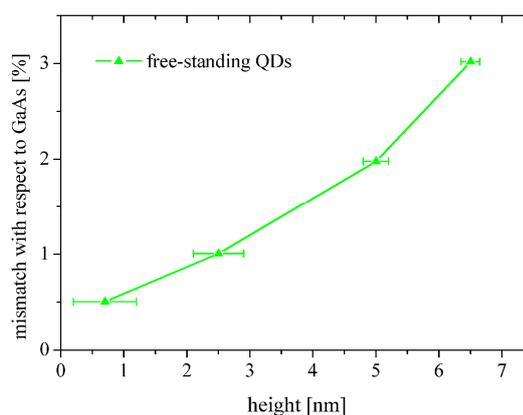


Figure 3.11: Lattice mismatch with respect to GaAs of free-standing InGaAs QDs as a function of the height in the dots.

the dashed blue line interpolates the lattice parameter linearly as a function of the InAs concentration in the alloy. The two points with a mismatch of 0.5% and 1.0% which are attributed to a height of 0.7nm and 2.5nm, respectively, agree well with Vegard's law. This indicates that the strain energy is minimised by interdiffusion. In the higher regions of the dots (measurements at 5.0nm and 6.5nm with a mismatch of 2.0% and 3.0%, respectively), the InAs concentration is higher as expected from Vegard's law. This means that the InGaAs islands cannot completely relax at the apex. It remains a compressive strain of the lateral lattice parameter of about $\Delta a/a \approx -0.6\%$ with respect to $\text{In}_{0.5}\text{Ga}_{0.5}\text{As}$.

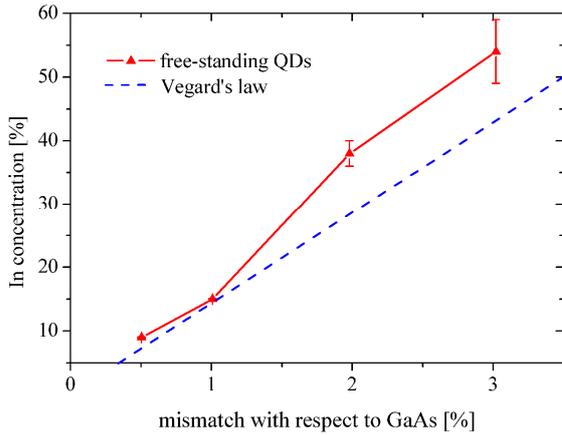


Figure 3.12: InAs concentration as a function of the lattice mismatch with respect to GaAs. The dashed line shows Vegard's law, the linear interpolation of the lattice parameter as a function of the InAs concentration.

3.3.3 Towards the limits of the contrast variation technique

The investigation of buried InGaAs QDs and of dots grown on the strain modulated surface of a buried QD layer using contrast variation by anomalous scattering reaches the limits of this technique and the ISS model. The results are discussed in the following section in more detail.

Fig. 3.13 shows the InAs concentration in the InGaAs QD double structures with a spacer layer thickness of 70\AA . Although the last QD layer is free-standing and the scattering volume is restricted to a narrow surface layer by selecting $\alpha_i < \alpha_c$ the maximum InAs concentration ($< 30\%$) differs considerably from the nominal MBE growth concentration (50%) and the investigation of the single layer of QDs shown in Fig. 3.7. The investigation of the double structure with 130\AA spacer (not shown) gives a very similar result.

In Fig. 3.14 the results of contrast variation measurements of InGaAs QDs capped with 100\AA GaAs are presented. The radial scans have been performed at an incident angle $\alpha_i = 0.25^\circ > \alpha_c$. The increased penetration depth for $\alpha_i = 0.25^\circ$ of about 650\AA allows for a more sensitive investigation of the buried QDs. Due to the capping the maximum lattice mismatch of the system with respect to GaAs is less than 2% (as compared to about 4.5% in the case of the free-standing QDs). The maximum InAs concentration seems to be less than 30% .

Finally, Figs. 3.15 and 3.16 compare directly the radial measurements performed on the free-standing single layer of QDs, the double layer of QDs (spacer with 70\AA), and the buried layer of QDs ($\alpha_i > \alpha_c$) at 11.856keV and 12.380keV , respectively. The maximum lattice mismatch with respect to GaAs decreases in the case of the double layer and especially the buried layer of QDs which is attributed to interdiffusion and the influence of the capping layer.

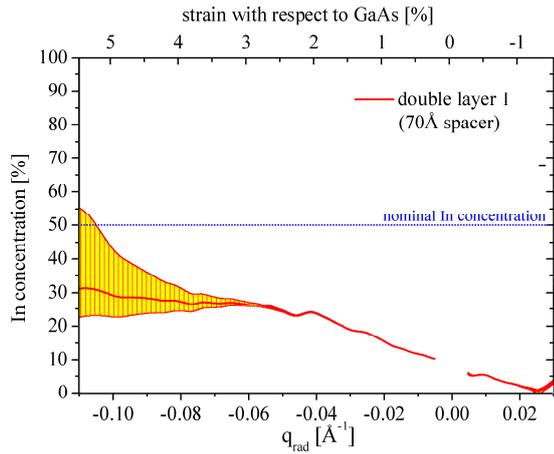


Figure 3.13: InAs concentration in the InGaAs QD double structure (70Å spacer). The measurements were performed for incident angles α_i below the critical angle α_c .

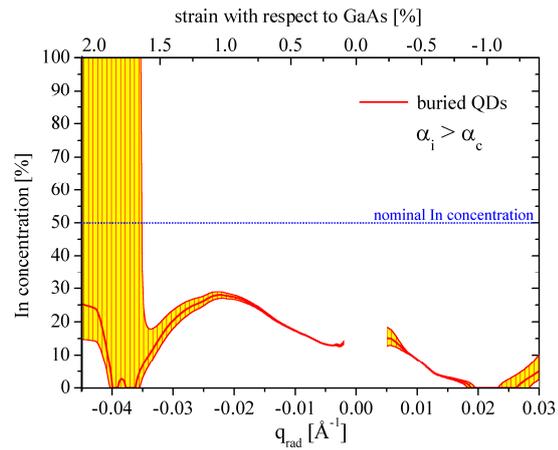


Figure 3.14: InAs concentration in a layer of buried InGaAs QDs. The measurement was performed for an incident angle $\alpha_i = 0.25^\circ > \alpha_c$ increasing the penetration depth of the x-rays to about 650Å. Note the different range of the radial measurement.

3.3.4 Discussion

The most striking result of the measurement shown in Fig. 3.13 is the maximum InAs concentration of less than 30% as compared to about 50% in Fig. 3.7. In both cases free-standing InGaAs QDs with nominally the same growth parameters have been investigated with GID under $\alpha_i < \alpha_c$. The only difference is the existence of a buried layer of QDs in case of the sample shown in Fig. 3.13. One possible explanation is the growth of a thinner wetting layer under the influence of the strain from the buried islands affecting the subsequent growth of the free-standing quantum dots.

However, it is more likely that the ISS model cannot be applied to this sample system. This can be understood by regarding finite-element calculations of a free-standing, a single buried, and a system of two coupled quantum dots in Fig. 3.17 to 3.19, respectively. The concentration profiles of all simulated dots is identical, varying between 30% and 50% InAs from the base to the top. In the figures the lateral strain profile ϵ_{xx} which is accessible for GID is plotted.

In case of the free-standing dot (see Fig. 3.17) these iso-strain areas are approximated by discs with increasing lattice parameter stacked vertically on top of each other. A small deviation of the predefined concentration profile (thin black lines) which is slightly bent downwards at the surface of the dot and the strain profile (colour scale) which is slightly bent upwards is observed. In this case the contrast variation technique always determines the *average concentration* of such an iso-strain area. This might result in an underestimation of the InAs concentration of ISS volumes at the base of the dot which extend into the GaAs substrate.

In case of the buried QD shown in Fig. 3.18 it is quite obvious that a model based on iso-strain areas cannot be applied. In this case areas having the same strain state extend over regions with a large concentration gradient. E.g. several “iso-strain” areas extend from the InAs-rich apex of the dots to the GaAs rich surface of the capping layer. Assuming that the intensity

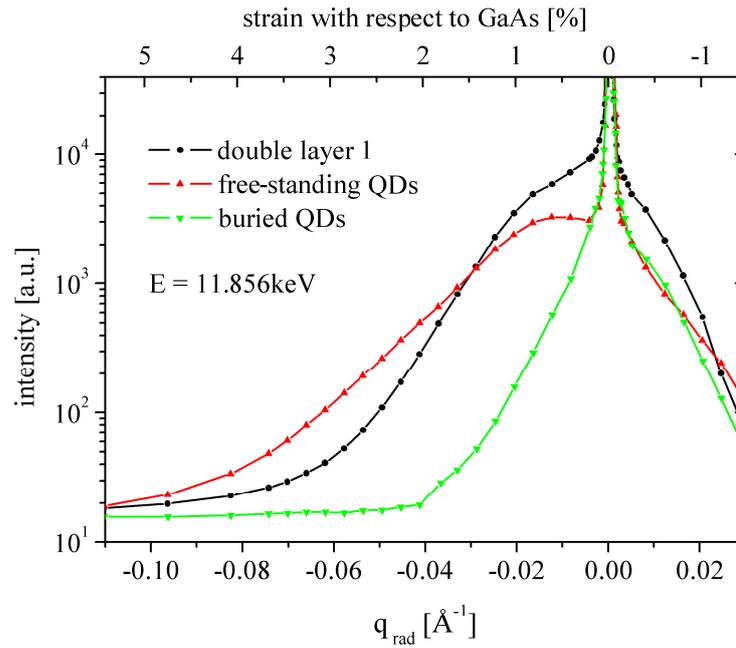


Figure 3.15: Radial scan at the (200) Bragg reflection of the free-standing single layer of QDs, the double layer of QDs (spacer with 70Å), and the buried layer of QDs at an energy of 11.856keV.

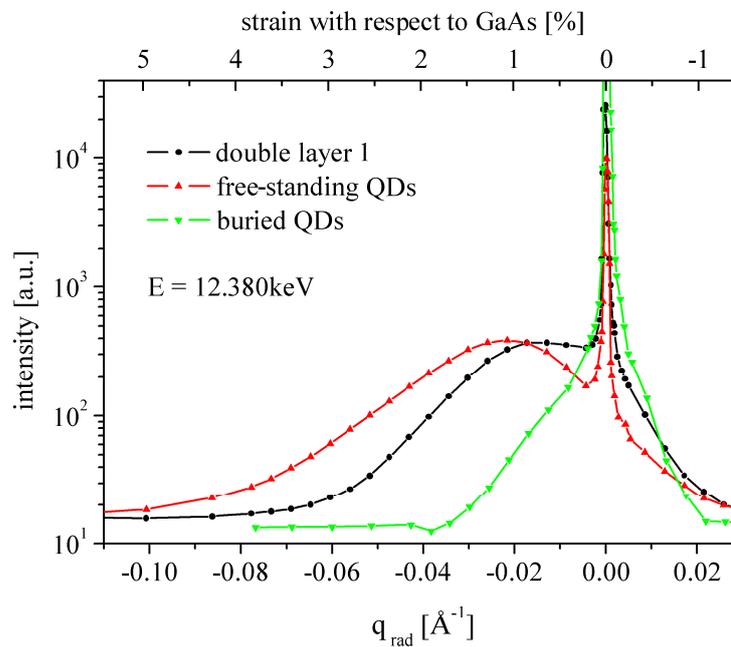


Figure 3.16: Radial scan at the (200) Bragg reflection of the free-standing single layer of QDs, the double layer of QDs (spacer with 70Å), and the buried layer of QDs at an energy of 12.380keV. The scattering of GaAs is strongly suppressed at this energy as compared to InAs scattering.

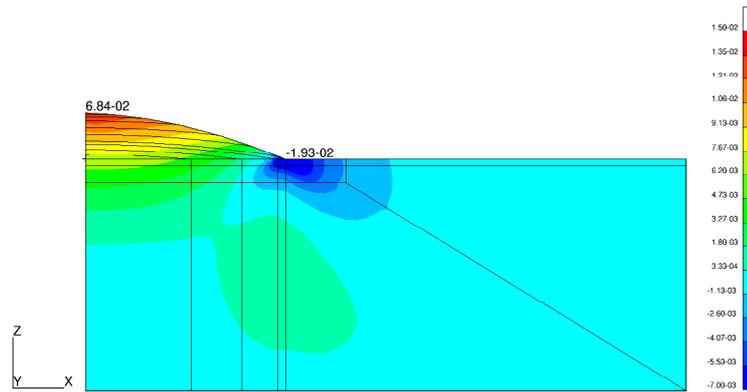


Figure 3.17: FEM simulation of the in-plane strain ϵ_{xx} of a free-standing InGaAs QD. The InAs concentration in the dot varies between 30% and 50% at the top.

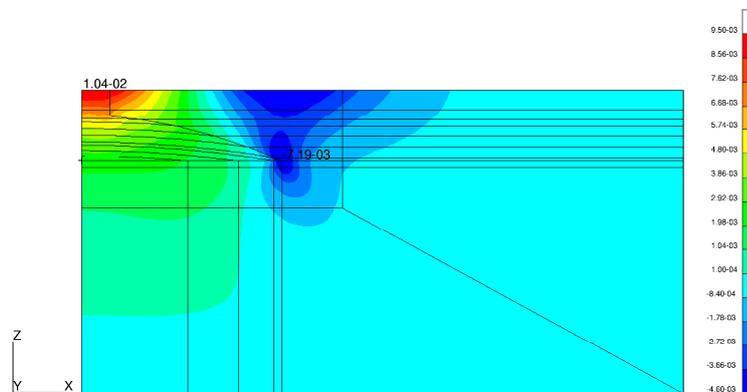


Figure 3.18: FEM simulation of the in-plane strain ϵ_{xx} of a buried InGaAs QD. The InAs concentration in the dot varies between 30% and 50%. Note the different intensity scale as compared to Figs. 3.17 and 3.19.

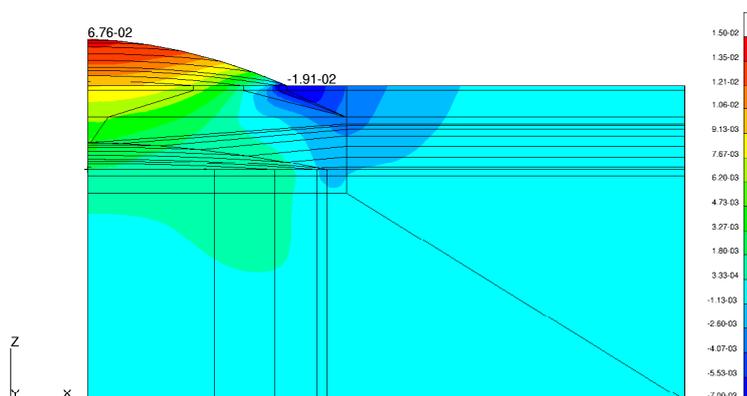


Figure 3.19: FEM simulation of the in-plane strain ϵ_{xx} of a double layer of InGaAs QDs. Both for the free-standing and the buried QDs an InAs concentration between 30% and 50% at the top was chosen.

distribution in a radial scan is *not* dominated by the shape function of particular volumes in the dot, the maximum InAs concentration of 30% derived in Fig. 3.14 can be understood by a combination of interdiffusion in the cap layer and averaging over iso-strain areas with a strong concentration gradient. In this case FEM model calculation have to be used for the quantitative interpretation of the data.

The case of the QD double layer takes an intermediate position (see Fig. 3.19). On the one hand relaxed states at the top of the upper quantum dot are unique and a correct determination of their composition should be possible. On the other hand, similar strain states in the base of the upper dot, the volume of the buried dot, and the spacer layer in between exist. Thereby, the material composition of similar strain states in this region is quite different (high InAs concentration in the buried dot, low concentration in the GaAs spacer). Therefore, a strong averaging of the determined concentration profile has to be taken into account. It has to be noted that the structure shown in Fig. 3.19 is only one example. In reality even more complicated structures can exist as the two QD layers do not necessarily have to be vertically correlated.

Another problem arises directly from the interpretation of the radial measurements as presented in Figs. 3.15 and 3.16. It is an inherent problem of the ISS analysis that it is not clear up to which q_{rad} the radial scan may be identified with a certain iso-strain area. Even in the case of a QD with only a single strain state, the finite shape of the dot results in a certain extent of the diffracted intensity in reciprocal space. Moreover, the radius of the iso-strain areas at the relaxed apex of the dots (with large “strain” with respect to GaAs) decreases which results in a broadening of the corresponding form function. At the same time the intensity of the form function decreases due to its reduced scattering volume. Therefore, it is not possible to determine exactly the maximum strain relaxation of the nanostructures directly from the radial measurement. However in the range used for the evaluation of the angular measurements on the free-standing single layer of quantum dots in section 3.3.2 this effect is certainly not significant and the ISS model can be applied.

Summary

X-ray techniques and atomic force microscopy have been used for the characterisation of free-standing $\text{In}_x\text{Ga}_{1-x}\text{As}$ islands grown on GaAs (001) by molecular beam epitaxy with a nominal concentration of $x = 0.5$. In addition, one sample with quantum dots buried under 100Å GaAs and two samples with a double layer of quantum dots have been investigated.

GISAXS was used to study the *vertical alignment* in the quantum dot double layers. However, no evidence for a vertical coupling between the two layers was found. The weak variation of the elastic energy density at the surface of the cap layer gives a possible explanation.

In order to characterise the *composition profile* of the free-standing islands, the technique of *contrast variation* by *anomalous GID* at a superstructure reflection has been applied. Using the iso-strain scattering model the technique is well suited for a *direct determination of the InAs concentration* as a function of the lateral strain in the quantum dots. In combination with atomic force microscopy a three-dimensional model of the strain and interdiffusion profile of the free-standing InGaAs QDs can be reconstructed.

For the investigated $\text{In}_{0.5}\text{Ga}_{0.5}\text{As}$ dots a strong interdiffusion of InAs is found as has been reported on similar nanostructures by Kegel et al. [Kegel01]. At the base of the islands the strain relaxes almost completely by interdiffusion whereas at the apex of the dots the lattice is compressively strained [$\Delta a/a \approx -0.6\%$ with respect to the determined InAs concentration of $(54 \pm 5)\%$].

The experimental resolution, especially concerning the separation of adjacent iso-strain volumes, would be improved by measuring higher indexed superstructure reflections [e.g. (600)]. In this case a better separation of the iso-strain areas is achieved since the strain-induced scattering will be spread out on a larger Q -range, whereas the form factor distribution in Q -space does not depend on the investigated reflection.

An accurate measurement of the intensity in the Bragg peak would allow for a direct determination of the composition of the wetting layer.

Further measurements on buried $\text{In}_{0.5}\text{Ga}_{0.5}\text{As}$ QDs and free-standing islands grown on the strain modulated surface of a buried QD layer have shown the limits of the iso-strain model and the contrast variation technique. Especially the precondition that the *in-plane lattice parameter* has to be a *monotonic function of height* is very important.

As calculated by FEM models, this condition is *only fulfilled for free-standing quantum dots*. In this case iso-strain (or better iso-lattice parameter) volumes coincide approximately with the (predefined) iso-concentration volumes. However, this is not the case for more complex structures, like free-standing quantum rings (see discussion in chapter 4).

For the investigation of *buried nanostructures* the concept of iso-strain scattering cannot be applied which makes a direct interpretation of the measurements impossible. Since the change of the lattice parameter is not a monotonic function of height the iso-lattice parameter and the iso-concentration volumes do not correspond. Therefore, the contrast variation technique only determines the *average InAs concentration* for an ISS volume and FEM simulations are required for a detailed analysis. Within this thesis FEM will be used for the characterisation of quantum rings in chapter 4.

In the case of the quantum dot double layers the restrictions for applying the methods of contrast variation and iso-strain scattering become obvious, as well. In this case, the strain modulation and InAs interdiffusion in the GaAs spacer layer results in a considerable deviation of iso-concentration and iso-lattice parameter volumes. Thus, the composition determined by contrast variation is again an average value.

Chapter 4

Quantum rings

Overgrowth phenomena deserve closer attention as the capping of quantum dots is needed for optical and electronic applications.

Several years ago, ring structures have been reported (see [Garcia97]) after capping of InAs quantum dots with a thin layer of GaAs. While the first ring structures have accidentally been grown, in recent years more effort has been put to investigate the impact of the cap layer on the structural properties of nanostructures, in particular to optimise the formation of the so-called *quantum rings*. The ring geometry makes them especially interesting for magneto-optical and electronic applications [Bayer03, Climente03, Lorke98, Lorke00, Pettersson00, Warburton00]. Different models for the process of ring formation have been proposed [Lorke01, Blossey02]. However, detailed knowledge about structural parameters like strain and interdiffusion in the quantum rings has not yet been gained. This is due to the fact that most of the publications studying the morphological change from quantum dots to quantum rings are restricted to the analysis of atomic force microscopy profiles. It is only concluded from spectroscopic investigations [Lorke02] that the ring structure consists of In rich material.

Initially quantum rings (QRs) have been observed in the material system InAs/GaAs. In recent years self-organised ring structures have been reported in InAs/InP [Raz03] and in Si/Ge [Cui03], as well.

The *first section* of this chapter describes which conditions in the growth process result in the formation of QRs. In the following, two models are presented explaining the formation process of the ring shape. The first section ends with a description of the investigated samples. In the *second sub-chapter* the experimental aspects of this work are presented. Atomic force microscopy (AFM) gives a direct image of the surface morphology. Grazing incidence small angle x-ray scattering (GISAXS) was used to investigate shape and symmetry of the QRs. Grazing incidence diffraction (GID) is able to quantify the strain and the composition within the nanostructures. As it is impossible to reconstruct directly the morphological properties of the investigated structures, model calculations have to be performed. This is described in the *third sub-chapter*. In particular finite-element calculations have been used to find out the *chemical composition* of the QRs. In *sub-chapter four* these new results are discussed and compared to the models in the literature reviewed at the beginning of this chapter.

4.1 Motivation

Self-organised InGaAs quantum rings (QRs) are observed after partial overgrowth of InAs quantum dots with a thin GaAs capping layer. A first systematic study of these MBE grown structures was performed by Garcia et al. [Garcia97]. A recent review of fabrication and spectroscopy of InGaAs quantum rings can be found in [Lorke03]. Some more details are explained in the original works of these authors [Lorke98, Lorke00, Pettersson00, Lorke01, Lorke02, Blossey02]. Morphological shape changes of QDs due to thin capping have been observed by other groups as well. The formation of InGaAs ring structures on GaAs grown by molecular beam epitaxy (MBE) has been reported in [Ferdos02, Heidemeyer02, Kamiya99, Songmuang03, Takehana03]. The growth condition for the formation of InGaAs rings by metalorganic vapour-phase epitaxy (MOVPE) is described in [Lee98]. [Raz03] and [Cui03] report on ring formation in the material system InAs/InP and Si/Ge, respectively.

4.1.1 Self-organised growth of quantum rings

A condition for the later ring formation as described by A. Lorke, R. Blossey, J.M. Garcia, et al. [Garcia97, Lorke00, Lorke01, Lorke02, Lorke03, Blossey02] is the presence of large InAs islands ($\approx 100\text{\AA}$ in height) [Joyce01b]. Therefore, 1.7ML of InAs are deposited on a (001) oriented GaAs wafer at a growth temperature of 530°C to induce Stranski-Krastanov growth of large islands. For a calibration of the growth temperature, even in different growth chambers, the change of the GaAs(2x4) reconstruction to c(4x4) which occurs at 530°C under moderate As flux is used. Finally the samples are annealed for 40s at 530°C to narrow the size distribution and further help the formation of large quantum dots. The resulting InAs islands have a diameter of about 20nm to 30nm and a height of about 7nm to 10nm.

The GaAs capping layer is grown at a temperature of 530°C . As pointed out by the authors it is important that the capping layer thickness (about 4nm) is thinner than the original height of the QDs. In addition, the overgrowth has to be followed by a growth interruption (annealing) of 30 to 60 seconds at the growth temperature. The authors didn't observe ring formation for thicker capping layers. A typical image of the resulting quantum rings is shown in Fig. 4.1(a). The central holes are located at the sites of the former dots [Lorke02] and typically have a radius of about 10nm. The outer radius of the ring changes between 30nm in $[110]$ direction and 70nm in $[\bar{1}\bar{1}0]$. The elongation in $[\bar{1}\bar{1}0]$ direction is explained by the preferred In diffusion in this direction [Horikoshi90]. The rim of the QRs has typically a height of about 2nm. In case the sample is removed without annealing after the capping layer deposition not all islands have a well-defined depression in their centre. The authors assume that in this case there is not enough time for the complete transformation into rings.

In order to use the quantum rings for electronic or optical applications they have to be overgrown by a further thick GaAs cladding layer. This layer is grown at the same temperature (530°C). Spectroscopic data [Lorke02] prove that the ring shape of the self-organised QRs can thereby be preserved.

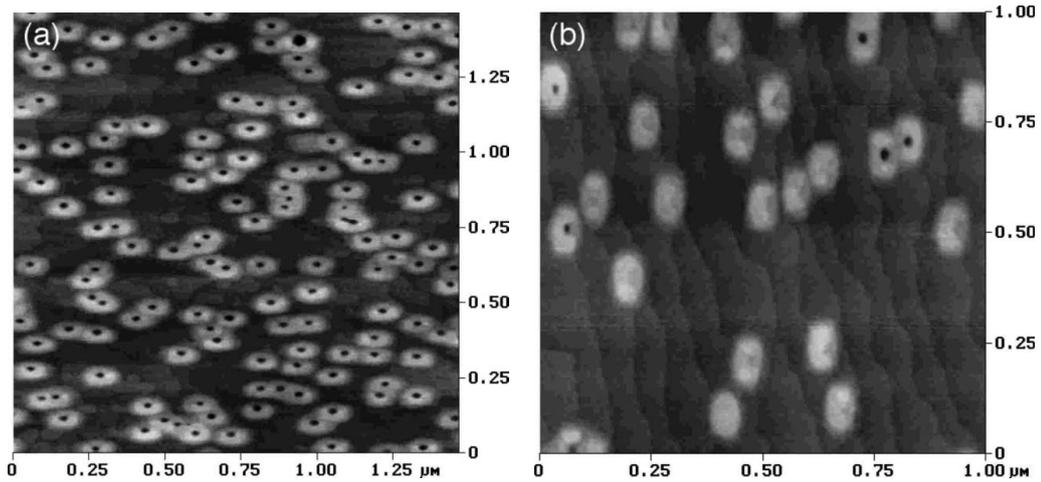


Figure 4.1: Atomic force micrographs of self-organised InGaAs rings taken from [Lorke02]. According to the authors the islands are elongated in $[1\bar{1}0]$ direction. Fig. (a) shows the surface morphology after 60s annealing at the growth temperature. If the sample is removed immediately after the capping layer deposition [Fig. (b)] not all islands have a well-defined depression in their centre.

4.1.2 Growth mechanisms

During the overgrowth the heteroepitaxial system is not in thermal equilibrium, since the structure changes its morphology with time. Two growth models have been proposed by Lorke et al. The first is based on *kinetic considerations*. The transformation from dots to rings is explained by a diffusion mechanism [Lorke01, Lorke02]. The second model is based on *thermodynamic considerations* introducing an analogy of the InAs islands to wetting droplets on solid substrates. In this model the transition from dots to rings is caused by a change of the surface free-energy balance at the three-phase contact-line between GaAs, InAs, and vacuum [Blossey02, Lorke03].

Diffusion driven model

Diffusion plays an important role during the overgrowth of quantum dots as a significant material redistribution during the capping of InAs islands is observed [Xie94, Joyce01a].

The model by Lorke et al. explaining the process of ring formation is summarised in Fig. 4.2 [Lorke01, Lorke02]. The GaAs capping layer is surrounding the dot rather than covering it like a blanket [see Fig. 4.2(a)]. This assumption is justified by the fact that the relaxed InAs lattice constant at the top of the dot makes it an unfavourable site for the attachment of Ga atoms. In addition, the ring formation takes place only if the InAs islands are *partially* capped. Then, InAs which remains uncovered at the top of the island can diffuse outwards leaving a hole at the location of the InAs island [see Fig. 4.2(b)]. This process is facilitated by the fact that In atoms are very mobile at the annealing temperature of 530°C unlike Ga atoms [Lorke02]. Therefore, the outward diffusion of In is stopped by alloying with the deposited capping material to InGaAs. This explains the rather sharp outer edge of the rings [Fig. 4.2(c)].

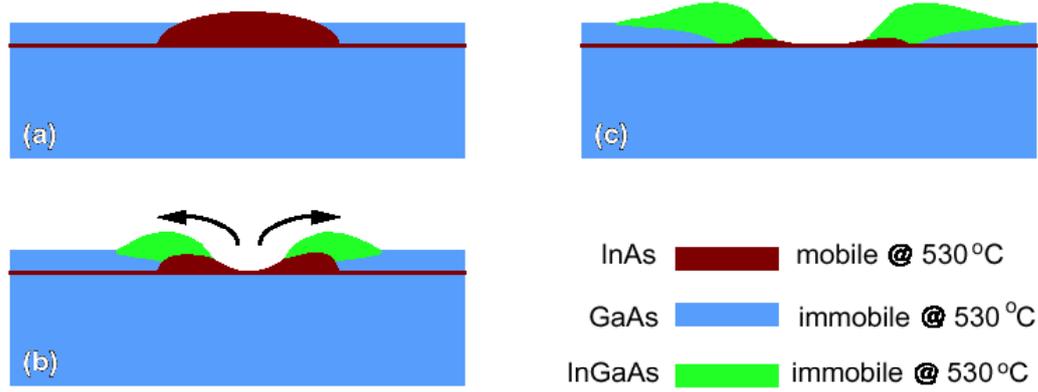


Figure 4.2: Scenario of a diffusion-driven transformation from dots to rings according to Lorke et al. [Lorke01].

A further indication that diffusion plays an important role is deduced from the elongated shape of the rings in $[1\bar{1}0]$ direction (see Fig. 4.1). The anisotropy of the (001) surface is caused by the As-rich (2x4) surface reconstruction which is usually observed during MBE growth [Hashizume95, LaBella99]. In order to minimise the number of dangling bonds at the surface two adjacent As atoms form a dimer along the $[1\bar{1}0]$ direction. This results in a greater adatom surface diffusion along $[1\bar{1}0]$ as compared to the $[110]$ direction [Brault98, Sudijono92]. Furthermore, it is to note that the ring formation process is strongly temperature dependent [Joyce98].

Wetting droplet instability

An alternative explanation [Blossey02, Lorke03] for the rather abrupt morphological change of the InAs islands into ring structures comes from an analogy to the instability of wetting droplets. A similar *de-wetting process* was used by Herminghaus et al. [Herminghaus98] to explain the formation of polystyrene rings on Si.

The model is sketched in Fig. 4.3. In the case of a wetting droplet the three phases shown in the image correspond to $1 \cong \text{solid phase}$, $2 \cong \text{liquid phase}$, and $3 \cong \text{vapour}$. The shape of the droplet is governed by the surface free-energies. At the three-phase contact-line between solid phase, liquid phase, and vapour three interfacial tensions (or surface-free energies) are acting at the droplet border [see Fig. 4.3 (a)]. They are denoted by γ_{12} , γ_{23} , and γ_{13} . In equilibrium the surface forces balance is described by *Young's equation*

$$\gamma_{13} = \gamma_{23} \cos \theta + \gamma_{12} \quad (4.1)$$

θ is the contact angle between the forces pulling along the “12” (solid-liquid) and “23” (liquid-vapour) interfaces.

Adding a new layer of solid phase shifts the interface between the solid phase and vapour [see Fig. 4.3(b)]. The three-phase contact line is lifted up and the surface force balance is now

$$\gamma_{13} + \gamma_{12} \cos \theta = \gamma_{23} \cos \theta \quad (4.2)$$

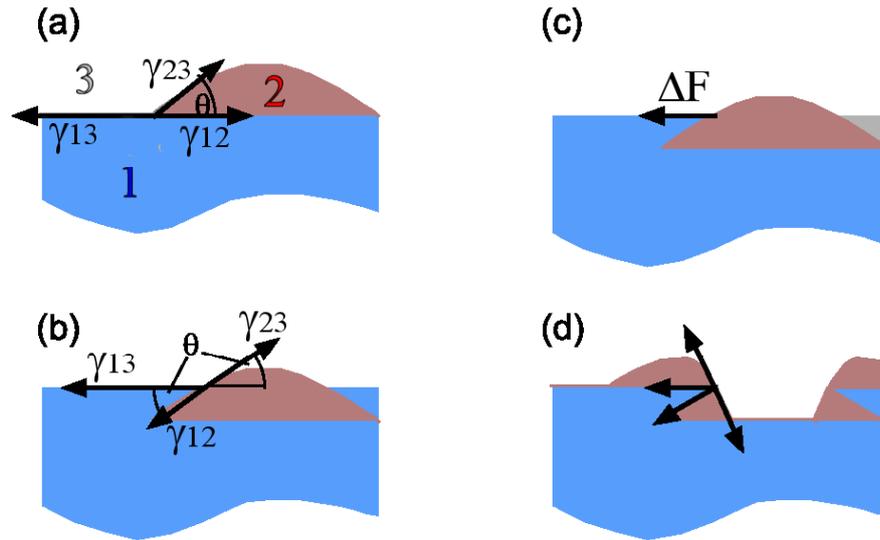


Figure 4.3: Model of ring formation promoted by a wetting droplet instability according to Blossey et al. [Blossey02]. For a wetting droplet: 1 \cong solid phase, 2 \cong liquid phase, 3 \cong vapour. For the quantum dot model: 1 \cong GaAs substrate, 2 \cong InAs dot, 3 \cong vacuum (As vapour). The vectors show the corresponding interfacial tensions γ_{12} , γ_{23} , γ_{13} , and the Young force ΔF . See text for more details.

The resulting imbalance yields an uncompensated *Young force* which is pulling radially outward [see Fig. 4.3(c)]

$$\Delta F = \gamma_{12}(1 + \cos \theta) \quad (4.3)$$

A possible new equilibrium shape is shown in Fig. 4.3(d).

This model has been transferred to the system of an InAs island on a GaAs substrate. In this case the three phases correspond to 1 \cong GaAs, 2 \cong InAs, and 3 \cong vacuum (or As vapour). A small difference in surface tension, causing a large change in contact angle, can be sufficient to destroy the surface force balance between the GaAs/InAs/vapour interfaces and results in the formation of a ringlike rim of InAs as a new equilibrium shape.

Qualitatively this scenario provides an explanation for the observed shape transformation from QDs to QRs. However, there are a few aspects which are not taken into account, according to the authors: the influence of a thin InAs wetting layer, elastic effects (strain), or edge effects (anisotropic diffusion) are not considered. Kinetic effects, like alloying and diffusion of the constituents, might play an important role as well. However, none of these effects should in principle alter the morphological instability deduced from the droplet model.

Complementary investigations by other authors

The formation of ring structures during overgrowth of InAs islands with GaAs has been reported by other authors as well.

Granados et al. [Granados03a, Granados03b] show the strong dependence of the final morphology on the particular growth conditions, like the substrate temperature and the molecular species of the As flux (As_2 or As_4). Drastic differences are observed for the same amount of deposited material. Fig. 4.4(a) shows a atomic force micrograph of the uncovered InAs islands. They have an average height of 10nm. No ring formation has been observed for the capping of smaller islands. Overgrowth under As_4 flux with 2nm GaAs at 540°C and 60s annealing at the growth temperature leads to the formation of elongated nanostructures [see Fig. 4.4(b)]. Reducing the growth temperature to 500°C results in a camel hump-like form [see Fig. 4.4(c)]. However, 2nm GaAs overgrowth at 500°C using As_2 and annealing for one minute induces ring like structures.

The experimental results are explained by the competition between diffusion and de-wetting processes, as described by Lorke et al.

At 540°C the higher mobility of In especially in $[1\bar{1}0]$ direction and the strong In-Ga alloying, resulting in the formation of immobile InGaAs, leads to elongated nanostructures [see Fig. 4.4(b)].

For $T_{\text{cap}} = 500^\circ\text{C}$ the migration of Ga atoms into the central region is reduced. Therefore, InGaAs alloying takes place mainly on the outside edge of the QD. De-wetting of the liquid central InAs region results in the formation of a depleted region causing a camel hump-like shape [see Fig. 4.4(c)].

Under As_4 flux, the migration of group III atoms is increased in $[1\bar{1}0]$ direction (asymmetrically elongated nanostructures), whereas As_2 has an enhanced reactivity, resulting in the formation of quantum rings as shown in Fig. 4.4(d).

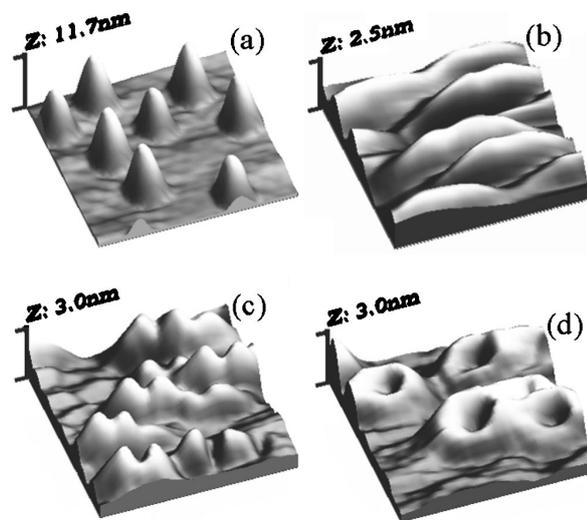


Figure 4.4: 250nm x 250nm AFM images of InAs quantum dots: (a) free-standing, (b) capped with 2nm GaAs at 540°C , (c) capped with 2nm GaAs at 500°C , (d) like (c) but covered under As_2 atmosphere (taken from [Granados03a]).

Several other authors report on ring formation even *without applying a special growth interruption* [Kamiya99, Ferdos02, Heidemeyer02, Songmuang03, Takehana03]. After the overgrowth the samples are immediately cooled down to room temperature. Of course, this cooling process takes some time (about 1.5min, assuming a cooling rate of $5^\circ\text{C}/\text{s}$). On the other hand, ring formation occurs with a clearly lower thermal budget than in the case of annealing one minute at 530°C before starting the cooling process.

Lee et al. [Lee98] have observed ring formation during partial overgrowth of $\text{In}_{0.5}\text{Ga}_{0.5}\text{As}$ quantum dots by metalorganic vapour-phase epitaxy (MOVPE). Quantum rings occur after overgrowth with 6nm GaAs at 480°C without further annealing. However, reducing the overgrowth temperature only 30°C to 450°C (5nm capping) makes an annealing of 1min at 630°C necessary to produce ring structures.

Recently Raz et al. [Raz03] succeeded in growing InAs self-assembled quantum rings on InP. Similar trends as compared to the InAs/GaAs material system are observed: the rings are elon-

gated along the $[1\bar{1}0]$ direction, and the long diameter of the QRs exceeds about three times the diameter of the uncapped QDs. The average height of the original QDs is reduced by a factor of about 7 during the dot-to-ring transformation.

On the other hand, the formation of InAs/InP quantum rings disagrees with the kinetic model by Lorke et al. which assumes that the driving force for the dot to ring transformation is the difference in the surface diffusion velocity of In and Ga atoms, as dot material and substrate/capping layer contain the same group III material. Therefore, Raz et al. believe that the thermodynamic model provides a better explanation for the formation of the rings.

Until recently only in III-V system semiconductors QR structures have been observed. Very recently Cui et al. [Cui03] produced SiGe quantum rings by partially overgrowing large (dome shaped) Ge islands with a thin Si layer at a relative high temperature of 680°C. The driving force for the ring formation is attributed to the strain energy relief after capping together with the high Ge surface diffusion and Ge surface segregation.

4.1.3 Investigated samples

The samples investigated have been provided by the group of P.M. Petroff in Santa Barbara, USA.

All structures have been grown on GaAs (001) wafers. For all growth steps dimeric As (As_2) from cracked As_4 has been used. This means that the molecular species of the As flux was As_2 with some rest of As_4 . The growth rate for GaAs growth was $2.53\text{\AA}/s$. InAs was grown at a rather low rate of $0.055\text{ML}/s$.

First a 100nm GaAs buffer layer, followed by a superlattice and another GaAs buffer layer of 100nm thickness was grown at a temperature of 610°C. In the following four different samples were prepared with slightly different growth parameters, which are summarised in table 4.1.

Sample	QD growth	GaAs coverage	Temperature of coverage
c10-530	$(550 \pm 5)^\circ\text{C}$	10nm	$(530 \pm 5)^\circ\text{C}$
c10-450	$(490 \pm 5)^\circ\text{C}$	10nm	$(450 \pm 5)^\circ\text{C}$
c03-530	$(550 \pm 5)^\circ\text{C}$	3nm	$(530 \pm 5)^\circ\text{C}$
c03-450	$(490 \pm 5)^\circ\text{C}$	3nm	$(450 \pm 5)^\circ\text{C}$

Table 4.1: Important growth parameters of the investigated InAs quantum dot samples. Only sample c03-450 shows quantum rings and was investigated by x-ray techniques in more detail.

The InAs quantum dots were grown at a temperature of 550°C and 490°C, respectively, as indicated in table 4.1. The InAs deposition was followed by 30s annealing at the growth temperature to narrow the size distribution and further help the formation of large quantum dots. Subsequently the samples were overgrown with GaAs at a growth rate of $2.53\text{\AA}/s$. The temperature was varied between 450°C and 530°C. The capping layer thickness changed between 3nm and 10nm. After the GaAs overgrowth the samples were immediately cooled down to room temperature.

4.2 Experiment

Atomic force micrographs have been recorded from all sample surfaces to characterise the surface morphology. The more time consuming investigation by x-ray techniques has only been applied to sample c03-450 (see Fig. 4.8) as on its surface all partially capped InAs quantum dots have evolved into circular InGaAs ring structures.

4.2.1 Atomic Force Microscopy

The four samples listed in table 4.1 have been investigated using a *Digital Instruments Nanoscope Dimension 3100* atomic force microscope, operated in Tapping Mode. Ex-situ AFM images have been taken at several positions on the sample surface. In Figs. 4.5 to 4.8 two images per sample are shown. One image has a side length of $1\mu\text{m} \times 1\mu\text{m}$, the other one a side length of $500\text{nm} \times 500\text{nm}$. Unfortunately, no sample without capping layer was available. Therefore, the size of the uncapped InAs quantum dots are not known.

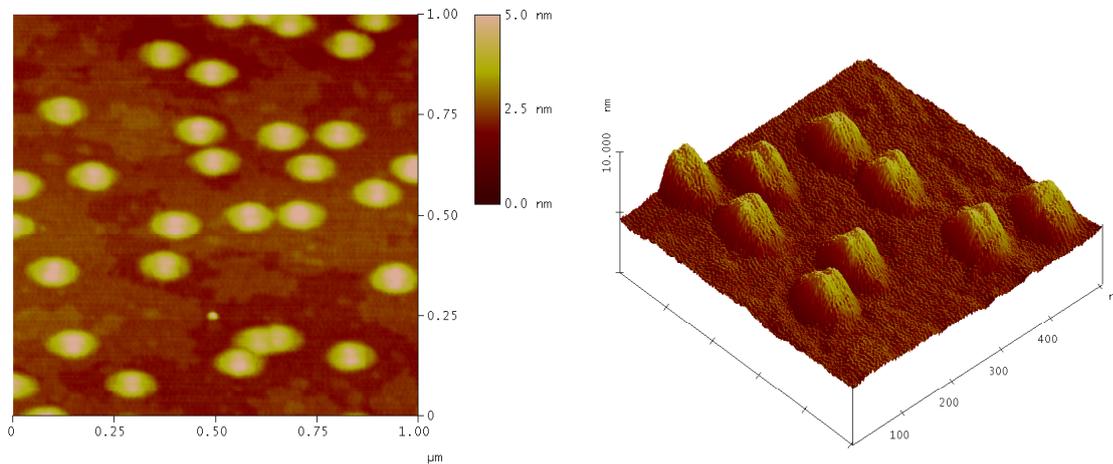


Figure 4.5: AFM images of sample c10-530. Due to the thickness of the GaAs capping layer (slightly larger than the height of the original dots) the InAs quantum dots evolve into a double peak structure.

Fig. 4.5 shows the surface morphology of sample c10-530 after overgrowth with 10nm GaAs at a temperature of 530°C . The thickness of the GaAs capping layer is expected to be slightly larger than the height of the original InAs quantum dots. In this case the InAs quantum dots evolve into a double peak structure with a preferential orientation along one of the $\langle 110 \rangle$ directions. The height of the dots is about 2.8nm, the base diameter is about 95nm to 105nm.

Fig. 4.6 shows the AFM images of sample c10-450 which was overgrown at the lower temperature of 450°C . Compared to the overgrowth at higher temperature (see Fig. 4.5), the double peak structure is more pronounced. Again the average height of the structures is 2.8nm, the base diameter is about 80nm.

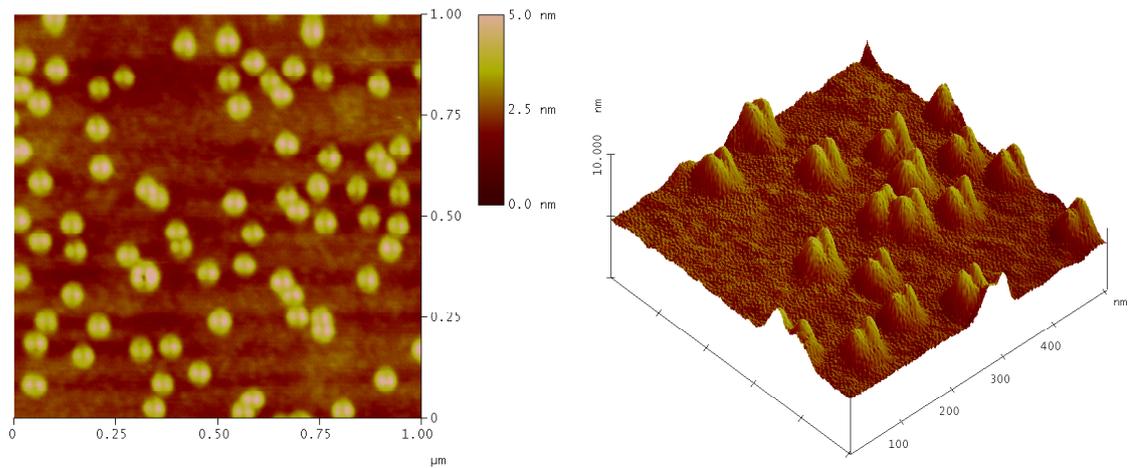


Figure 4.6: AFM images of sample c10-450. The thickness of the GaAs capping layer exceeds the height of the original InAs dots. Compared to the overgrowth at higher temperature (see Fig. 4.5) the double peak structure is more pronounced.

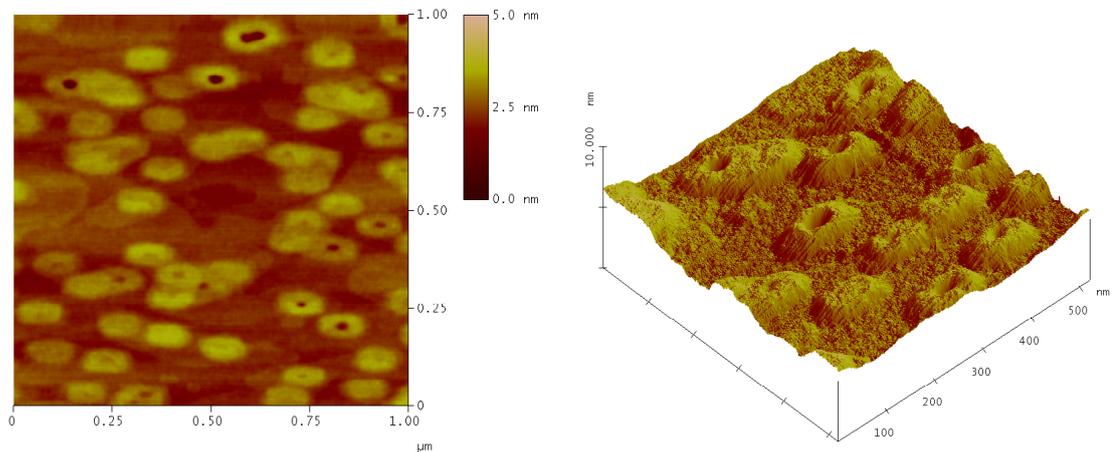


Figure 4.7: AFM images of sample c03-530. The original InAs quantum dots are only partially covered by the GaAs capping layer. A few dots have evolved into elongated quantum rings.

Fig. 4.7 shows two micrographs of sample c03-530, which was overgrown with only 3nm GaAs at a temperature of 530°C. In this case the original InAs quantum dots are only partially covered by the GaAs capping layer. Most of the islands have an elongated shape with a base diameter of 125nm to 150nm and 65nm to 75nm along the two $\langle 110 \rangle$ directions, respectively. Their height is about 1.4nm. Only a few dots have evolved into elongated quantum rings. The base diameter and the height of these rings are comparable to the other structures without central hole. The diameter of the hole is about 25nm to 30nm, its depth is up to 2.4nm.

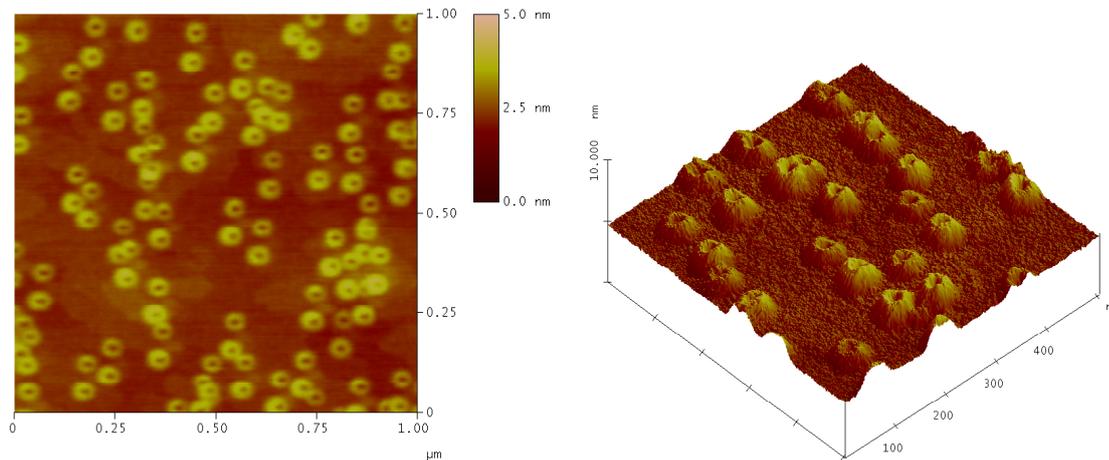


Figure 4.8: AFM images of sample c03-450. All the partially capped InAs quantum dots have evolved into circular InGaAs ring structures.

Sample c03-450 (see Fig. 4.8) was overgrown at a lower temperature of 450°C with 3nm GaAs. Again the original InAs quantum dots are only partially covered by the GaAs capping layer. At this growth temperature all the original InAs quantum dots have evolved into circular ring structures. The base diameter of the rings is about 55nm to 60nm in both $\langle 110 \rangle$ directions. The average height as well as the depth of the central hole is about 1.5nm.

These findings are comparable to the results from literature reviewed in chapter 4.1. It is assumed that the low growth rate for the InAs deposition together with the annealing of the quantum dot structures resulted in large InAs islands (base diameter of 20nm to 30nm, height of 7nm to 10nm as in most publications cited in this thesis). It is generally agreed that the presence of such islands is a prerequisite for the formation of quantum rings. In addition, no ring formation is observed for a capping layer thickness comparable or even exceeding the height of the original InAs quantum dots. Double peak structures as observed in Figs. 4.5 and 4.6 have been reported by Joyce et al. [Joyce01b] and Heidemeyer et al. [Heidemeyer02] for thick capping layers. On the other hand, camel hump-like structures [see Fig. 4.4(c)] have been observed by Granados et al. [Granados03a] for thin capping layers depending on other growth conditions, as well. This makes clear that the overgrowth process of quantum dots is very complex. Due to the fact that the heteroepitaxial system is not in equilibrium during overgrowth the final shape of the structures depends on many parameters.

Fig. 4.7 (sample c03-530) can be directly compared to Fig. 4.1(b). The nominal growth parameters correspond very well to the conditions described in [Lorke02]: large InAs quantum dots were overgrown at a temperature of 530°C and the sample was removed from the growth

chamber immediately after the capping. The size of the resulting islands and ring structures is comparable as well. The process of ring formation can be explained by the growth modes compared in section 4.1.2. The partial transformation into quantum rings is attributed to the fact that the samples were not annealed after the deposition of the GaAs capping layer. Therefore, there was not enough time for the complete transformation into rings which presumably takes place at the growth temperature of above 500°C. The lower temperatures during the cooling process are obviously not sufficient.

Therefore, it is even more surprising that at lower growth temperature (490°C for the dot growth, 450°C for the capping) ring formation is observed (see Fig. 4.8) for the same thickness of overgrowth and without further annealing (growth interruption). In addition, the QRs are not elongated in any direction. The evaluation of the GISAXS data (see the following section) confirms the circular shape of the islands with high statistical accuracy. The circular shape might be attributed to the reduced growth temperature of 450°C where the effect of the preferred diffusion of In in $[1\bar{1}0]$ direction [Horikoshi90] is less important. In addition, the molecular species of the As flux was dimeric As (As_2) for all samples. This As_2 has an enhanced reactivity which reduces the migration of group III atoms (In,Ga) in $[1\bar{1}0]$ direction.

For a better understanding of the transformation of *all* islands into ring structures a more detailed study with systematically varied growth parameters would be necessary.

Since all QDs have been transformed into QRs and due to the homogeneous size distribution of the rings, the last sample c03-450 was chosen for the investigation of shape, strain, and interdiffusion in the QRs by x-ray techniques under grazing incidence and exit angles.

4.2.2 Grazing incidence small angle scattering (GISAXS)

This section describes the x-ray measurements which have been performed for the characterisation of sample c03-450. This sample shows only ring-shaped islands (see Fig. 4.8). The x-ray techniques have already been introduced in more detail in chapter 2.2. Grazing incidence small angle x-ray scattering (GISAXS) is used to investigate shape and symmetry of the QRs. This technique is not sensitive to the crystalline structure of the sample. Grazing incidence diffraction (GID) can additionally quantify the strain and the composition within the nanostructures.

The grazing incidence small angle x-ray scattering (GISAXS) measurements have been performed at the Beamline ID1 at an energy of 8.0keV. A first experiment was performed using the linear position sensitive detector (PSD). The detector was mounted on the detector arm of the diffractometer, oriented parallel to the sample surface as sketched in Fig. 2.17. In the centre a lead beam stop attenuated the strong specular reflected beam. A second experiment was performed using the two-dimensional CCD camera. The CCD detector was mounted on a movable stage in the evacuated SAXS tube. The corresponding set-up is shown in Fig. 2.10. Again a linear lead beam stop was used to shadow the specular reflected beam.

Fig. 4.9 shows a typical GISAXS measurement taken with the CCD camera at an incident angle $\alpha_i = 0.4^\circ$. In the centre a linear beam stop shadows the specular reflected beam at $\alpha_f = 0.4^\circ$. Clearly the enhanced scattering intensity close to the critical angle $\alpha_c = 0.30^\circ$ can be observed (*Yoneda maximum*).

As we are not interested in the exit angle α_f resolved data, in the following only cuts or PSD data along 2θ for an exit angle of $\alpha_f = 0.32^\circ$ are considered.

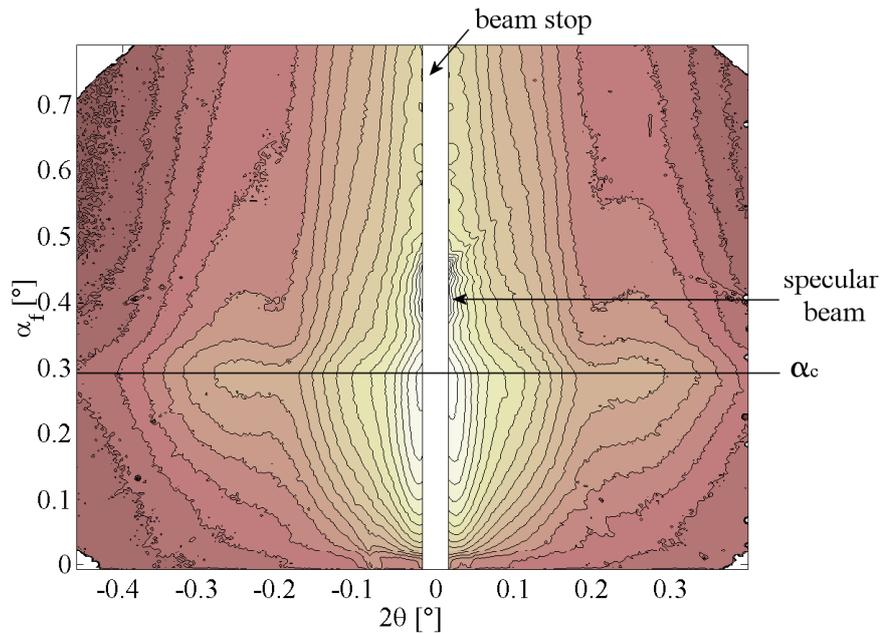


Figure 4.9: GISAXS measurement of the sample c03-450. The α_f - 2θ measurement was taken with the two-dimensional CCD detector. The incidence angle α_i was set to 0.4° .

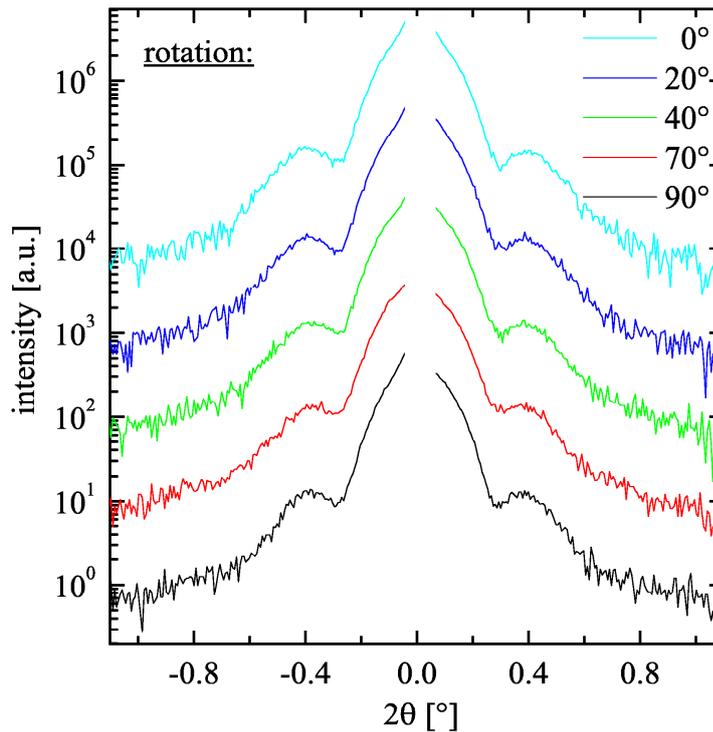


Figure 4.10: The figure shows cuts along 2θ for different azimuthal positions as indicated (sample: c03-450, $\alpha_i = 0.4^\circ$, $\alpha_f = 0.32^\circ$). No azimuthal dependence on the sample rotation is observed, indicating that the lateral quantum ring shape is isotropic. The measured curves are shifted for clarity.

Fig. 4.10 shows five measurements for different azimuthal positions of the sample in a range between 0° and 90° . The curves plotted in Fig. 4.10 are shifted in intensity for more clarity. In the measurement no azimuthal dependence is observed indicating that the lateral quantum ring shape is isotropic. This confirms the observation already made by atomic force microscopy (see Fig. 4.8).

Data evaluation

An introduction to the evaluation of GISAXS data as well as a computer program for the simulation of GISAXS data has been published by R. Lazzari [Lazzari02].

Generally in small-angle scattering of particles, the differential scattering cross section $\frac{d\sigma}{d\Omega}(\vec{q})$ is written as the product of the square of a *form factor* $F(\vec{q})$ of a single object and a *correlation function* $C(\vec{q})$ of the object positions.

$$\frac{d\sigma}{d\Omega}(\vec{q}) \propto \langle |F(\vec{q})|^2 \rangle_\alpha \cdot C(\vec{q}) \quad (4.4)$$

$\langle \dots \rangle_\alpha$ designates averaging over the size-shape distribution.

The form factor $F(\vec{q})$ in Born approximation is the Fourier transform of the shape function S of the object.

$$F(\vec{q}) = \int_S \exp(i\vec{q}\vec{r}) d\vec{r} \quad (4.5)$$

The main problem in the interpretation of the scattering data is how the contributions of the correlation function can be distinguished from the structure factor induced scattering.

On the surface of sample c03-450 lateral correlations do not play a significant role. Therefore, the data were analysed by taking only a form factor into account. For data fitting a routine was developed using MATLAB.

Inspired from the AFM it seems reasonable to use a model based on disc-shaped rings. The form factor of a disc with radius R_{out} and a hole in the centre of radius R_{in} is calculated in polar coordinates:

$$\begin{aligned} F(q) &= \int_{R_{\text{in}}}^{R_{\text{out}}} \int_0^{2\pi} 1 \cdot \exp(iqr \cos \phi) r d\phi dr = \int_{R_{\text{in}}}^{R_{\text{out}}} 2\pi r J_0(qr) dr = \\ &= \frac{2\pi R_{\text{out}} J_1(qR_{\text{out}}) - 2\pi R_{\text{in}} J_1(qR_{\text{in}})}{q} \end{aligned} \quad (4.6)$$

using the recursion formula for Bessel functions:

$$\frac{d}{dx} [x^n J_n(x)] = x^n J_{n-1}(x) \quad (4.7)$$

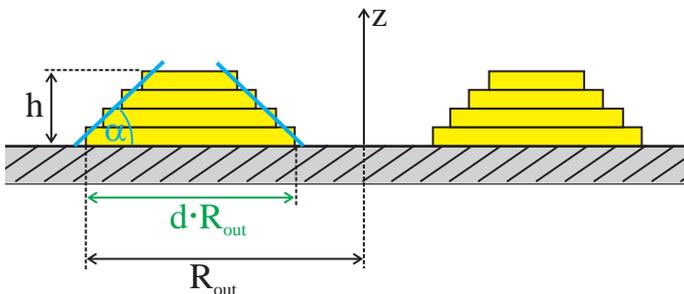


Figure 4.11: Model used for the simulation of the GISAXS measurements shown in Fig. 4.10. See text for more details.

Fig. 4.11 shows a cut through the centre of the used ring model. Several rings with decreasing width are stacked on top of each other. The decrease of the outer and the increase of the inner radius as a function of height h is expressed by the angle α . In addition, a size distribution of this structure is taken into account separately. Fit parameters for the calculated model are the outer radius R_{out} , the thickness of ring at the base $d \cdot R_{\text{out}}$, the height h , the angle α , and a parameter for the size distribution σ (half width of a gaussian distribution around the average radius R_{out}). Based on these parameters and the form factor of a ring as determined in Eq. 4.6 the scattering amplitude has been calculated as follows:

$$A(q) \propto \int_{R_{\text{out}}-2\sigma}^{R_{\text{out}}+2\sigma} \left[\int_0^h F(q, R, z) dz \cdot \exp\left(\frac{-(R_{\text{out}} - R)^2}{2\sigma^2}\right) \right] dR \quad (4.8)$$

using the form factor

$$F(q, R_{\text{out}}, z) = \frac{1}{q} \left\{ \left(R_{\text{out}} - \frac{z}{\tan \alpha} \right) J_1 \left[q \left(R_{\text{out}} - \frac{z}{\tan \alpha} \right) \right] - \left(R_{\text{out}}(1-d) - \frac{z}{\tan \alpha} \right) J_1 \left[q \left(R_{\text{out}}(1-d) - \frac{z}{\tan \alpha} \right) \right] \right\} \quad (4.9)$$

The best fit of this calculation is plotted in Fig. 4.12 as a red solid line. The parameters of the best fit are listed in table 4.2 showing good agreement with the AFM results. The lateral size of the quantum rings can be determined with high accuracy from the simulation of the width and the position of the shape-induced oscillations. The size distribution of the quantum ring ensemble σ around the average radius R_{out} results in a damping of these oscillations. The parameters h and α have a similar effect as they average over rings with changing thickness $d \cdot R_{\text{out}}$, but constant average radius $R_{\text{out}}(1 - d/2)$. As these effects are partly coupled a larger error margin has been attributed to the corresponding values.

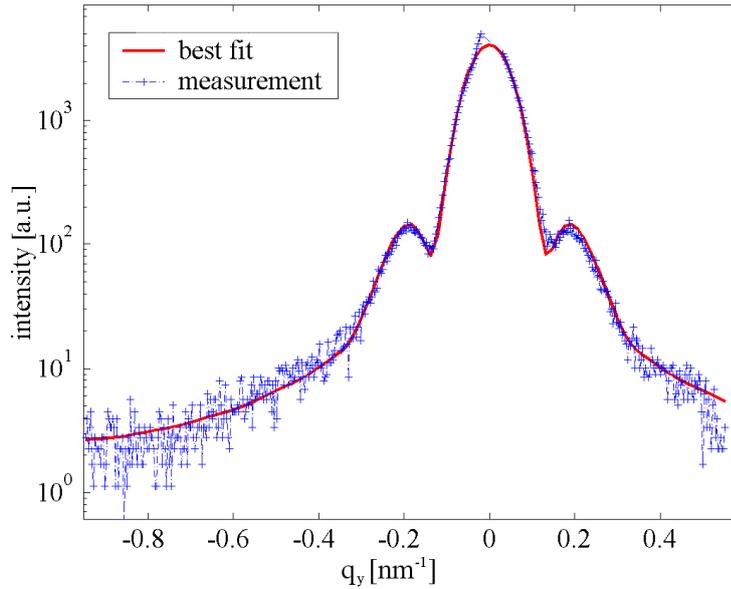


Figure 4.12: Best fit for the GISAXS measurements shown in Fig. 4.10 using the model described in Fig. 4.11 and Eqs. 4.8 and 4.9.

parameter	value
R_{out}	$(25.6 \pm 0.5)\text{nm}$
$d \cdot R_{\text{out}}$	$(0.79 \pm 0.02) \cdot R_{\text{out}}$
h	$(1.7 \pm 0.3)\text{nm}$
α	$(20 \pm 2)^\circ$
σ	5.2nm

Table 4.2: Parameters used for the best simulation of the GISAXS data (see Fig. 4.12).

4.2.3 Grazing incidence diffraction (GID)

Grazing incidence diffraction (GID) measurements of the sample c03-450 have been performed to gain information about strain and interdiffusion within the rings. All data have been measured at the Beamline ID1 at an energy of 10.3keV close to the $(\bar{2}20)$ and (220) surface Bragg reflection. The incident angle was set to $\alpha_i = 0.18^\circ$, slightly smaller than the critical angle for total external reflection $\alpha_c = 0.22^\circ$, to measure surface sensitive. Strain sensitive radial scans have been recorded for two sample orientations, rotated by 90° [i.e. $(\bar{2}20)$ and (220) reflection] along $[\bar{1}\bar{1}0]$ and $[110]$, respectively. The position sensitive detector PSD has been used to record α_f resolved data. The measured data are plotted in Figs. 4.14 to 4.17. In Figs. 4.14 and 4.16 the intensity integrated along the PSD is shown for the two investigated sample orientations. α_f resolved measurements are shown in corresponding $q_{\text{rad}} - q_z$ mappings in Figs. 4.15 and 4.17.

At the radial positions marked from 1 to 12 in Figs. 4.14 and 4.16 angular scans have been performed. Since the length of the scattering vector Q does not change these scans are not sensitive to the lattice strain, but only to the form factor. For these measurements only the integrated intensity was recorded and is shown in Figs. 4.18 and 4.19 or as $q_{\text{rad}} - q_{\text{ang}}$ mappings in Figs. 4.20 and 4.21 on a logarithmic intensity scale. The light blue lines mark the radial position where the angular scans have been recorded. The points in between are interpolated.

From the following evaluation of the measured data it becomes clear that the ‘‘iso-strain scattering model’’ (ISS) [Kegel01] cannot be applied to the quantum ring samples. This can be understood from the evaluation of the angular measurements. In the iso-strain scattering model each radial position corresponds to a certain scattering volume with a particular strain state, i.e. lattice parameter. The corresponding angular scan gives information about the shape of this iso-lattice-parameter volume. Therefore, each angular scan can be fitted with the shape function of such an area (disc or ring) similar to the fit of the GISAXS measurements. In the present case however, the angular scans number 2 and 3 measured at $q_{\text{rad}} = -0.044\text{\AA}^{-1}$ and $q_{\text{rad}} = -0.035\text{\AA}^{-1}$ do not show an absolute maximum in the centre (see Fig. 4.18). As the form function of a disc or a ring always has the absolute maximum in its centre these data cannot be explained with a simple form factor fit. On the other hand, this result can easily be understood regarding the two-dimensional plot of the form factor of a ring (without size distribution) in Fig. 4.13. For certain values of q_{rad} an off-centre cut can show a minimum in angular direction under certain circumstances (see the black line in Fig. 4.13).

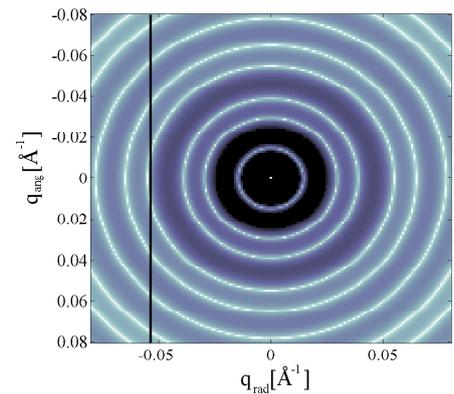


Figure 4.13: Two-dimensional plot of the form factor of a ring structure.

Figure 4.13: Two-dimensional plot of the form factor of a ring structure. The plot shows concentric rings of intensity in the $q_{\text{rad}} - q_{\text{ang}}$ plane. The x-axis is $q_{\text{rad}} [\text{\AA}^{-1}]$ ranging from -0.05 to 0.05, and the y-axis is $q_{\text{ang}} [\text{\AA}^{-1}]$ ranging from -0.08 to 0.08. A vertical black line is drawn at $q_{\text{rad}} \approx -0.044 \text{\AA}^{-1}$, showing a minimum in intensity at $q_{\text{ang}} = 0$.

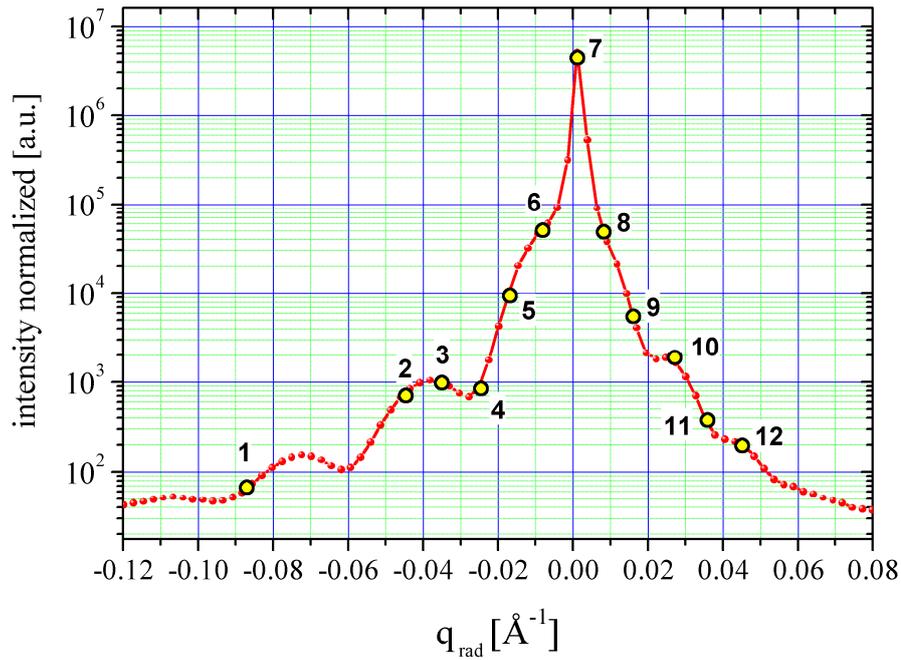


Figure 4.14: Radial measurement of the α_f integrated intensity at the $(2\bar{2}0)$ Bragg reflection. The number 1 to 12 mark the positions where angular scans have been recorded (see Fig. 4.18).

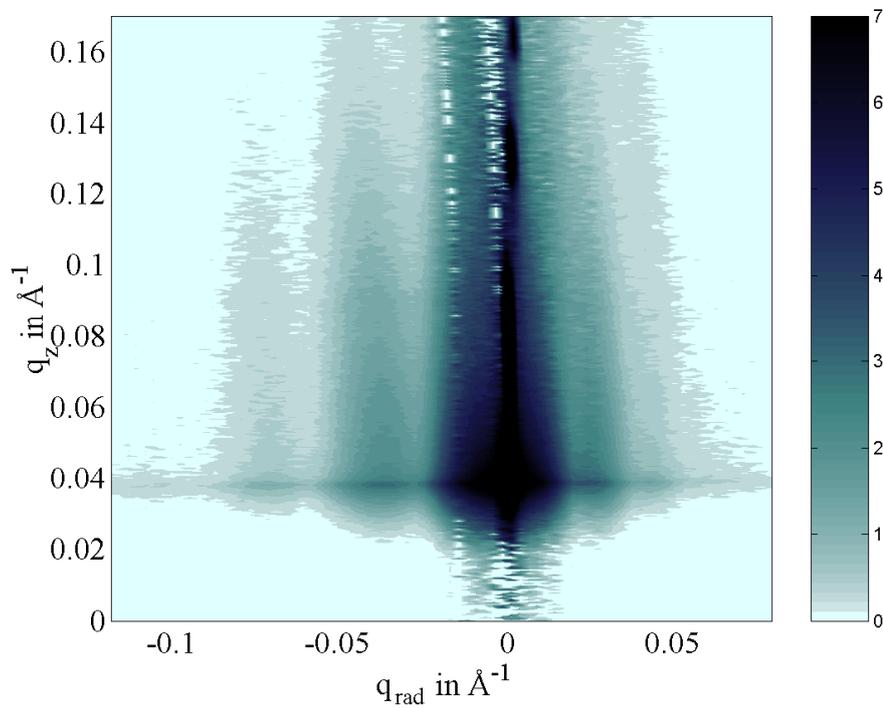


Figure 4.15: $q_{\text{rad}} - q_z$ mapping at the $(2\bar{2}0)$ Bragg reflection. The intensity is plotted in a logarithmic scale.

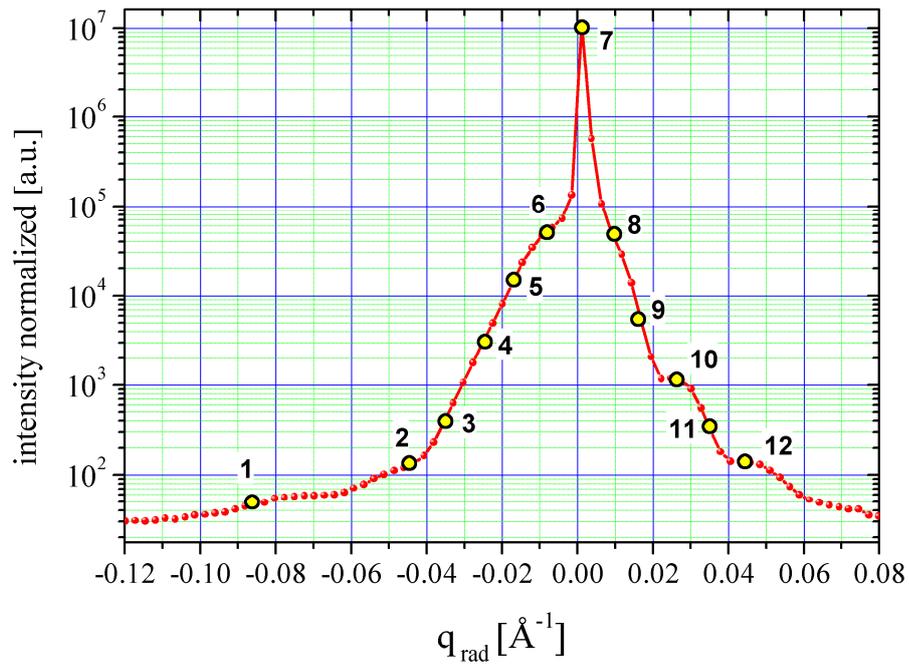


Figure 4.16: Radial measurement of the α_f integrated intensity at the (220) Bragg reflection. The number 1 to 12 mark the positions where angular scans have been recorded (see Fig. 4.19).

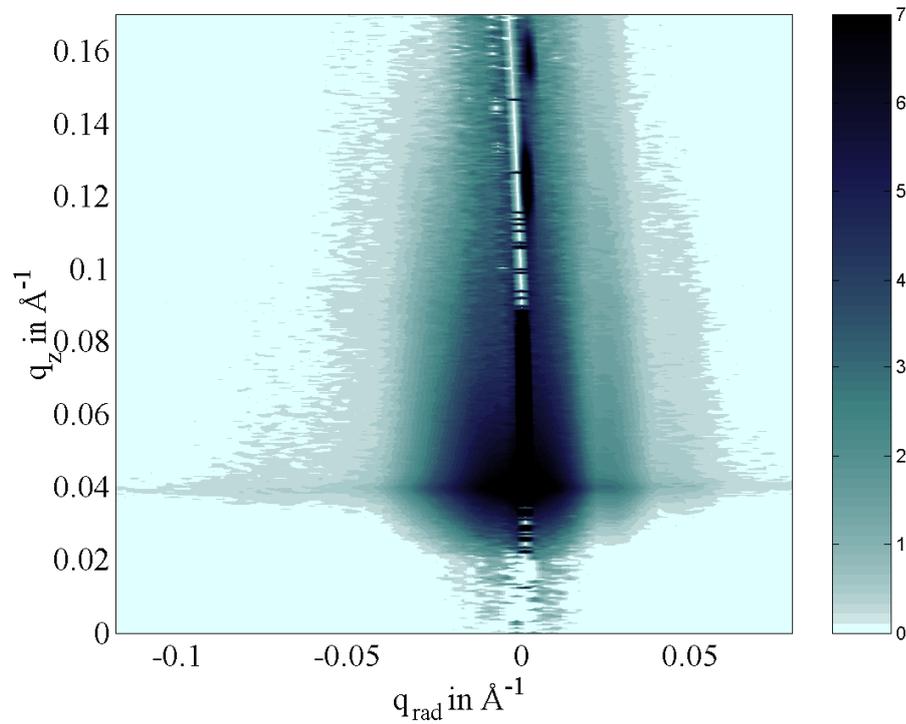


Figure 4.17: $q_{\text{rad}} - q_z$ mapping at the (220) Bragg reflection. The intensity is plotted in a logarithmic scale.

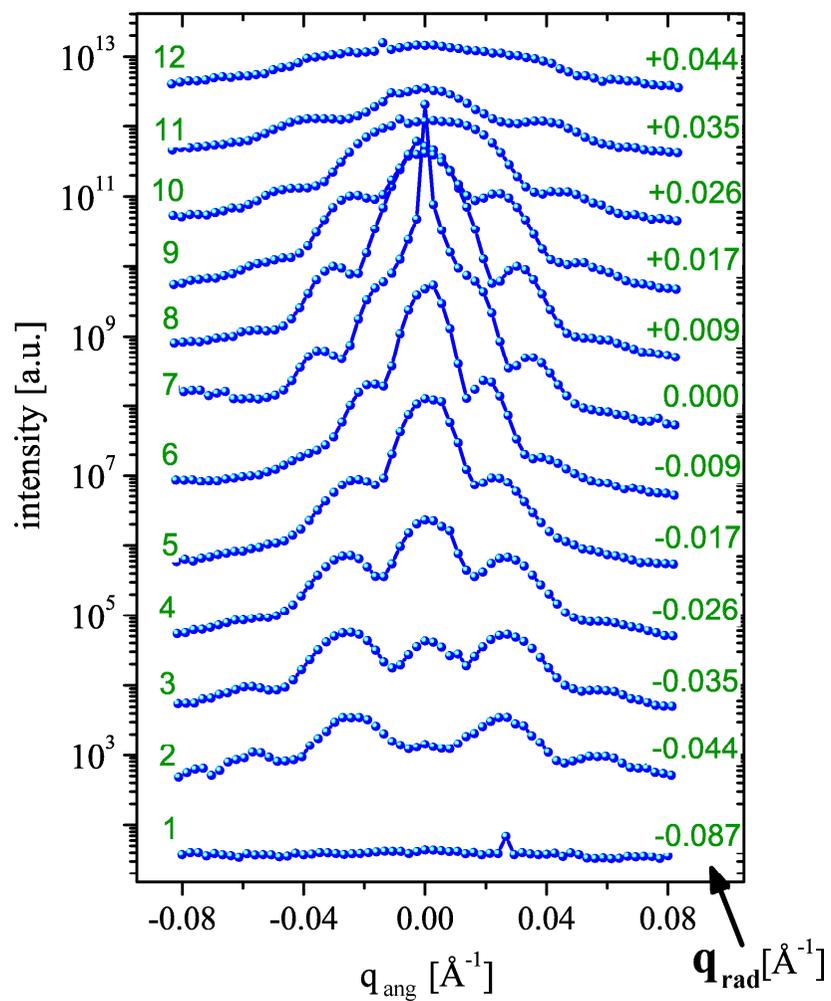


Figure 4.18: Angular measurement of the α_f integrated intensity at the (220) Bragg reflection. The angular measurements have been performed at the positions indicated in Fig. 4.14.

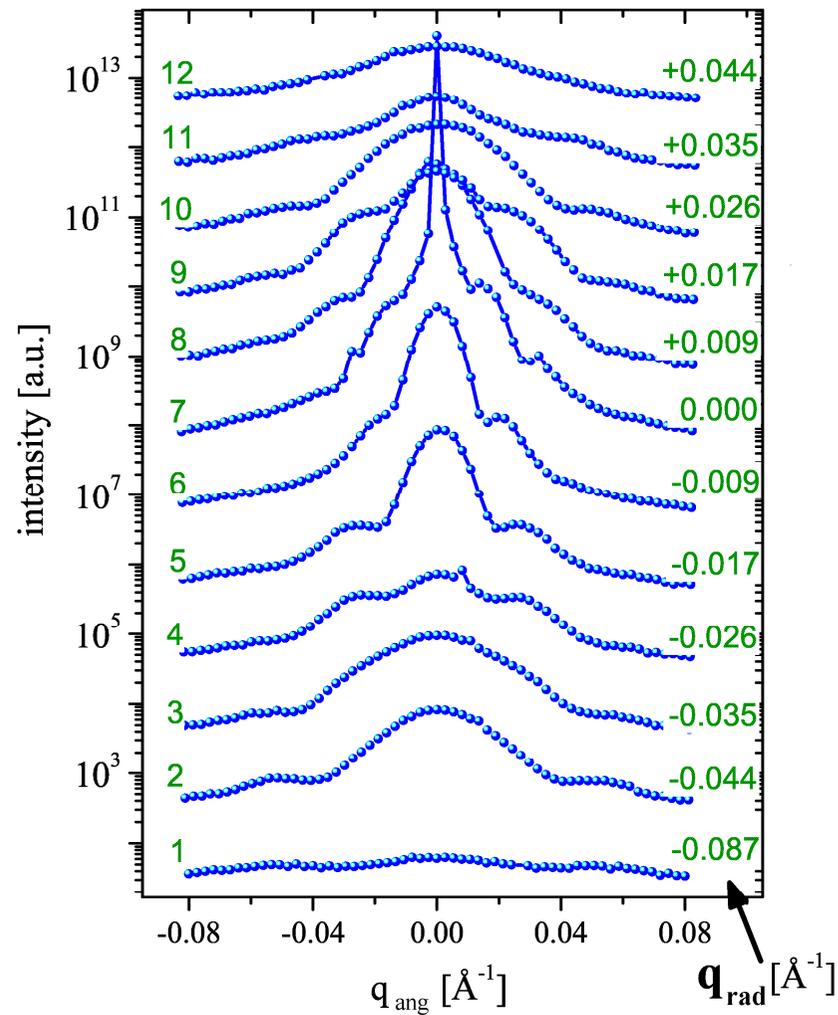


Figure 4.19: Angular measurement of the α_f integrated intensity at the (220) Bragg reflection. The angular measurements have been performed at the positions indicated in Fig. 4.16.

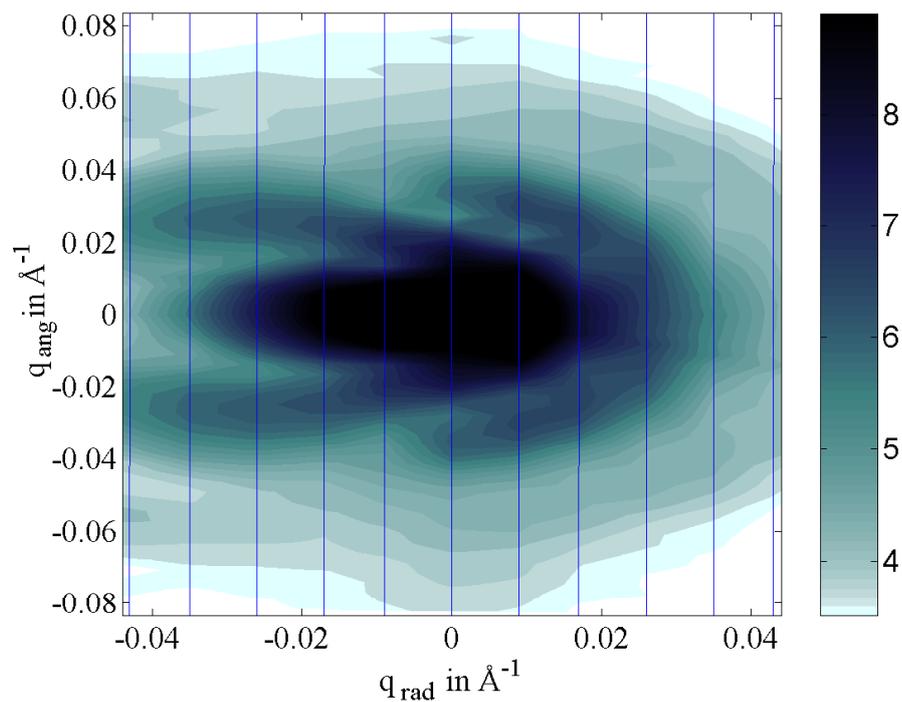


Figure 4.20: $q_{\text{rad}} - q_{\text{ang}}$ mapping of the α_f integrated intensity at the $(2\bar{2}0)$ Bragg reflection. The light blue lines mark the radial position where the angular scans have been recorded.

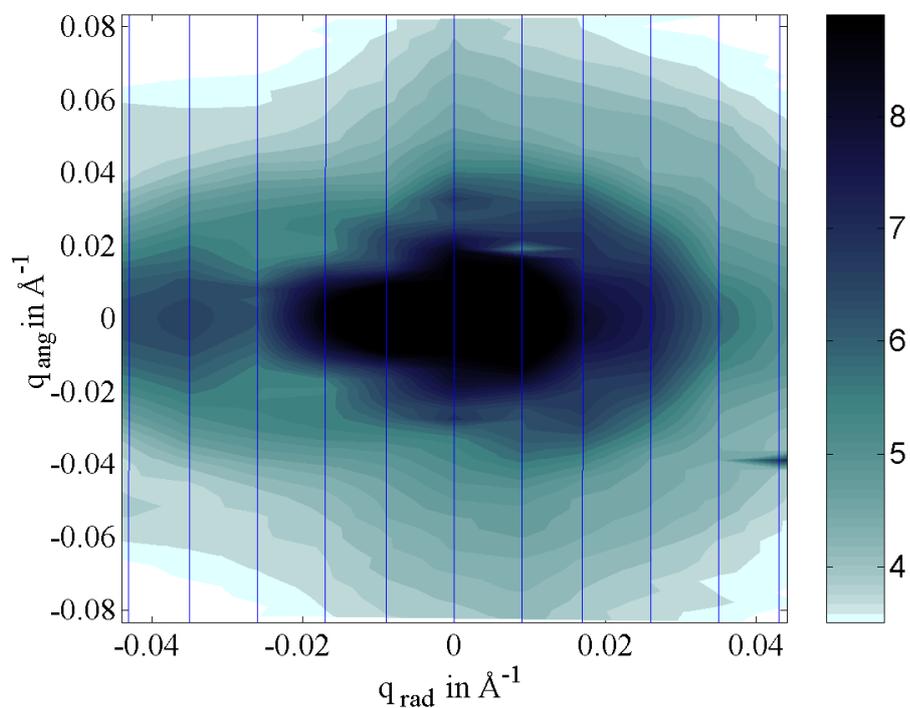


Figure 4.21: $q_{\text{rad}} - q_{\text{ang}}$ mapping of the α_f integrated intensity at the (220) Bragg reflection. The light blue lines mark the radial position where the angular scans have been recorded.

This is a first hint that the superposition of several shape factors (induced by different strain states) plays a role for the analysis of the measured angular data. In addition, the strain sensitive radial scan shows oscillations for $q_{\text{rad}} < 0\text{\AA}^{-1}$ originating from the shape of the quantum rings.

Therefore, the measured angular scans do not allow for a discrete analysis on the basis of the ISS model. Rather all scans have to be simulated all together in $q_{\text{rad}} - q_{\text{ang}}$ mappings as plotted in Figs. 4.20 and 4.21 and $q_{\text{rad}} - q_z$ mappings as shown in Figs. 4.15 and 4.17.

4.3 Finite-element simulation of the GID data

Due to the complex sample structure finite-element calculations have to be used for the evaluation of the GID data. In order to simulate the measured diffraction patterns, the displacement field u_x in a plane through the centre of the QR is needed. These displacements have been calculated using the commercial FEM program package PATRAN/NASTRAN. The FEM calculations have been performed in three-dimensions as described in chapter 2.3.3.

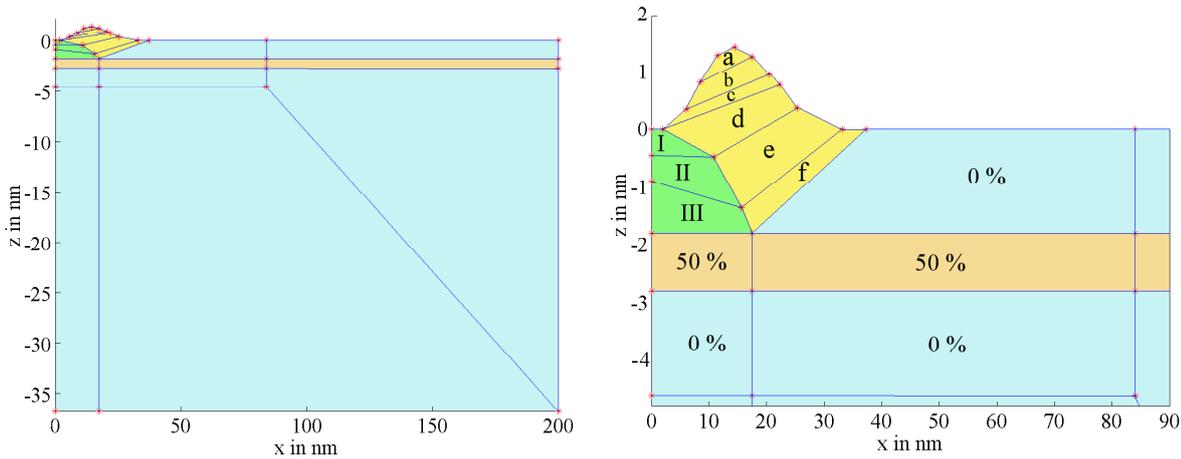


Figure 4.22: FEM model of the quantum ring structure. (left) The size of the simulated substrate is $200\text{nm} \times 37\text{nm}$. In the figure on the right the region around the buried quantum dot and the ring is enlarged. The numbers define the InAs concentration. The concentration of the areas I-III and a-f is given in table 4.3.

Fig. 4.22 (left) shows a two-dimensional cut through the QR model. Like in Fig. 2.21 the mesh density for the creation of the finite elements was chosen according to the expected gradient in the strain field. The substrate has a size of $200\text{nm} \times 37\text{nm}$, large enough that a further increase does not influence the calculated displacement field.

Fig. 4.22 (right) shows the region around the ring structure in more detail. According to the growth models presented in section 4.1.2 it is assumed that the QR consists of the buried *rest of a quantum dot* grown on top of a wetting layer and a free-standing *ring structure*. In the dot rest three regions of different InAs concentration can be defined (labelled I-III). The general shape of the ring structure has been modelled on the basis of AFM and especially GISAXS

data. (A fine tuning of the ring diameter was done in the course of the FEM simulations.) The concentration gradient in the ring is divided in six areas (a-f). In addition, it is possible to increase or reduce the radius and/or the height of the QR by a multiplicative factor. A few models have been calculated assuming a steeper or flatter shape of the free-standing ring, as well.

In total 75 FEM models have been simulated. In table 4.3 the model parameters of 13 selected simulations are listed. The InAs concentration in the dot rest (I-III), in the ring (a-f), and the radius of the QRs is specified. Identical sets of growth parameters are marked with different colours for easier comparison. For all models the cap layer far away from the QRs is assumed to be of pure GaAs. For the wetting layer a concentration of 50% InAs due to interdiffusion was chosen. However, this value is of minor importance for the simulation as will be discussed in the following section.

simulation number	dot rest			ring						size s
	I	II	III	a	b	c	d	e	f	
1a	75%	75%	50%	90%	75%	65%	50%	30%	15%	1.05
2a	75%	75%	50%	100%	90%	75%	60%	40%	20%	1.05
1b	75%	75%	50%	90%	75%	65%	50%	30%	15%	1.00
2b	75%	75%	50%	100%	90%	75%	60%	40%	20%	1.00
1c	75%	75%	50%	90%	75%	65%	50%	30%	15%	0.95
2c	75%	75%	50%	100%	90%	75%	60%	40%	20%	0.95
3a	75%	75%	50%	20%	15%	15%	15%	10%	10%	1.05
4a	75%	75%	50%	10%	10%	10%	10%	10%	5%	1.05
3b	75%	75%	50%	20%	15%	15%	15%	10%	10%	1.00
4b	75%	75%	50%	10%	10%	10%	10%	10%	5%	1.00
5	100%	90%	80%	90%	75%	65%	50%	30%	15%	1.00
6	40%	40%	20%	90%	75%	65%	50%	30%	15%	1.00
7	75%	75%	50%	50%	40%	30%	20%	20%	10%	1.00

Table 4.3: Parameters for selected FEM simulations of quantum rings: I-III, and a-f give the InAs concentration in the dot rest and in the ring as defined in Fig. 4.22. Parameter s is a multiplicative factor to increase or reduce the QR radius.

The $q_{rad} - q_z$ and $q_{rad} - q_{ang}$ reciprocal space maps have been calculated using a simulation program written by V. Holý. For the simulation the displacement field u_x in a plane through the centre of the QR was extracted into a 400×386 matrix of equally spaced points.

The use of only a two-dimensionally calculated displacement field for the simulation of the diffraction patterns is justified by the independence of the displacement field from cuts with different azimuthal orientations. The resolution of these simulation along q_x and q_z is determined by the area used for the FEM calculation. For the described simulation size ($200\text{nm} \times 37\text{nm}$) the resolution is 0.003\AA^{-1} and 0.017\AA^{-1} in x and z direction, respectively. The step width $\Delta x = 5\text{\AA}$, $\Delta z = 1\text{\AA}$ of the FEM calculation determines the maximum size of the simulated map in reciprocal space, in this case more than 1\AA^{-1} in lateral direction.

4.4 Evaluation and discussion

The quantum ring structure as developed in the previous chapter is a highly complex multi-parameter model. The size, shape and concentration profile of both the dot rest and the ring have an important influence on the calculated displacement field and strain. In the following section several case studies are discussed for a better understanding of the reliability of the best simulation results shown in the second part.

Case studies

With the following case studies it is only possible to cover a small part of the complex parameter field of all possible simulations. On the other hand, they show a clear trend which supports the interpretation of the model calculations. For the final results additional combinations and parameters (like dot shape and concentration gradient) have been taken into account. For an easy comparison, radial scans were simulated with the intensity integrated along q_z .

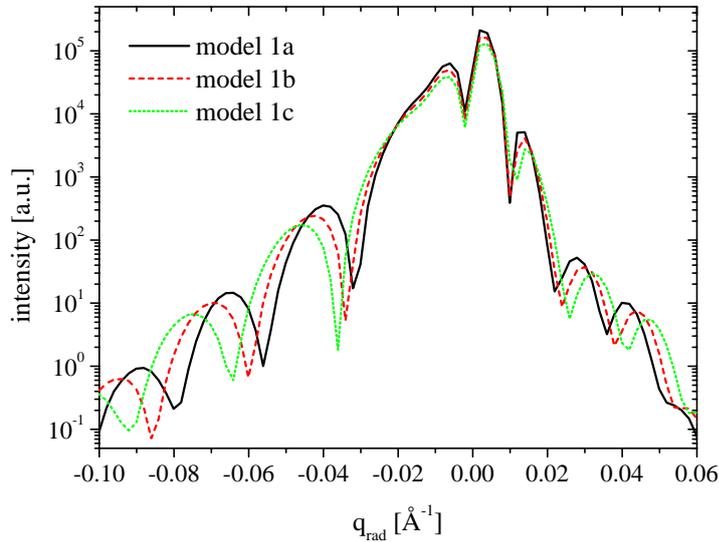


Figure 4.23: FEM case study: change of the QR radius. The radius of model 1a and 1c is 105% and 95% of the radius of model 1b.

Fig. 4.23 shows studies of the effect when the QR radius is changed. Simulation 1a, 1b, and 1c have all the same concentration profile in the dot rest and in the ring. Only the radius of the QR changes between 105% and 95% of the original size. An increase of the radius results in a decrease of the period of all the observed oscillations and vice versa.

Fig. 4.24 compares three simulations with different concentration profiles in the dot rest. The maximum InAs concentration changes from 100% (model 5) to 75% (model 1b) and 40% (model 6). The concentration in the ring and the radius were not modified. The different InAs concentration profiles in the dot basically influence the magnitude of the displacement field u_x , whereas the general distribution always stays the same (similar to Fig. 4.26 for model 2b). The period of the oscillations for $q_{\text{rad}} > 0 \text{ \AA}^{-1}$ which are attributed to a compressed region of GaAs

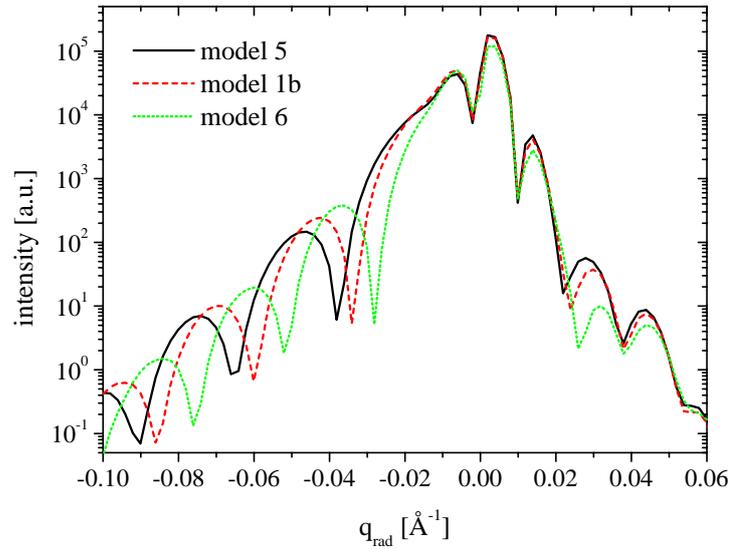


Figure 4.24: FEM case study: change of the InAs concentration in the dot rest. The maximum InAs concentration in the ring is 90%. In the dot rest it changes from 100% (model 5) to 75% (model 1b) and 40% (model 6).

around the QR do not change because the size of this region doesn't vary. The modulations for $q_{\text{rad}} < 0 \text{ \AA}^{-1}$ induced by the shape of the QRs are affected by the changing magnitude of the displacement field (smaller period for lower InAs concentration and weaker displacements).

Fig. 4.25 compares the influence of the InAs concentration in the ring. The concentration in the dot rest and the radius of the structure are unmodified. The maximum InAs concentration

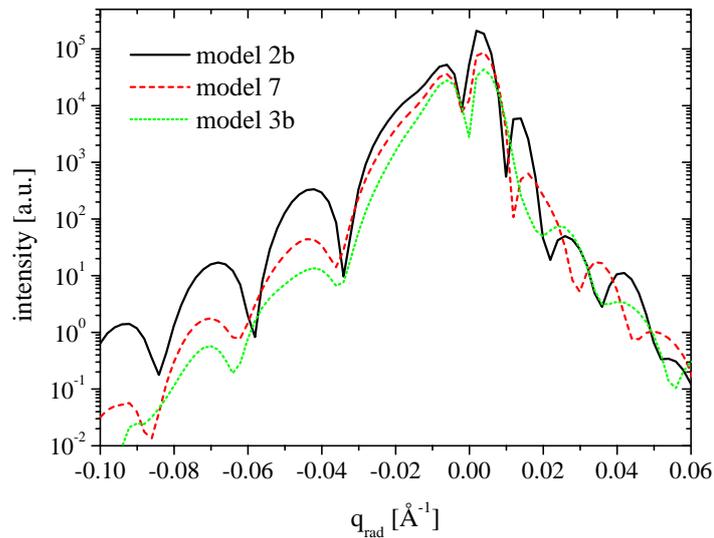


Figure 4.25: FEM case study: change of the InAs concentration in the ring. The maximum InAs concentration in the dot rest is 75%. In the ring it changes from 100% (model 2b) to 50% (model 7) and 20% (model 3b).

in the ring changes from 100% (model 2b) to 50% (model 7) and 20% (model 3b). These variations have an important influence on the displacement field u_x . Fig. 4.26 shows the displacement field of model 2b, Fig. 4.27 the one of model 3b. The corresponding strain distribution ϵ_{xx} of the two models is shown in Figs. 4.28 and 4.29. The higher InAs concentration (model 2b) results in a stronger strain field which is more concentrated in the ring. Stronger displacements (max. 0.12\AA) are observed at the outer surface of the ring as compared to the other two models. In the case of a low InAs concentration in the ring (model 3b) the maximum of the displacement field is more centred in the ring with an maximum displacement of only 0.07\AA .

The oscillations for $q_{\text{rad}} > 0\text{\AA}^{-1}$ are shifted due to the changing distribution of the displacement field in the QR (smaller period for higher concentration). For $q_{\text{rad}} < 0\text{\AA}^{-1}$ the period of the oscillations remains basically unchanged but the amplitude of the maxima decreases dramatically with decreasing concentration.

Best simulation

From the comparison of these case studies three main conclusions are drawn.

- Pronounced intensity modulations for $q_{\text{rad}} < 0\text{\AA}^{-1}$ can *only* be achieved by a high concentration of InAs in the ring, whereas a low concentration helps to suppress these oscillations largely. The positions of the maxima for $q_{\text{rad}} < 0\text{\AA}^{-1}$ do not depend on the InAs concentration in the ring, while a shift of the maxima for $q_{\text{rad}} > 0\text{\AA}^{-1}$ is observed.
- A variation of the InAs concentration in the dot rest influences the position of the maxima for $q_{\text{rad}} < 0\text{\AA}^{-1}$. The modulation for $q_{\text{rad}} > 0\text{\AA}^{-1}$ is almost unaffected.
- An increase or reduction of the QR radius changes the period of all observed oscillations.

These three facts are necessary to explain and simulate the different shapes of the radial measurements at the $(2\bar{2}0)$ and (220) reflection shown in Figs. 4.14 and 4.16. While the two measurements are almost identical for $q_{\text{rad}} > 0\text{\AA}^{-1}$, the measurement at the $(2\bar{2}0)$ reflection shows more pronounced modulations for $q_{\text{rad}} < 0\text{\AA}^{-1}$. As the shape of the QRs is known to be identical in all directions (GISAXS, AFM) the difference has to be explained with a distinct strain caused by the InAs concentration profile of the QR.

According to the results of the case studies, only a difference in the InAs concentration *of the ring* along the two crystallographic directions can explain the experimental results. Thus, for the simulation of the measurement at the $(2\bar{2}0)$ reflection a high InAs concentration of more than 90% has been assumed, whereas a concentration of less than 20% has to be used for the simulation of the measurement at the (220) Bragg peak.

To reproduce the correct position of the oscillations either a change of the QR radius or the InAs concentration in the dot rest has to be assumed, as both variations have similar results. To limit the number of free parameters the radius of the QRs was restricted on the basis of the simulation of the GISAXS data.

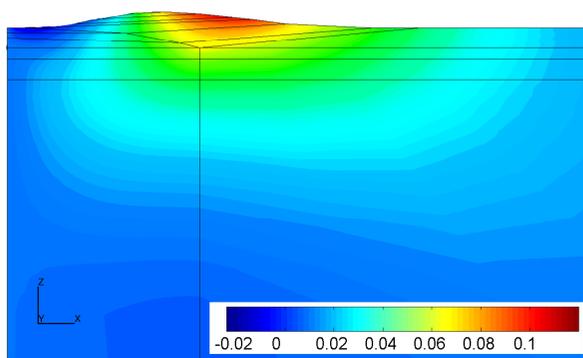


Figure 4.26: FEM simulation of the displacement field u_x [in nm] assuming a high InAs concentration in the quantum ring (model 2b). This displacement is used to simulate the measurements at the $(\bar{2}20)$ Bragg reflection.

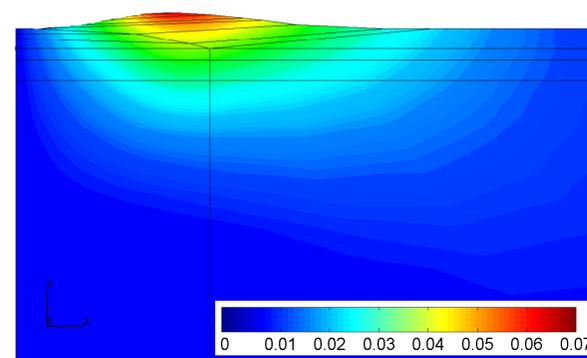


Figure 4.27: FEM simulation of the displacement field u_x [in nm] assuming a low InAs concentration in the quantum ring (model 3b). This displacement is used to simulate the measurements at the (220) Bragg reflection.

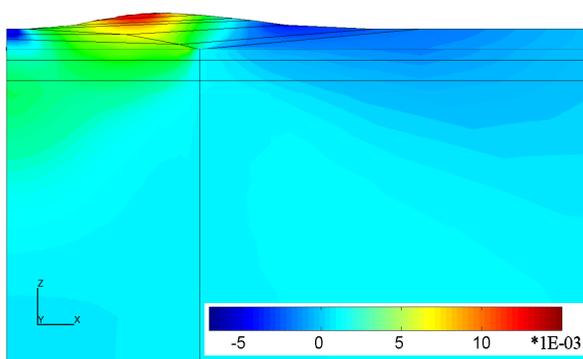


Figure 4.28: FEM simulation of the strain ϵ_{xx} assuming a high InAs concentration in the quantum ring (model 2b).

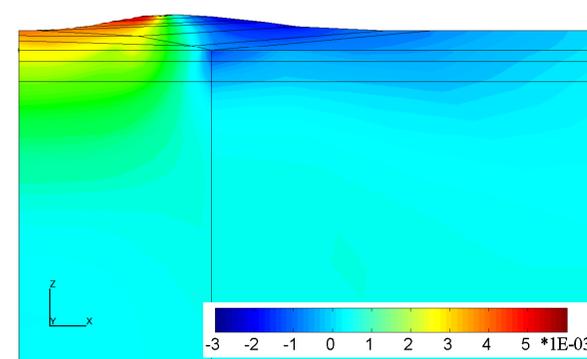


Figure 4.29: FEM simulation of the strain ϵ_{xx} assuming a low InAs concentration in the quantum ring (model 3b).

The best simulation results are shown in Figs. 4.30 and 4.31. To take into account the thermal diffuse scattering close to the Bragg peak an intensity distribution with a decay of $1/q^2$ is added to the simulations. A small size and concentration distribution within the investigated dot ensemble is accounted for by averaging over models with slightly varying parameters.

In the case of the radial measurement at the $(2\bar{2}0)$ peak (see Fig. 4.30) two models with an maximum InAs concentration in the ring of 90% (model 1) and 100% (model 2), respectively, have been calculated. For each model a size distribution of $\pm 5\%$ was assumed (model a, b, c). The best fit shown in the solid red line reproduces very well the central part, the position of the first side maximum for $q_{\text{rad}} < 0\text{\AA}^{-1}$, and both oscillations for $q_{\text{rad}} > 0\text{\AA}^{-1}$. The existing differences in intensity and at the position of the second maximum for $q_{\text{rad}} < 0\text{\AA}^{-1}$ have to be explained with the complexity of the multi-parameter model which makes it difficult to reproduce all of the experimental features. In addition, it is not possible to “fit” the measured data. Rather it is a continuous refinement of parameters of the FEM simulation until the best possible agreement between experiment and simulation is achieved.

The InAs concentration profile in the dot rest is based on investigations by Kegel et al. [Kegel00b, Kegel01]. According to these results a strong interdiffusion resulting in free-standing QDs with an InAs concentration of 50% at the base and 100% InAs at the apex was assumed. As the dot material diffuses outwards according to the model by Lorke et al. the concentration in the dot rest reaches from 50% at the base to 75% at the top. These assumption together with a radius of $\approx 28\text{nm}$ provides a good approximation of the measurement. The radius is in good agreement with the GISAXS simulations.

The measurement at the (220) reflection has been simulated by models with 10% (model 4) and 20% InAs (model 3) as a maximum concentration in the ring and the same concentration in the dot rest as at the (220) Bragg peak. Again a size distribution of $\pm 5\%$ for the radius (model a,b) has been averaged and is shown as dashed lines in the figure.

Concerning the error of these simulations one has to admit an uncertainty of the maximum InAs concentration in the dot rest between 50% and 80% and $(27 \pm 3)\text{nm}$ in the QR radius due to the coupled influence of the InAs concentration in the dot rest and the QR radius on the modulations.

On the other hand, the error of the InAs concentration in the ring is very low. In the case of the simulation at the $(2\bar{2}0)$ reflection only a concentration of more than 85% can reproduce the strong modulations for $q_{\text{rad}} < 0\text{\AA}^{-1}$. A concentration of less than 20% has to be used to reproduce the measurement at the (220) reflection.

Further model parameters have shown to be of minor importance: for example, the InAs concentration in the wetting layer. A flatter shape of the rim or a change of the height of the QR ($\pm 0.2\text{nm}$) induces a change of the modulations which are within the uncertainty of other model parameters (radius, concentration).

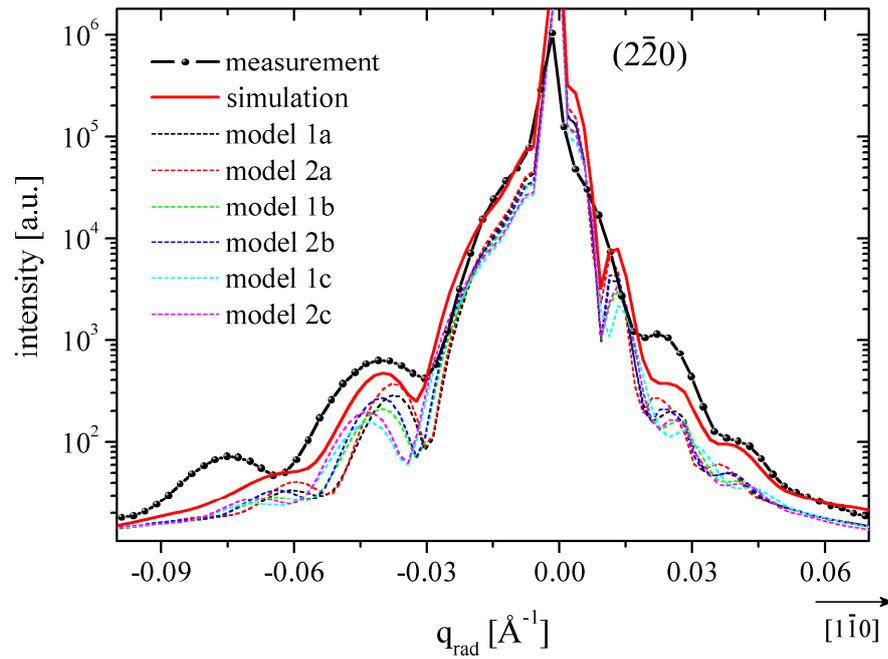


Figure 4.30: Best simulation for the radial measurement at the $(2\bar{2}0)$ Bragg reflection. A statistical distribution is taken into account by averaging over six models shown in dashed lines.

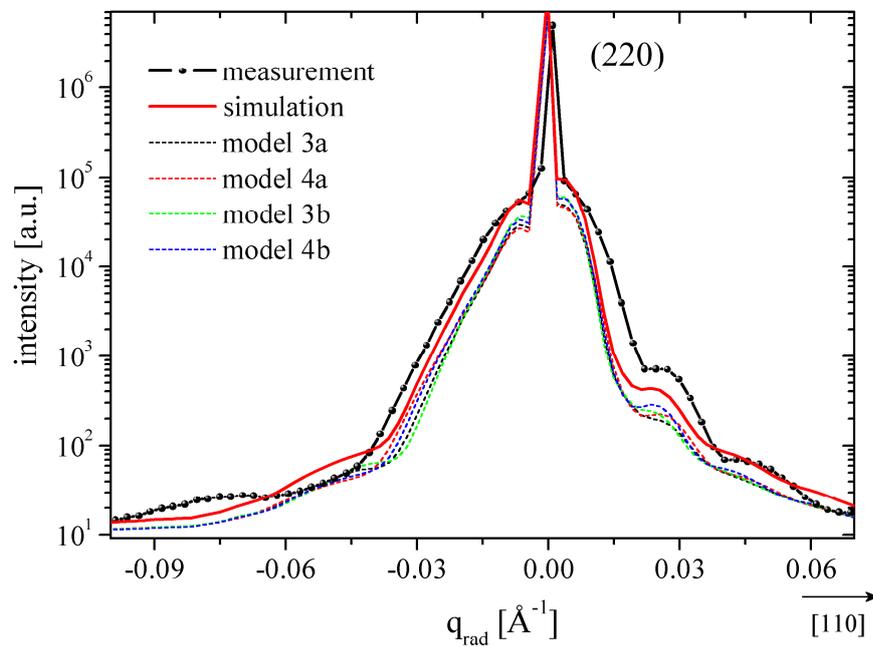


Figure 4.31: Best simulation for the radial measurement at the (220) Bragg reflection. A statistical distribution is taken into account by averaging over four models shown in dashed lines.

In addition, the best simulation results are confirmed by comparing calculated $q_{\text{rad}} - q_z$ and $q_{\text{rad}} - q_{\text{ang}}$ mappings as well as angular cuts with the experimental data (see Figs. 4.32 to 4.37). For an easy comparison the corresponding measurements which have already been shown in chapter 4.2.3 are presented again.

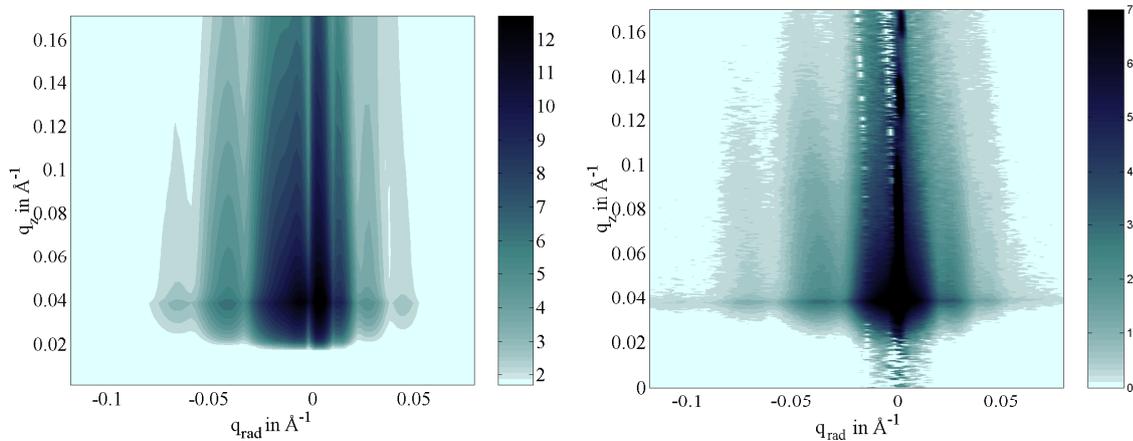


Figure 4.32: Comparison of the simulated (left) and measured (right) $q_{\text{rad}} - q_z$ mapping at the $(2\bar{2}0)$ Bragg reflection.

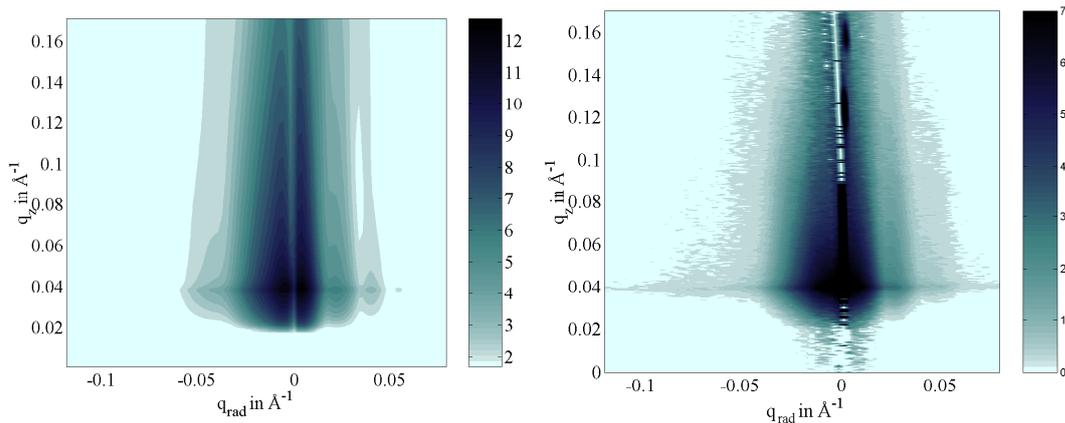


Figure 4.33: Comparison of the simulated (left) and measured (right) $q_{\text{rad}} - q_z$ mapping at the (220) Bragg reflection.

The vertical lines in Figs. 4.34 and 4.35 mark the position of the angular scans. However, in the case of the simulations the values in between are also calculated. Therefore, these plots show more details than the interpolated mappings of the experimental data. In general a satisfactory agreement of measurements and simulations is achieved, considering the complexity and interdependence of the parameter field

Figs. 4.36 and 4.37 show selected angular simulations and measurements at the $(2\bar{2}0)$ and (220) reflection, respectively. The radial position of the presented angular cuts do not differ more than 0.002\AA^{-1} from the nominal position of the measurement. Again a background, taking into account the thermal diffuse scattering at the Bragg peak is added. Although the simulations have not been “fitted” they show a good agreement with the experiment. The

height of the observed maxima is not always exactly matched. However, this depends very sensitively on the simulation parameters. On the other hand, the general features like the different ratio between the height of the central peak and the side maxima can be very well reproduced.

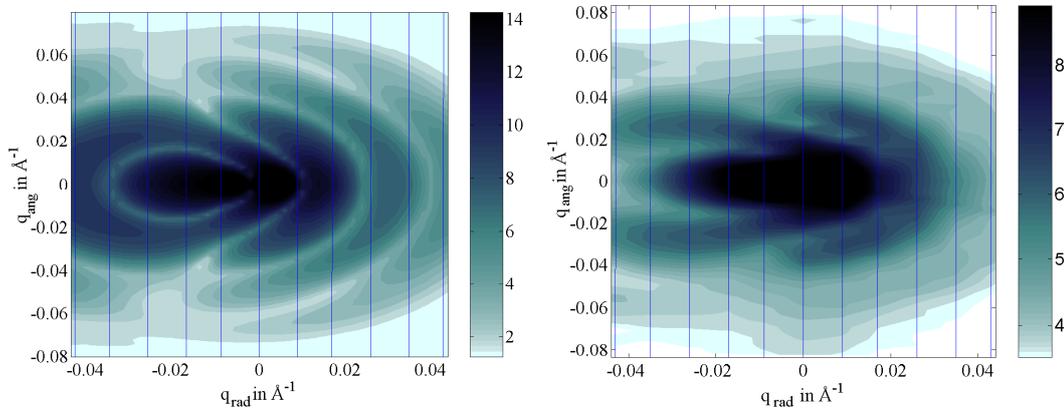


Figure 4.34: Comparison of the simulated (left) and measured (right) $q_{\text{rad}} - q_{\text{ang}}$ mapping at the (220) Bragg reflection. The light blue lines mark the radial positions where the angular *measurements* have been recorded.

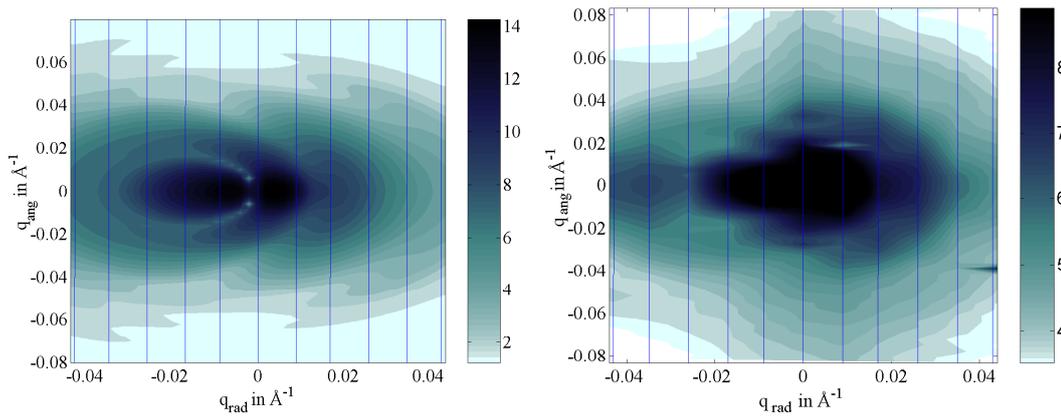


Figure 4.35: Comparison of the simulated (left) and measured (right) $q_{\text{rad}} - q_{\text{ang}}$ mapping at the (220) Bragg reflection. The light blue lines mark the radial positions where the angular *measurements* have been recorded.

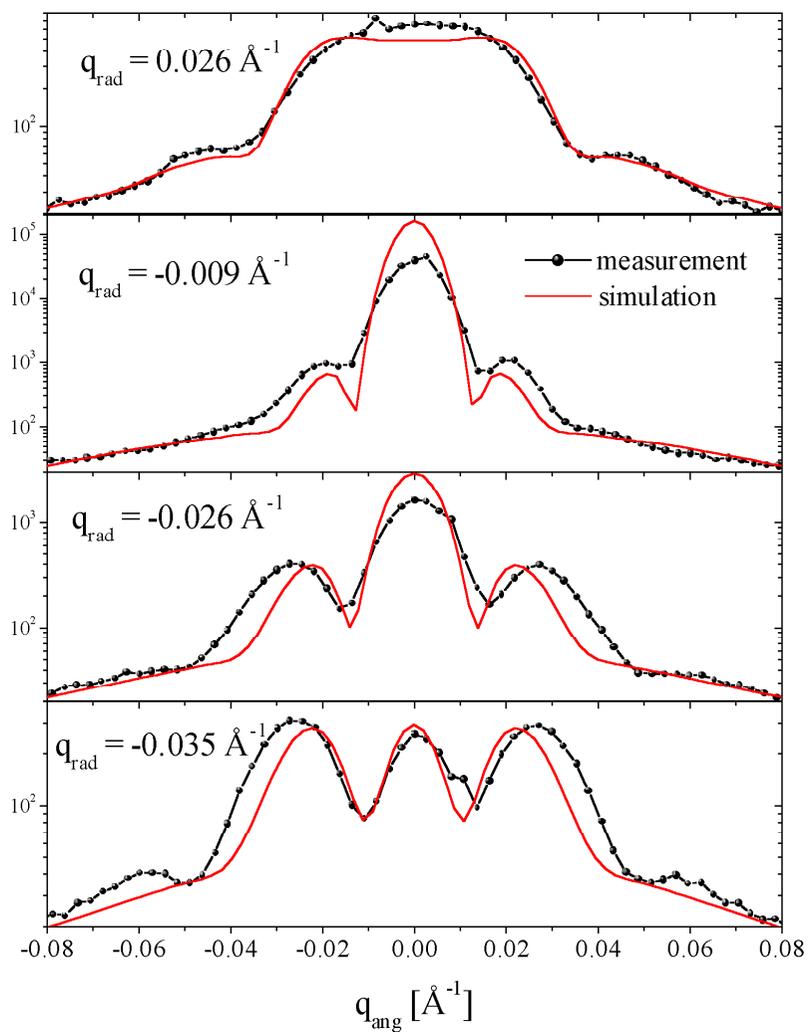


Figure 4.36: Selected angular simulations at the $(\bar{2}20)$ Bragg reflection are compared to the corresponding measured data.

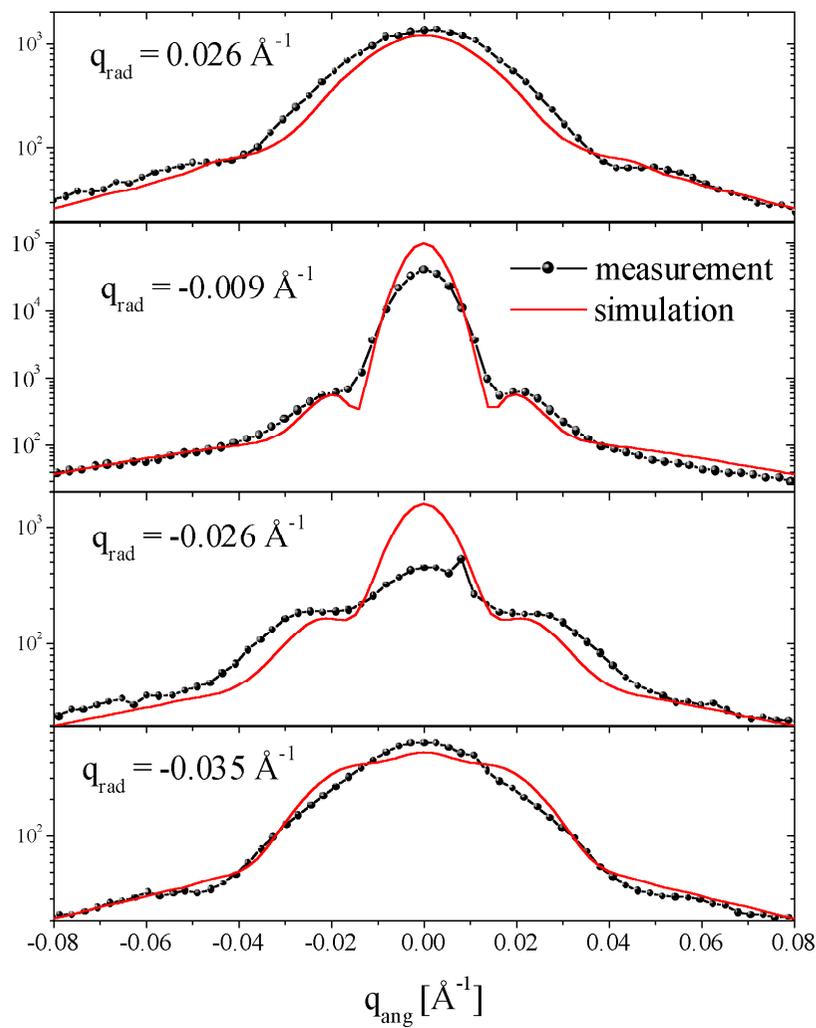


Figure 4.37: Selected angular simulations at the (220) Bragg reflection are compared to the corresponding measured data.

Summary

From the GISAXS and AFM measurements it can be concluded that the investigated quantum rings have a *homogeneous circular shape*. The average radius is (26 ± 2) nm, the height (1.5 ± 0.2) nm. The depth of the central hole is comparable to the rim height above the substrate surface.

In contrast, the FEM based case studies show that the InAs *concentration profile* in the ring along the two $\langle 110 \rangle$ directions is *very inhomogeneous* (see Fig. 4.38). In one direction, assumed to be $[1\bar{1}0]$, the InAs concentration in the ring has a maximum concentration of more than 85% with a decreasing gradient towards the GaAs capping layer. In $[110]$ direction the maximum concentration in the ring is below 20%. This difference is explained with the preferred diffusion of In along the $[1\bar{1}0]$ direction. The InAs concentration in the dot rest of the buried island cannot be determined with the same accuracy. It is in the range between 50% and 80% InAs for both $\langle 110 \rangle$ orientations measured.

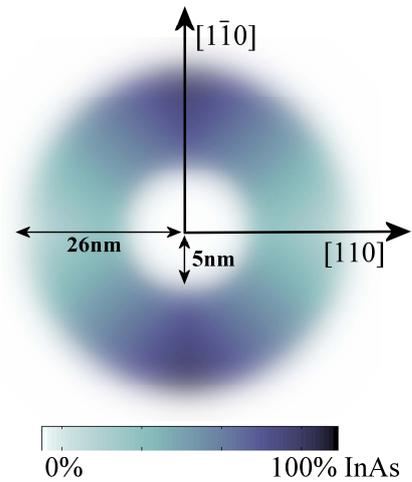


Figure 4.38: Summary of the quantum ring model.

These results favour the *diffusion driven model* (see section 4.1.2) to explain the transformation from dots to rings during overgrowth since a significant material transport is required to obtain the inhomogeneous composition profile of the rings. The preferred In diffusion along the $[1\bar{1}0]$ direction is supported only by this model.

The alternative model of a *wetting droplet instability* might be an appropriate model to describe the shape transformation. However, it cannot explain the inhomogeneous concentration profile in the rings.

So far only the composition profile in $[110]$ and $[1\bar{1}0]$ direction has been determined experimentally. The investigation of the interdiffusion along other crystallographic directions (e.g. $[100]$ and $[010]$ by measuring at the (400) and (040) Bragg reflections, respectively) can help to refine the model.

A direct determination of the InAs composition using contrast variation by anomalous diffraction is not possible due to the rather complex configuration of the rings which does not allow for a clear separation of shape and strain contributions along the radial intensity distribution (see section 4.2.3).

However, *anomalous GISAXS* should be a useful technique for a further characterisation of the rings [Goerigk03]. This technique is *element specific* by measuring e.g. at energies near the L absorption edge of In. For GISAXS measurements at 8.0keV no azimuthal dependence of the small angle scattering signal has been observed (see Fig. 4.10). However, a change of the small angle scattering for the InAs rich $[1\bar{1}0]$ and the GaAs rich $[110]$ direction using anomalous GISAXS could support the findings of the GID investigation. Moreover this technique can be applied for all azimuthal orientations of the sample.

Chapter 5

Cleaved Edge Overgrowth (CEO)

5.1 Motivation

The investigation of semiconductor quantum wires (QWRs) and dots (QDs) with quantum confinement of charge carriers to one (1D) or zero dimensions (0D), respectively, has become an increasingly important research field in semiconductor physics, as these structures show unique electronic and optical properties compared to systems of higher dimensionality.

Several techniques can be applied to produce these structures as already described in chapter 1. Each technique shows particular advantages and drawbacks. Introducing additional confinement by lateral patterning will affect the optical properties of these structures as atomically flat interfaces are required. However, the patterning by lithographic techniques or focussed ion beams can result in variations of the width of the QWRs due to imperfect interfaces. This results in a broadening of the photoluminescence (PL) linewidths. Molecular beam epitaxy (MBE) allows for the growth of interfaces with atomic precision. On the other hand, the self-organised (Stranski-Krastanov) growth of quantum dots by MBE shows another disadvantage: its inherent randomness of the formation process, concerning size, shape and position of the QDs. All this leads again to a broadening of the PL spectra. In addition, it is impossible to address precisely one or just a few nanostructures in future electronic devices.

Therefore, it seems necessary to precisely control the size, shape and position of the QDs before they can be used in device applications.

Cleaved edge overgrowth (CEO), a MBE technique that uses high-quality overgrowth on the cleaved edge of a multilayer sample [Pfeiffer90] has proven to be a powerful technique for the fabrication of T-shaped QWRs which form at the intersection of two QWs. The CEO technique will be introduced in chapter 5.1.1. A further development of the T-shaped QWRs, as proposed by [Regelman99] and theoretically calculated by [Grundmann00], are purely strain modulated quantum wires. The particular properties of these structures are described in chapter 5.1.2. Arai et al. [Arai97a, Usami98] have used Stranski-Krastanov growth on a cleaved edge to control size and position of semiconductor islands in the material system Si/Ge. Chapter 5.1.3 is concerned with this approach.

In both cases (strain-induced QWRs and ordering of QDs) a detailed knowledge about the strain distribution in the overgrown layer is important, and has not been studied experimentally so far. The chapters 5.2 and 5.3 deal with the investigations of this strain distribution by x-ray techniques.

5.1.1 Technique

The cleaved edge overgrowth (CEO) technique, pioneered by Pfeiffer et al. [Pfeiffer90] relies on the overgrowth on the cleaved edge of a previously prepared multilayer heterostructure fabricated by molecular beam epitaxy (MBE). It is thus capable of producing nearly perfect structures (using the atomic control of the MBE process) in more than one direction [Wegscheider97c]. For the samples investigated within this work, the multilayer heterostructure acts as a substrate with an in-plane modulated lattice constant, giving rise to periodic strain modulations in the epitaxial layer grown on the cleaved edge. The presence of strain in these structures introduces a new parameter in band gap engineering due to modified confinement effects [Grundmann00].

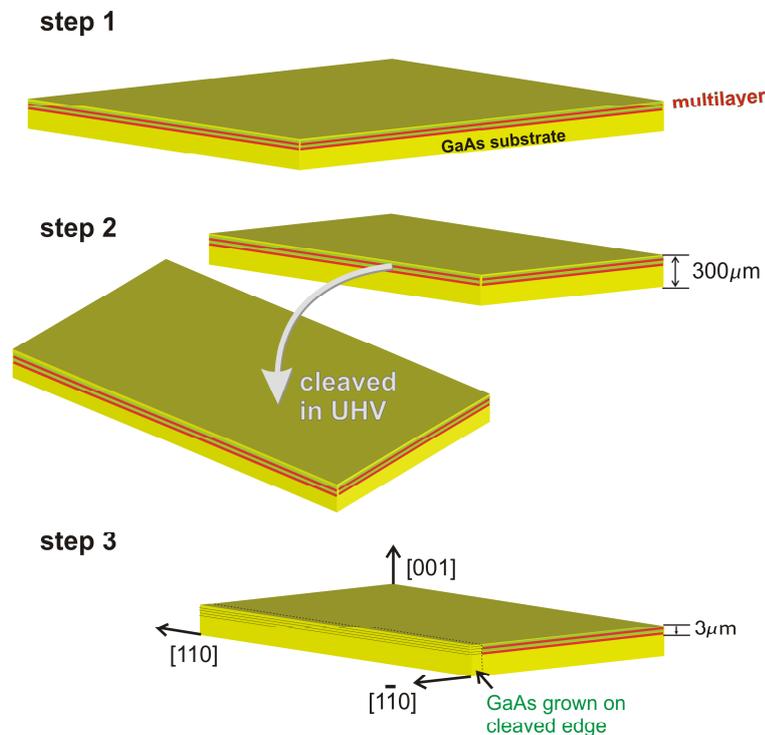


Figure 5.1: Schematic overview of the cleaved edge overgrowth (CEO) sample preparation. On a GaAs (001) substrate a multilayer is deposited (step 1). The thinned sample is then *in-situ* cleaved (steps 2). The fresh (110) surface which is produced by the cleaving is immediately overgrown by the desired structure.

The CEO production process consists of several steps which are sketched in Fig. 5.1. First a GaAs based heterostructure (multilayer) is grown on a GaAs (001) substrate by molecular beam epitaxy (MBE) as is shown in Fig. 5.1 (step 1). In the following this is referred to as the *first growth direction*. Then the wafer is removed from the UHV growth chamber and

thinned from the back surface to less than $300\mu\text{m}$ using a bromine methanol dilution. Pieces of a size of about $7 \times 7\text{mm}^2$ were produced and scribed by a computer controlled system to have a predetermined breaking point for the later *in-situ* cleaving. The samples are cleaned in boiling acetone and methanol, and mounted on a special sample holder. Thereon, the samples are transferred into the UHV chamber and heated up to 420°C for several hours. Back in the growth chamber the samples were annealed at 600°C to remove the oxide layer. After this time consuming treatment, the samples are ready for the actual cleaved edge overgrowth [see Fig. 5.1 (step 2 and 3)]. The samples are *in-situ* cleaved which exposes a fresh $(\bar{1}\bar{1}0)$ surface. The immediate overgrowth of this tiny surface ($300\mu\text{m} \times 7\text{mm}$) ensures the high quality of the structure. This growth in $[\bar{1}\bar{1}0]$ direction is referred to as the *second growth direction*. The second growth has to be carried out on a (110) oriented GaAs, InAlAs or AlGaAs crystal face since these zinc-blende type semiconductors show a strong natural preference for cleaving on (110) lattice planes. Unfortunately, this fact complicates the growth of the CEO layer due to the different reconstruction of the (110) oriented surface as compared to the (001) orientation [BresslerHill92, Wegscheider97a]. The conventional parameters for MBE growth along the $[001]$ direction would result in poor surface morphology and unacceptable optical and transport properties. Therefore, they have to be adapted to this sample orientation [Holmes98]. The growth of InAs QDs on the (110) oriented surface is especially difficult, which will be explained in chapter 5.1.3 in more detail.

5.1.2 T-shaped quantum wires

Confinement

The optical properties of semiconductors are largely determined by the band gap. A photon can be absorbed as soon as its energy $\hbar\omega$ is larger than E_{gap} . By the formation of excitons (electron-hole pairs) the absorption of photons is possible for energies $E < E_{\text{gap}}$ as the energy levels of the excitons lie below the conduction band edge in the band gap. The binding energy of excitons for bulk GaAs is about 4.2meV . Therefore, almost all excitons are ionized at room temperature ($kT \approx 26\text{meV}$). It is possible to overcome this problem as excitons have a higher binding energy if they are localised in one or more dimensions.

By introducing heterostructures the mobility of the charge carriers is confined to two dimensions. The size of these so called quantum wells (QWs) is comparable to the exciton Bohr radius ($\approx 11\text{nm}$). In such QWs the binding energy of the excitons is considerably increased compared to bulk material. As a consequence of this confinement excitons can exist even at room temperature. A further increase of the binding energy is achieved by confinement to one dimension (quantum wires - QWRs).

Several technologies have been implemented to fabricate these structures. Lithographic techniques using focused ion beams are limited to several 100\AA due to the optical resolution. More interesting would be a width smaller than the Bohr radius of excitons in bulk GaAs. In addition, introduction of additional confinement by lateral patterning severely affects the optical quality of the structures [Wegscheider97b].

Cleaved edge overgrowth has proven to be a powerful technique for the fabrication of T-shaped QWRs which form at the intersection of two QWs [Pfeiffer90, Wegscheider97c, Wegscheider98].

This technique was first introduced in 1985 by [Chang85] and is sketched in Fig. 5.2. A QWR forms at the crossing of the GaAs QW grown in $[001]$ direction and the GaAs QW grown in $[110]$ direction on the cleaved edge. As shown in Fig. 5.2(b) the wave functions of electrons and holes extend into the crossing QWs. As a consequence the confinement at the T-shaped crossing and therefore the ground state energy is reduced as the charge carriers are in a more favourable state there. This lowering is of quantum mechanical nature. The structure is invariant in the $[1\bar{1}0]$ direction which leads to a 1D QWR.

As MBE is used for the CEO process all relevant sizes are controlled on an atomic scale. In addition, a high degree of structural perfection (e.g. absence of large inhomogeneous emission line broadening) can be reached. Laser emission from 1D excitons in QWRs has been observed for the first time by [Wegscheider93].

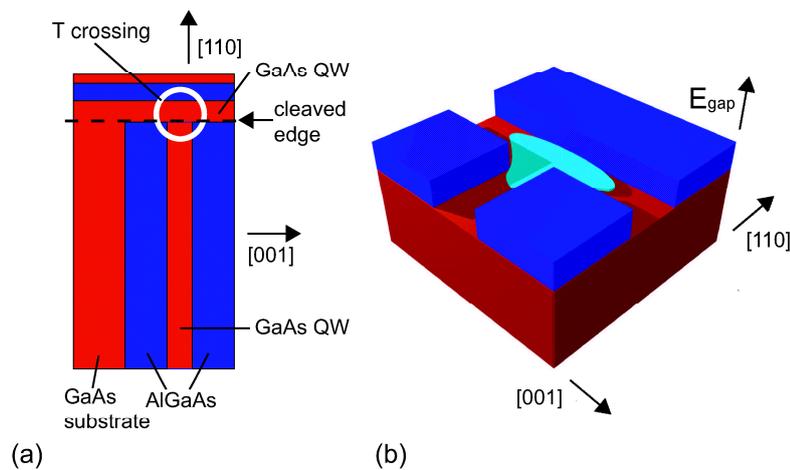


Figure 5.2: Schematic view of a (classical) unstrained T-shaped quantum wire produced by CEO (a). Figure (b) shows a band gap sketch. The probability distribution of the electrons is marked in light blue (taken from [Hajak03]).

As predicted and theoretically modelled [Grundmann97, Wegscheider97b], CEO can also be employed to produce QDs in which charge carriers are confined in all directions [Wegscheider97b, Wegscheider97c, Wegscheider98, Schedelbeck97]. These QDs are fabricated by two-fold cleaved edge overgrowth at the intersection of three quantum wells.

The inclusion of strained layers in such structures introduces a new parameter in band-gap engineering to modify confinement effects.

Strain modulated quantum wires

The inclusion of strained layers in QW structures produced by CEO has already been proposed in 1990 by Gershoni et al. [Gershoni90, Gershoni91]. They presented a quantum wire in which confinement to 1D is produced by one-dimensional pseudomorphic strain (see Fig. 5.3) - in contrast to the QWR structure which is formed when the wave functions of electrons and holes extend into crossing QWs (see Fig. 5.2).

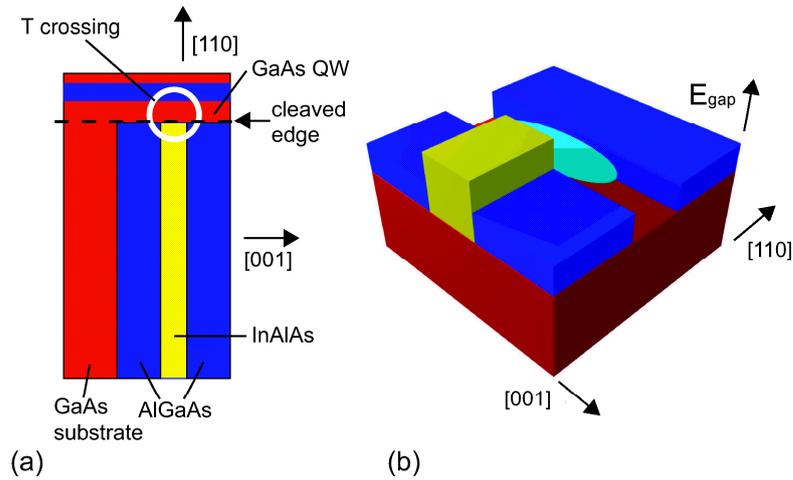


Figure 5.3: Schematic view of a purely strain modulated quantum wire produced by CEO (a). Figure (b) shows a band gap sketch. The probability distribution of the electrons is marked in light blue. In contrast to the unstrained T-shaped quantum wire (Fig. 5.2) there is no quantum well grown in [001] direction. The quantum wire is purely strain-induced (taken from [Hajak03]).

In order to use the maximum strain directly at the interface of the cleaved edge it is necessary to grow the QWR directly on top of the cleaved edge. The distorting material has to have a larger band gap than GaAs to form a barrier for the CEO QW. This is the case if a multilayer of InAlAs and AlGaAs is grown [instead of GaAs and AlGaAs, as in the case of the unstrained T-shaped QWR (see Fig. 5.2)].

The investigated samples are based on a configuration proposed by Regelman et al. [Regelman99]. They have presented the design of a lower dimensionality lasing device based on a quantum wire of nanometre cross-section embedded in its active region. The laser would be fabricated by the cleaved edge overgrowth technique and is expected to have a narrower gain spectrum, lower threshold currents, and a lower temperature dependence of its efficiency. Theoretical calculations show confining energies for both, electrons and holes, which are significantly higher than the thermal energy at room temperature. Thus, the proposed device is likely to operate well at room temperature.

Fig. 5.4 describes schematically the proposed heterostructure. It consists of a (001) oriented periodic structure of alternating 100Å and 300Å thick layers of $\text{In}_{0.2}\text{Al}_{0.8}\text{As}$ and $\text{Al}_{0.35}\text{Ga}_{0.65}\text{As}$ respectively, which do *not* form quantum wells, but exert tensile strain on the 100Å GaAs QW and $\text{Al}_{0.35}\text{Ga}_{0.65}\text{As}$ barrier grown in the [110] direction on top of the cleaved edge. The band gap of the (001) InAlAs (and AlGaAs) layers is sufficiently high that the charge carriers are confined to the GaAs layer [see Fig. 5.3(b)]. This configuration of the CEO structure creates a different physical situation: the lateral charge carrier localisation (along [110]) to 1D QWRs is not due to heterostructure barriers but solely due to the induced tensile strain in the (110) layer.

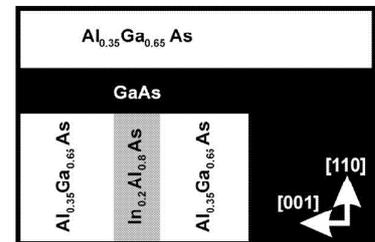


Figure 5.4: Geometry of the strained CEO quantum wire as theoretically investigated by [Grundmann00].

The lateral dimension of these strained QWRs are comparable to the dimensions of the intersecting QW layers from which they are formed. In order to make these devices applicable, the energy associated with the lateral confinement has to be largely enhanced. Regelman et al. [Regelman99] have theoretically shown that this can be achieved by the combined effect of strain and geometry in such a novel CEO heterostructure.

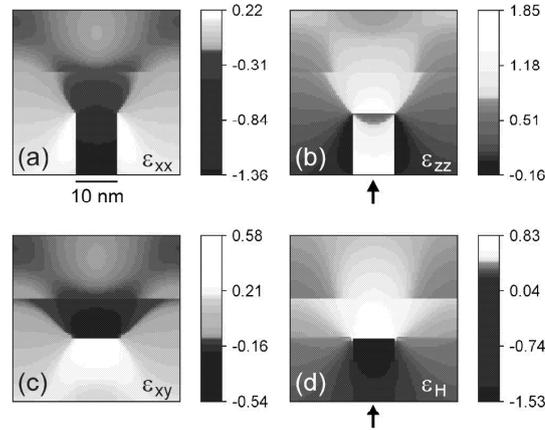


Figure 5.5: Strain components (a) ε_{xx} , (b) ε_{zz} , (c) ε_{xy} , and (d) $\varepsilon_H = \varepsilon_{xx} + \varepsilon_{yy} + \varepsilon_{zz}$ for the quantum wire shown in Fig. 5.4. The x , y , and z directions correspond to $[100]$, $[010]$, and $[001]$, respectively. The calculation was taken from [Grundmann00].

The existence of QWRs fabricated purely by tensile strain has been theoretically calculated by Grundmann et al. [Grundmann00]. In their work they study the configuration proposed by [Regelman99] and sketched in Fig. 5.4. A continuum mechanical model has been used for the calculation of the strain distribution. Their results are shown in Fig. 5.5 for several strain components. The strain is always given relative to the relaxed material of the respective layer. In addition, they have calculated the wave function of electrons and holes. As can be seen in Fig. 5.6 the wave function does not extend into the InAlAs layer of the $[001]$ growth - in contrast to the classical geometry shown at the beginning of this chapter. For a QWR structure as described above with a CEO GaAs layer (in $[110]$) of 50 or 100Å a confinement energy of 44.7meV or 62.5meV, respectively, is predicted. A further enhancement of the confinement energy is achieved by increasing the $\text{In}_{0.2}\text{Al}_{0.8}\text{As}$ layer thickness during the growth in $[001]$ direction e.g. to 150Å. In this case a confinement energy of 86.6meV has been calculated. Another possibility to enhance the confinement energy is to raise the induced strain by increasing the In concentration of the InAlAs layer. The upper limit for the choice of the layer thickness and the In concentration is always the critical thickness for dislocation formation [Grundmann90].

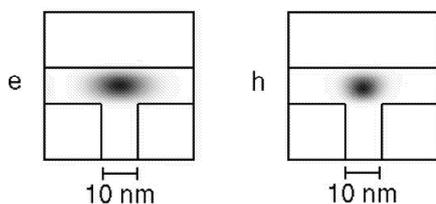


Figure 5.6: Wave function for electron (e) and hole (h) levels calculated for the QWR structure described in 5.4 (taken from [Grundmann00]).

Investigated samples

Recently, Robert Schuster [Schuster03] and Harald Hajak [Hajak03] demonstrated the existence of purely strain-induced QWRs produced by CEO using photo luminescence (PL) spectroscopy with high spectral and spatial resolution. The sample they have investigated corresponds to the structure shown in Fig. 5.4. For a CEO GaAs layer of 70Å they find a confinement energy of 42meV. Due to the high spatial resolution it was possible to localise the QWRs in the strained GaAs QW above the (001) InAlAs layers. These results confirm the theoretical predictions by Grundmann et al. [Grundmann00].

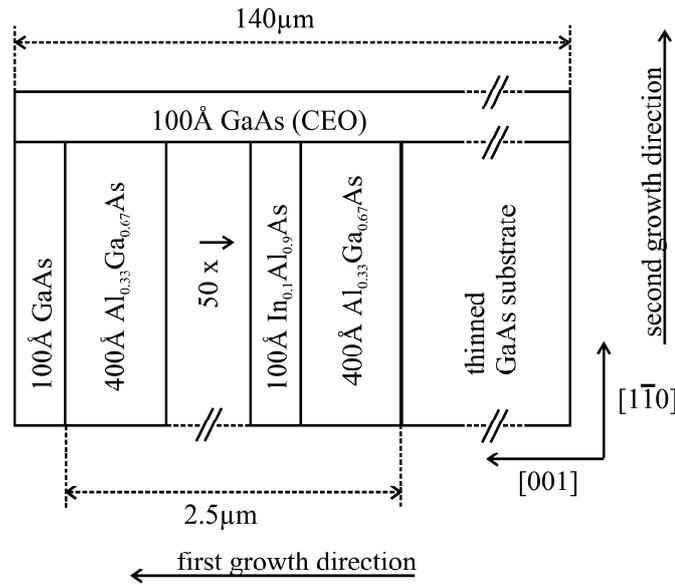


Figure 5.7: Cleaved edge overgrowth: schematic diagram of the sample layout obtained after two growth steps.

A slightly modified sample was prepared for the investigation by x-rays containing only the essential structures. In the $[1\bar{1}0]$ direction in particular only a GaAs layer of 100Å thickness was grown. A barrier and cap layer was abandoned to allow for an undisturbed investigation by grazing incidence x-ray diffraction.

This sample structure is displayed in Fig. 5.7: on a GaAs (001) substrate a superlattice of 50 times 400Å Al_{0.33}Ga_{0.67}As and 100Å In_{0.1}Al_{0.9}As was grown, ending with 400Å Al_{0.33}Ga_{0.67}As and a 100Å cap layer to prevent oxidation of the aluminium. For the strain investigation the cleaved edge was overgrown with 100Å GaAs. Two further samples were prepared with 70Å and 130Å GaAs coverage for comparison. Quantum wires form only if the GaAs CEO layer is overgrown with a barrier of Al_{0.33}Ga_{0.67}As. This structure was grown for the samples investigated by PL spectroscopy.

It is important to note that only a width of 2.5µm within the GaAs CEO layer is strain modulated. The sample in total is not thicker than 140µm which makes the x-ray investigation of these samples challenging.

5.1.3 Self-organised ordering of quantum dots

Another application for cleaved edge overgrowth is to control position and size of semiconductor islands using the periodic strain of the quantum wells. Arai and Usami et al. [Arai97a, Arai97b, Usami98] have used Stranski-Krastanov growth on the cleaved edge in the material system Si/Ge. The strained multiple quantum well in their samples consists of a series of 5 times $\text{Si}_{0.8}\text{Ge}_{0.2}/\text{Si}$ (first growth direction). The SiGe width varies between 200 and 400Å. The Si layer always has a width of 300Å. This forms a (110) substrate with an in-plane modulated lattice constant giving periodically modulated strain to epitaxial layers. Ge islands were found to selectively grow on the cleaved edge of SiGe at 600°C and on that of Si at 500°C (second growth direction). Fig. 5.8 shows atomic force microscopy (AFM) images of a sample which was overgrown with 6ML of Ge on top of the cleaved edge. The Ge islands grow aligned in straight lines along the quantum wells. The size of the Ge islands depends on the well width, which varied between $L_{\text{SiGe}} = 200\text{Å}$ and 400Å.

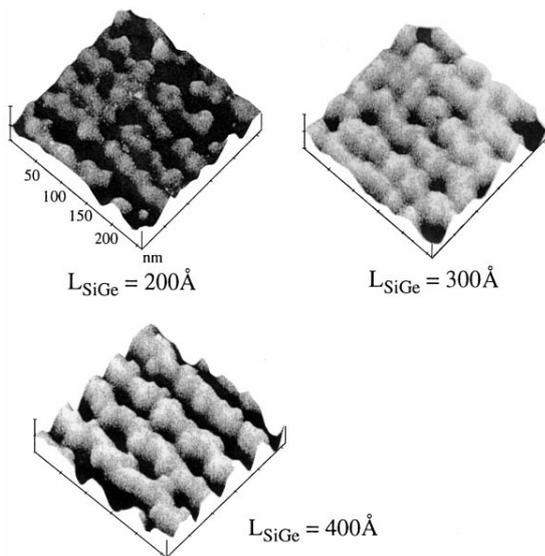


Figure 5.8: AFM image of 6ML of Ge grown on top of a $\text{Si}_{0.8}\text{Ge}_{0.2}/\text{Si}$ strained multiple quantum well (taken from [Usami98]).

The (second) growth of the quantum dots has to be carried out on a (110) oriented crystal surface. Especially for the investigated sample system of GaAs, InAs, and AlAs this fact complicates the MBE growth. Choosing growth conditions that are usually employed for the growth on (100) oriented crystals leads to a rough (110) surface containing either Ga droplets or macroscopic triangular shaped islands [Allen87, Wassermeier94].

It was a breakthrough for the MBE growth of III-V compounds, when Allen et al. [Allen87] achieved growth of device quality (110) GaAs for the first time in 1987. Films with good surface morphology can now be grown in particular under more arsenic rich conditions and using much lower substrate temperatures [Fawcett94]. This behaviour is explained by the smaller and strongly temperature-dependent arsenic incorporation co-efficient on GaAs (110) compared to GaAs (001), necessitating low substrate temperatures of about 490°C and a supersaturation of As. In addition, a transition from monolayer-by-monolayer growth to a bilayer growth has been observed [Wassermeier94] - depending on growth parameters like temperature and the kind of arsenic species (As_2 or As_4) used in the incident beam.

Taking into account the range of possible growth conditions it can be understood that the growth of ordered InAs quantum dots on top of the cleaved edge is rather complicated, but not impossible. Dieter Schuh [Schuh03] at the Walter Schottky Institute in Garching is currently working on this topic.

A detailed knowledge of the strain distribution in CEO layers will generate a better understanding of growth and alignment of nanostructures on strained CEO surfaces. In the following, x-ray techniques are presented and applied to measure this quantitatively.

5.2 Experiment

The strain distribution within a GaAs layer overgrown on the cleaved edge of an InAlAs/AlGaAs multilayer has not been studied experimentally so far. In the following an x-ray technique is presented to identify the pseudomorphic strain *only within the CEO layer* of 100Å thickness and to measure it quantitatively. The main problem which had to be overcome is to separate the signal of the pseudomorphic strain within the CEO layer from the underlying InAlAs/AlGaAs superlattice. Surface sensitivity is achieved by choosing the scattering geometry of grazing incidence diffraction. In addition, longitudinal and transverse scans at two Bragg reflections [(002) and (220)] have to be measured to prove that the measured strain modulation clearly stems *only* from the CEO layer (see Fig. 5.9).

A first problem for the investigations arises from the tiny sample size (140µm x 7mm) and its exceptional orientation (on the cleaved edge). A way had to be found to mount the sample accurately in the centre of rotation of the diffractometer with the (1 $\bar{1}$ 0) CEO layer facing upwards (relative to the goniometer head used for the sample alignment). For this purpose a L-shaped sample holder as sketched in Figs. 5.11 and 5.12 was designed. In addition, one has to keep in mind that the total thickness of the sample and thus the width of the overgrown (1 $\bar{1}$ 0) edge is only about 140µm. An in-plane modulation of the GaAs lattice constant (in the [001] direction) due to the overgrown lattice mismatched multilayer is expected only within 2.5µm of the CEO surface, which corresponds to the thickness of the multilayer (see Fig. 5.10).

The proposed technique

To allow for a non-destructive, surface sensitive analysis of the strain profile in the CEO layer the measurements were performed by means of grazing incidence x-ray diffraction (GID). Using refraction of the incident and exit x-ray beam at the sample surface, the penetration depth of the beam into the sample can be reduced to the CEO layer thickness.

By carrying out measurements at the (002) and (220) surface Bragg reflection in both the transverse and longitudinal direction (see Fig. 5.9) it is possible to distinguish between compositional/morphological and purely strain-induced features. If compositional or morphological modulations are present, satellite peaks are expected in the direction of the modulation (i.e. along [001]) around any Bragg reflection [Holý98, Ulyanenkov99]. On the contrary, purely strain-induced oscillations in reciprocal space appear for the present sample with a modulation in the [001] direction only at (hkl) Bragg reflections with $l \neq 0$ [Holý98].

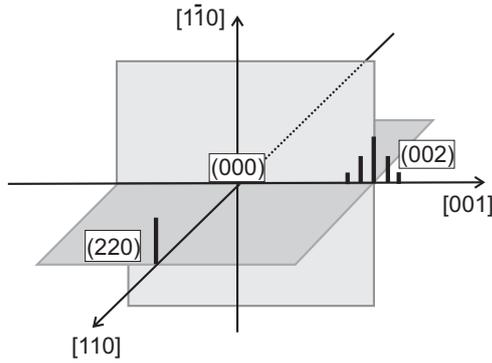


Figure 5.9: Sketch of the expected intensity distribution around the (002) and (220) Bragg reflections.

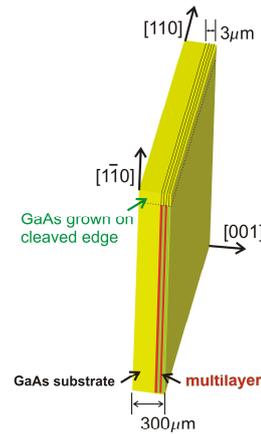


Figure 5.10: Schematic view of the investigated sample.

The period of the strain-induced satellites is inversely proportional to the multilayer period $D = 2\pi/\Delta q_{\text{long}}$, whereas the displacement Δq_{long} of the maximum of the envelope of the satellite reflections from the Bragg position Q_{Bragg} reveals the average residual strain inside the modulated volume $-\Delta a/a = \Delta q_{\text{long}}/Q_{\text{Bragg}}$ (a denotes the GaAs lattice parameter) [Holý98, Darowski98, Ulyanekov99].

Fig. 5.9 shows schematically the expected intensity distribution around the (002) and (220) Bragg reflections for the four investigated scans:

1. In a scan in the **longitudinal [001] direction** through the **(002) reflection** the strain profile in the direction of the superlattice modulations is probed. The evaluation of this scan using simulations based on a kinematical scattering model as well as finite-element calculations (see Chapter 5.3) reveals the strain profile within the CEO layer.
2. The **transverse scan** in the **[110] direction** through the **(002) reflection** parallel to the multilayer gives information about changes in composition or morphology along the multilayer. As the sample is invariant in this direction no intensity modulations in satellites are expected in this scan.
3. After turning the sample 90° around the $[1\bar{1}0]$ direction, the measurement at the **(220) reflection** in the **longitudinal [110] direction** is sensitive to lattice parameter changes along the [110] direction, i.e. along the wires. Again no intensity modulations in satellites are expected due to the lattice parameter invariance in this direction.
4. The **transverse measurement** in the **[001] direction** at the **(220) reflection** is sensitive to composition or surface morphology in the direction of the superlattice. Observed intensity modulations *cannot* be caused by strain because the momentum transfer Q is constant. Therefore, this scan can be used to determine whether satellites observed e.g. in a longitudinal scan at the (002) reflection are induced by strain and/or composition. For purely strain-induced modulations no satellites are expected in this transverse measurement. If satellites were observed in both the longitudinal scan at the (002) reflection

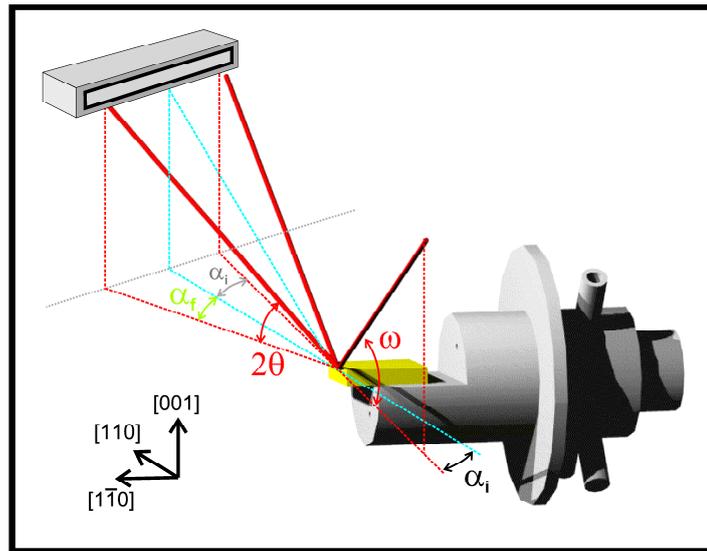


Figure 5.11: Experimental set-up - measurement at the (002) reflection. The intensity is measured with a one-dimensional position sensitive detector (PSD). See text for more details.

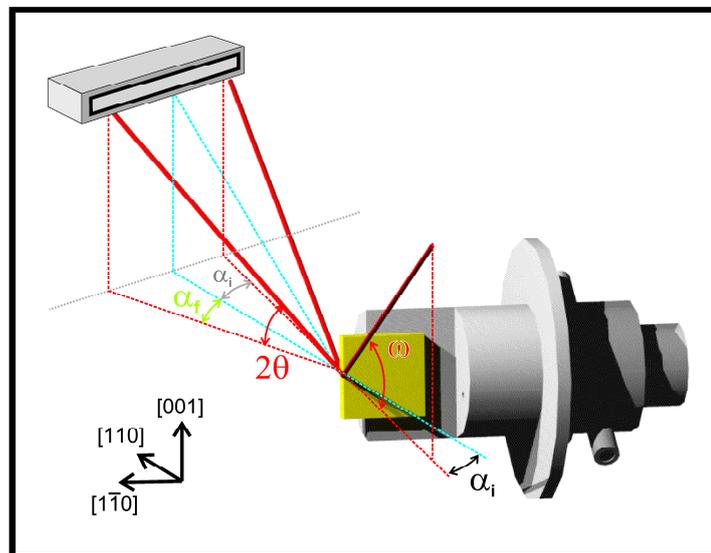


Figure 5.12: Experimental set-up - measurement at the (220) reflection.

and the transverse scan at the (220) reflection the modulations could be caused either by surface morphology or composition (multilayer). In the case of a flat surface (determined e.g. by AFM) one would have to assume interdiffusion of InAs or AlAs into the CEO layer, or a penetration depth of the GID measurements exceeding the 100Å CEO layer thickness, and therefore averaging over the strain in the CEO layer and in the multilayer.

A complication for the investigations arises from the size of the incident beam which is rather large compared to the sample surface on the cleaved edge. The width of the cleaved edge is about 140µm, the incident beam size defined by slits is 0.1mm x 0.1mm. Due to the grazing incidence angle ($\alpha_i = 0.4^\circ$) and the Bragg angle ($\omega = 17.74^\circ$) the incident beam always illuminates the (001) surface in addition to the investigated ($1\bar{1}0$) edge. For this reason not only the scattering of the cleaved edge in GID geometry, as previously described, is observed, but in addition scattering originating from the (001) surface (conventional out of-plane x-ray diffraction). This can be seen in Figs. 5.11 and 5.12. The sample is mounted on a sample holder, which was specially designed for the CEO geometry. The incident beam hits the cleaved edge under a grazing incidence angle α_i and a Bragg angle ω . In GID the beam is diffracted at an angle of 2θ . The exit angle α_f resolved diffracted intensity (containing information about the CEO layer) is measured with a one-dimensional position sensitive detector (PSD). This detector is mounted perpendicular to the CEO surface.

At the same time a second signal is detected. It stems from out of-plane diffraction at the (001) surface (containing information about the multilayer). Again the incident beam hits the surface under a Bragg angle ω and is diffracted at an angle of 2θ . This out of-plane scattering direction is inclined under an angle α_i relative to the cleaved edge, which plays no role for the out of-plane diffraction, but is important for the whole set-up: the signals of the two processes are close to each other along the exit angle (PSD). The maximum of the exit angle-resolved GID signal is at about $\alpha_f \approx \alpha_i + \alpha_c$. Therefore, the two signals lie $\alpha_i + \alpha_f \approx 1.2^\circ$ apart, assuming an typical incident angle of $\alpha_i = 0.4^\circ$ and a critical angle of about $\alpha_c \approx 0.4^\circ$. At this distance the tail of the strong scattering in out of-plane scattering direction can cover the intensity measured in GID which is about two orders of magnitude weaker.

In order to separate the two scattering paths for the measurement in particular at the (002) Bragg reflection the sample was mounted in a way that the x-ray beam always hits the sample coming from the side with the GaAs substrate (right hand side in Fig. 5.7). This allows to suppress any contribution originating from the multilayer due to the limited penetration depth of the incident beam, which then hardly reaches the buried multilayer, while the GID signal does, of course, not suffer from this absorption effect.

Fig. 5.12 shows the set-up for the investigation of the (220) Bragg reflection. The sample is turned 90° around the $[1\bar{1}0]$ direction relative to the alignment at the (002) reflection. In this case the out of-plane diffraction is measured in transmission, which strongly decreases the intensity of superlattice peaks.

All measurements have been performed at the beamline ID1 of the European Synchrotron Radiation Facility at an energy of 7.2keV.

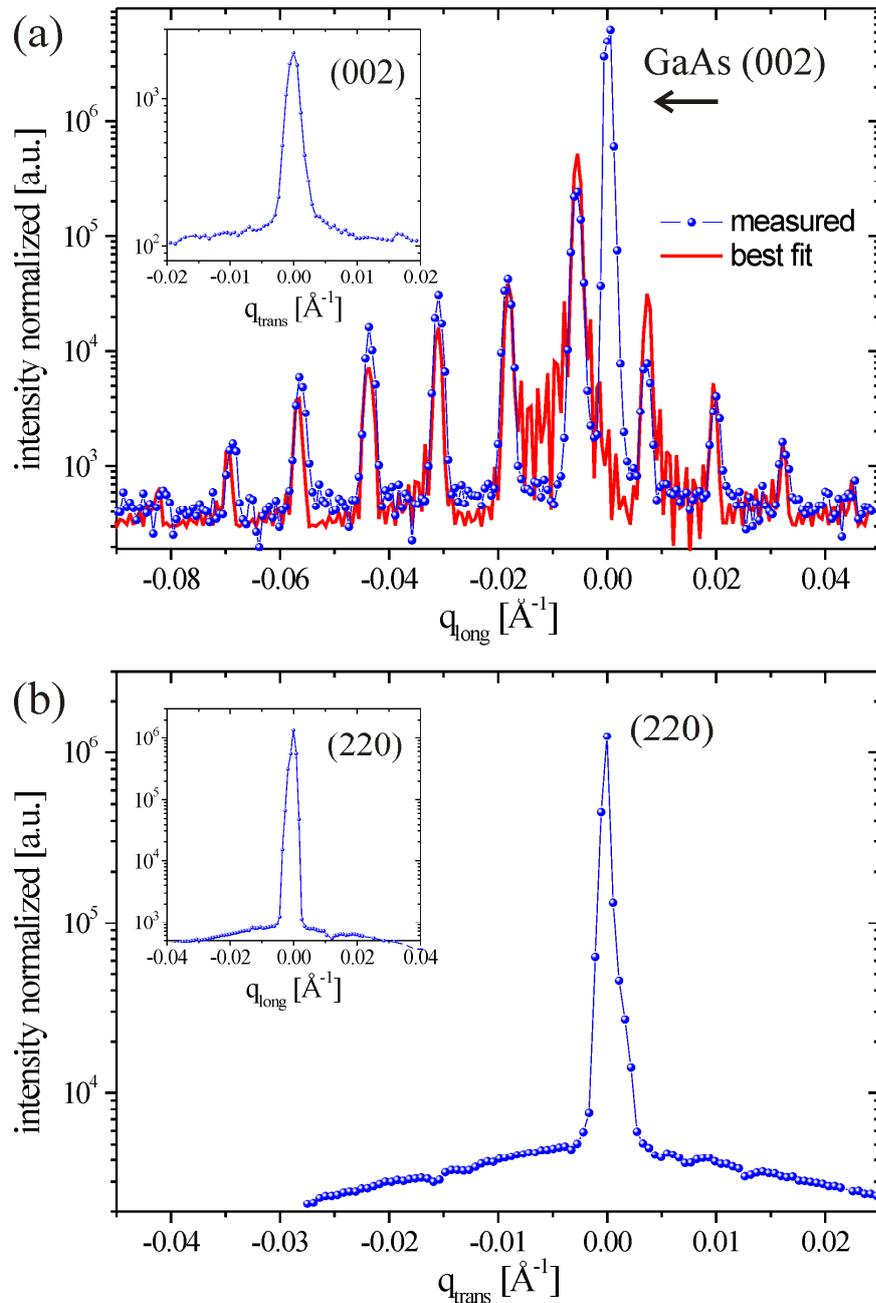


Figure 5.13: GID measurements of the cleaved edge. (a) Strain sensitive longitudinal scan at the (002) Bragg reflection. The fit was calculated using a displacement field based on finite-element simulations. The GaAs (002) substrate peak was not simulated. The inset shows a transverse scan at the (002) Bragg reflection. (b) Transverse scan (sensitive to composition and/or morphology) at the (220) Bragg reflection: no modulation is observed. The inset shows a longitudinal scan at the (220) Bragg reflection.

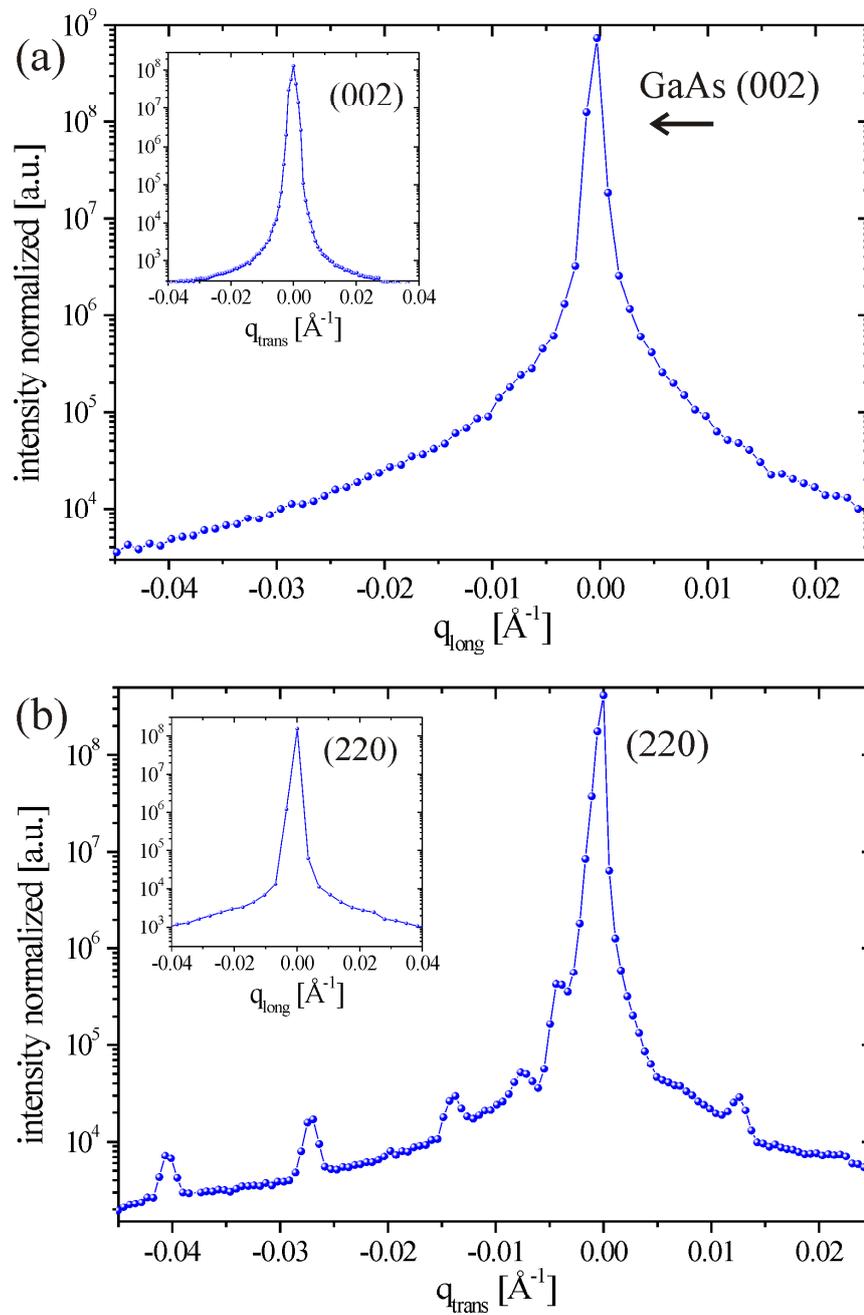


Figure 5.14: Out of-plane XRD measurements of the (001) surface. (a) Strain sensitive longitudinal scan at the (002) Bragg reflection. The inset shows a transverse scan at the (002) Bragg reflection. (b) Transverse scan (sensitive to composition and/or morphology) at the (220) Bragg reflection. The inset shows a longitudinal scan at the (220) Bragg reflection. The observed modulations are caused by the InAlAs/AlGaAs superlattice.

The measurements at the (002) and (220) Bragg reflection

Fig. 5.13 shows the measurements performed at the (002) and (220) Bragg reflections in grazing incidence geometry. In all figures the integrated intensity along the position sensitive detector used in the experiment is plotted. As can be seen from Fig. 5.9 longitudinal scans at the (002) and transverse scans at the (220) reflection measure perpendicular to the strain modulated wires in the overgrown cleaved edge. These two measurements are shown in Fig. 5.13 (a) and (b), respectively. The inset shows in each case the other scan direction (transverse at the (002) and longitudinal at the (220) reflection). In both cases (insets) the q vector of the measurement goes along the layers of the superlattice in [110] direction. As expected no satellite peaks are observed due to the invariance of the sample in this direction.

More interesting are the scans shown in full size: the longitudinal scan in [001] direction through the (002) reflection probes the strain profile in the direction of the superlattice modulations. From the displacement of the maximum of the envelope of the satellite reflections from the Bragg position an average residual strain inside the modulated volume of about $-\Delta q_{\text{long}}/Q_{\text{Bragg}} = \Delta a/a \approx (0.8 \pm 0.1)\%$ can already be determined. The lattice mismatch between the nominally grown $\text{In}_{0.1}\text{Al}_{0.9}\text{As}$ and GaAs is 0.72%. The period of the modulation of $D = (490 \pm 4)\text{\AA}$ reflects very well the nominal values of the MBE growth. A more quantitative analysis of the strain profile based on a kinematical scattering model and finite-element calculations is presented in the following chapter.

The transverse measurement in [001] direction at the (220) reflection (see Fig. 5.13(b)) would reveal changes in composition or surface morphology in the direction of the superlattice. The measurement does not show any satellites, thus excluding any periodic modulation in the surface morphology or in composition which could be caused by interdiffusion during the

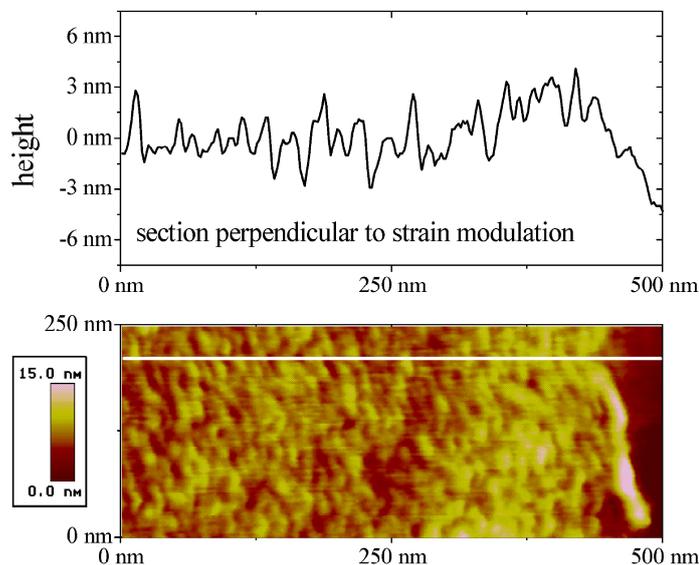


Figure 5.15: AFM image of the overgrown cleaved edge on top of the strained $\text{InAlAs}/\text{AlGaAs}$ superlattice. The white line marks where the cut shown in the upper part of the figure was taken. The measurement was taken as close as possible to the border of the CEO surface.

CEO. In addition, it proves that only the overgrown cleaved edge is investigated and not the underlying superlattice. If the x-ray beam could penetrate to this superlattice the material contrast between InAlAs and AlGaAs would cause satellites.

Fig. 5.14 shows the same measurements as before for the out of-plane Bragg diffracted beam (containing now information about the multilayer). Again the measurements presented in the two insets, measuring along the layers of the superlattice, do not show any interesting features. Due to the set-up with the x-ray beam hitting the sample from the side of the GaAs substrate no superlattice modulations are observed in a longitudinal scan at the (002) reflection [see Fig. 5.14(a)]. Fig. 5.14(b) shows the scan in the transverse direction at the (220) reflection. This measurement is sensitive to composition and/or morphology. The observed satellite peaks prove that the material contrast between InAlAs and AlGaAs causes modulations which were not observed in the transverse scan at the (220) Bragg reflection in GID geometry. Hence, it becomes clear that in GID only the thin CEO layer is probed and not the AlGaAs/InAlAs multilayer beneath.

Ex-situ atomic force microscopy (AFM) measurements (see Fig. 5.15) confirm the absence of morphological oscillations at the sample surface. All AFM measurements show a flat surface with an average roughness of about (2 ± 1) nm.

Exit angle-resolved data

Up to now only the integrated intensity of the measurements with the PSD mounted perpendicular to the sample surface was presented. Fig. 5.16 shows the originally measured α_f resolved data in a $q_{\text{long}} - q_z$ map at the (002) Bragg reflection in GID geometry. The map reveals depth-

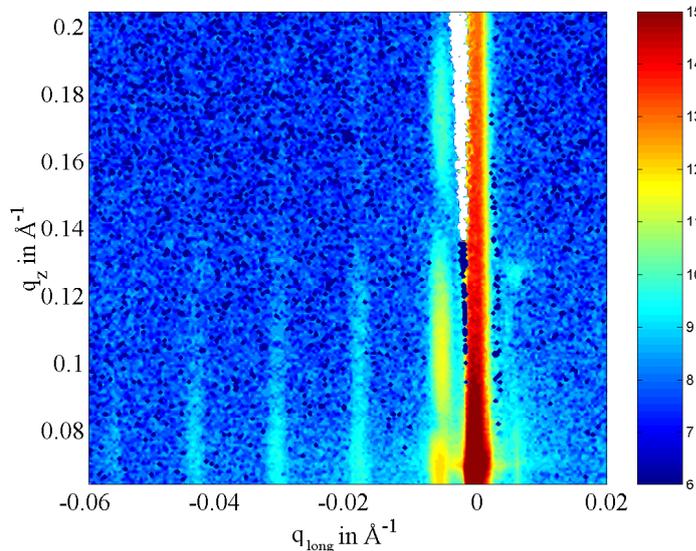


Figure 5.16: $q_{\text{long}} - q_z$ map at the (002) Bragg reflection in GID geometry. The corresponding plot showing the integrated intensity along q_z is shown in Fig. 5.13(a). The strain-induced satellites show thickness oscillations in q_z direction, caused by the strained CEO layer.

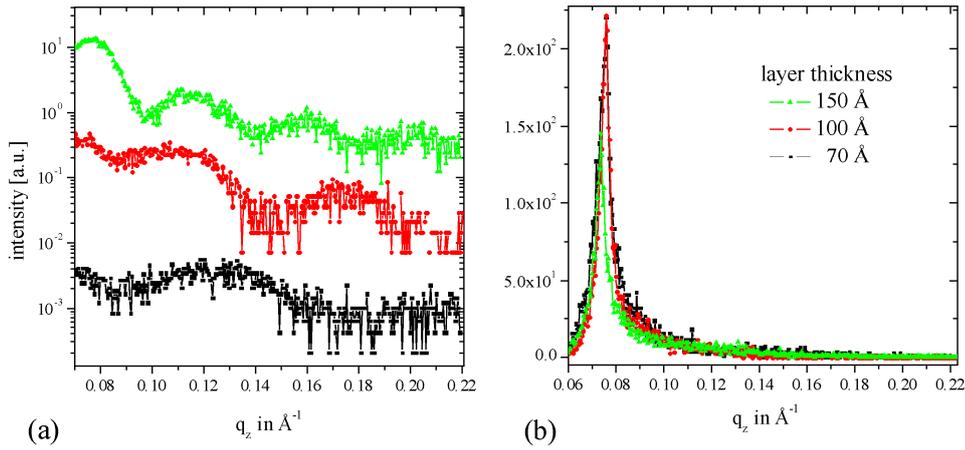


Figure 5.17: Slices along the q_z direction in Fig. 5.16 through (a) the first satellite and (b) the GaAs (002) peak for three different samples with varying thickness of the CEO layer.

resolved information on the sample. It can be clearly observed that the strain-induced satellites show thickness oscillations in q_z direction. These are caused by the strained CEO layer on top of the InAlAs/AlGaAs superlattice. On the other hand, the GaAs (002) peak doesn't show any oscillations in q_z direction. This signal comes from the large area of the sample where an unstrained CEO GaAs layer is grown on the cleaved GaAs (001) substrate. Fig. 5.17 (a) and (b) show slices along the q_z direction at the position of the first satellite, and the GaAs Bragg peak, respectively. Measurements for three different samples are presented. The nominal value of the thickness of the overgrown layer varies from 70 \AA , and 100 \AA , to 150 \AA . From the period of the observed oscillations the thickness of the strained layer is determined to be 71 \AA , 101 \AA or 152 \AA , respectively. This is in good agreement with the nominal growth parameters.

5.3 Evaluation and discussion

For a more detailed analysis, the CEO structure was simulated by means of the finite-element method (FEM). This gives information about the expected lateral and vertical strain relaxation in the overgrown layer. The strain-induced satellites shown in Fig. 5.13(a) were simulated by a kinematical scattering model based on a linear chain of atoms. The starting parameters of the atomic displacements were chosen according to the FEM simulation and refined in a fitting procedure.

Finite-element simulation

The strain distribution and the displacement field of the sample structure close to the cleaved edge was calculated by means of the finite-element method. One period of the multilayer with the overgrown GaAs layer was simulated as indicated in Figs. 5.18 to 5.21. Interdiffusion between the different materials is not taken into account, as it is of minor importance for the strain

distribution in the GaAs capping layer. For the model the nominal growth parameters have been used. The lattice constants and elastic constants of InAs, AlAs, and GaAs are summarised in Tab. 5.1. The properties of the alloys are obtained by linear interpolation between these values.

	InAs	AlAs	GaAs
lattice const.	6.0584Å	5.6614Å	5.65338Å
$c_{11} = c_{22} = c_{33}$	83.29GPa	120.2GPa	119GPa
$c_{12} = c_{13} = c_{23}$	45.26GPa	57.0GPa	53.8GPa
$c_{44} = c_{55} = c_{66}$	39.59GPa	58.9GPa	59.5GPa

Table 5.1: Lattice constants and elastic constants of InAs, AlAs, and GaAs used for the simulations.

However, in the present case the tensor of the elastic constants cannot directly be used in the FEM software as the CEO surface normal (z direction) points in $[\bar{1}\bar{1}0]$ direction, whereas the tensor is defined relative to the (001) surface. Therefore, a coordinate transformation of the tensor has to be carried out. For this the compressed indices (Voigt's notation) of the elastic constants c_{ij} (see chapter 2.3.1) can no longer be used. Rather, the transformation of the tensor c_{ijkl} of the elastic constants has to be considered by

$$\tilde{c}_{mnop} = \sum_{i=1}^3 \sum_{j=1}^3 \sum_{k=1}^3 \sum_{l=1}^3 a_{mi} a_{nj} a_{ok} a_{pl} c_{ijkl} \quad (5.1)$$

with the rotation matrix \mathbf{a} . For the described geometry a rotation around the x axis ([001] direction) has to be performed:

$$\mathbf{a} = \begin{pmatrix} 1 & 0 & 0 \\ 0 & \frac{\sqrt{2}}{2} & \frac{\sqrt{2}}{2} \\ 0 & \frac{\sqrt{2}}{2} & -\frac{\sqrt{2}}{2} \end{pmatrix} \quad (5.2)$$

The extension of the multilayer in the $[\bar{1}\bar{1}0]$ direction has been chosen large enough (200nm) so that a further increase does not influence the calculated displacement field. In the [001] direction periodic boundary conditions are assumed. As described in chapter 2.3.3 the calculation was done using the commercial program package PATRAN/NASTRAN. The results of the simulations are shown in Figs. 5.18 to 5.21.

Figs. 5.18 and 5.19 show the strain components ε_{xx} and ε_{zz} in x and z direction for the entire structure. The strain is given relative to the relaxed GaAs lattice. Close to the interface to the multilayer pseudomorphic growth is observed. Due to the significantly larger lattice parameter of InAlAs compared to GaAs (0.8%) *tensile strain above the InAlAs layer* is induced in the overgrown layer. Under the influence of this strain the GaAs lattice on top of AlGaAs is compressively strained ($\approx -0.1\%$). For that reason, in vertical direction the lattice is accordingly compressed on top of InAlAs and expanded above AlGaAs. Towards the surface the lattice

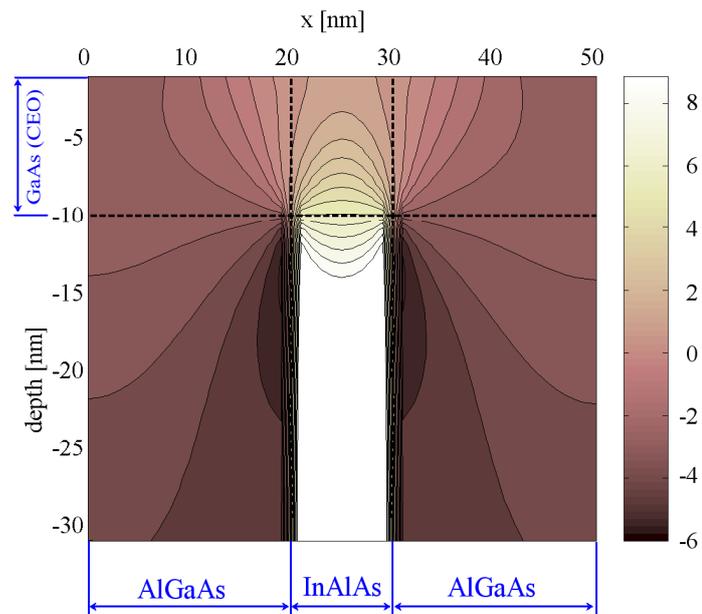


Figure 5.18: In-plane strain component ε_{xx} calculated by FEM. The colour scale is given in units of 10^{-3} .

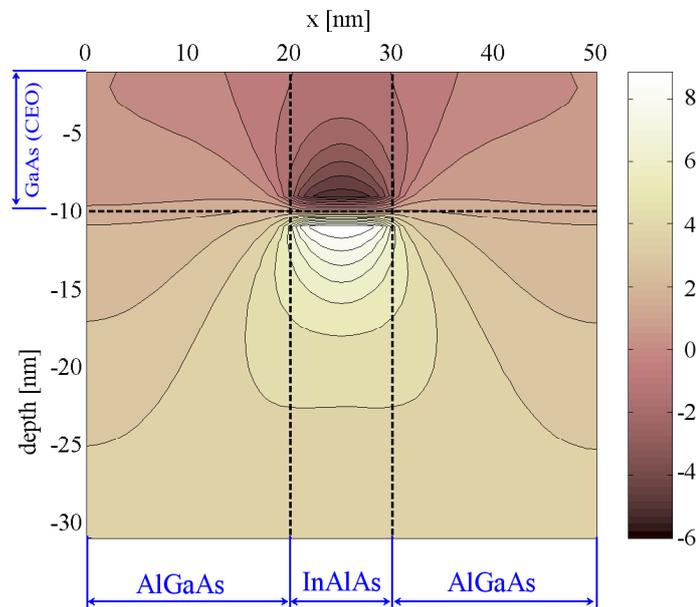


Figure 5.19: Strain component ε_{zz} perpendicular to the CEO surface calculated by FEM. The colour scale is given in units of 10^{-3} .

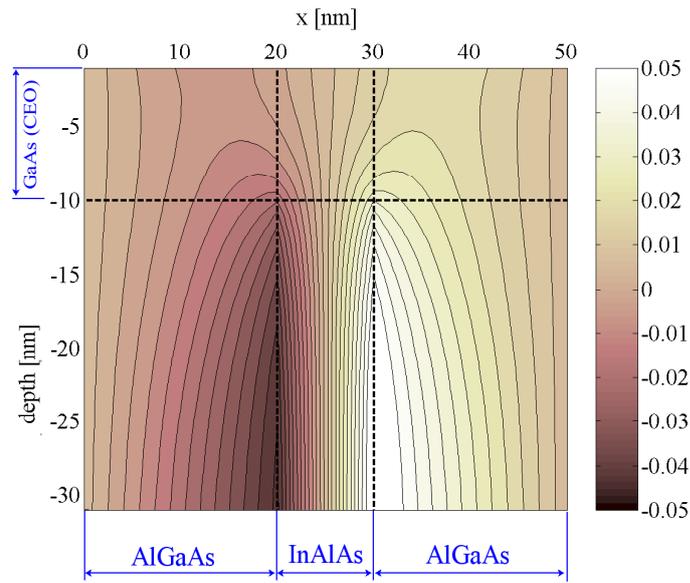


Figure 5.20: In-plane displacement field u_x calculated by FEM. The colour scale is given in units of [nm].

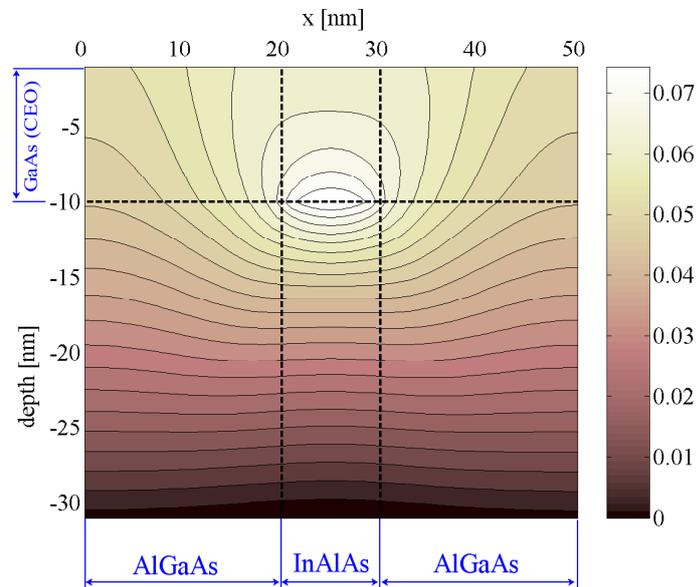


Figure 5.21: Displacement field u_z perpendicular to the CEO surface calculated by FEM. The colour scale is given in units of [nm].

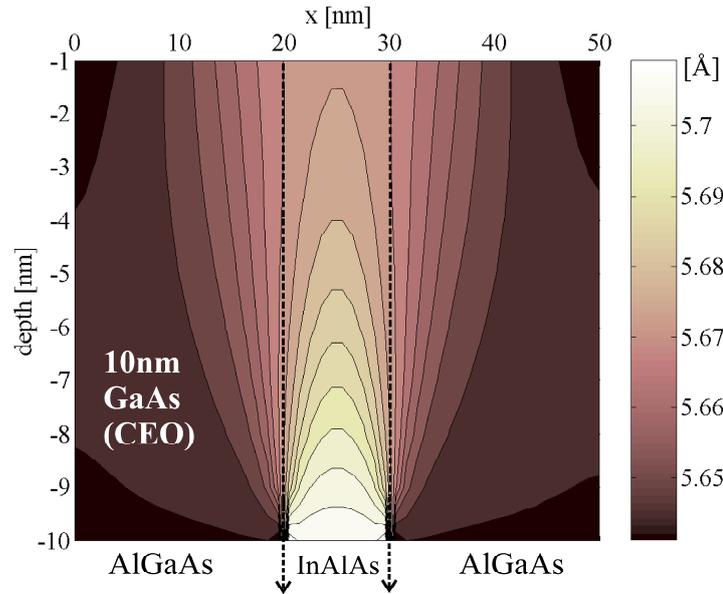


Figure 5.22: FEM calculation of the [001] component of the GaAs lattice parameter distribution in the CEO layer. The underlying multilayer material is marked at the bottom of the graph.

relaxes in both directions. In Figs. 5.20 and 5.21 the displacement field u_x and u_z shows basically the same information. The lateral displacement field is symmetric around the centre of the InAlAs layer. The zero value for the relative vertical displacement field was set to a depth of 30nm.

Fig. 5.22 shows the [001] in-plane component of the GaAs *lattice parameter distribution* within the CEO layer. This simulation based on the nominal growth parameters is used as an input parameter for the kinematical scattering model described in the following section. On top of the InAlAs layer the GaAs lattice is expanded to about 5.7Å. Due to this the GaAs lattice on top of AlGaAs is compressed to values even below the lattice constant of relaxed GaAs (5.653Å). Towards the surface of the CEO layer the lattice relaxes, which leads to a broadening of the lattice parameter distribution in lateral direction and a decrease of the maximum strain.

Fit using a kinematical scattering model

For the simulation of the strain sensitive longitudinal scan at the (002) Bragg reflection [see Fig. 5.13(a)] a kinematical scattering model has been developed. As the GID technique is only sensitive to the in-plane strain the crystal lattice is approximated by a one-dimensional linear chain of Ga and As atoms.

In a simple model two strain states A and B above InAlAs and AlGaAs are assumed (see Fig. 5.23). In strain state A (or B) the lattice constant of one Ga-As pair is denoted with a (or b). The thickness of one layer is given by $D_A = N_A \cdot a \leq 100\text{Å}$ (or $D_B = N_B \cdot b \leq 400\text{Å}$, respectively).

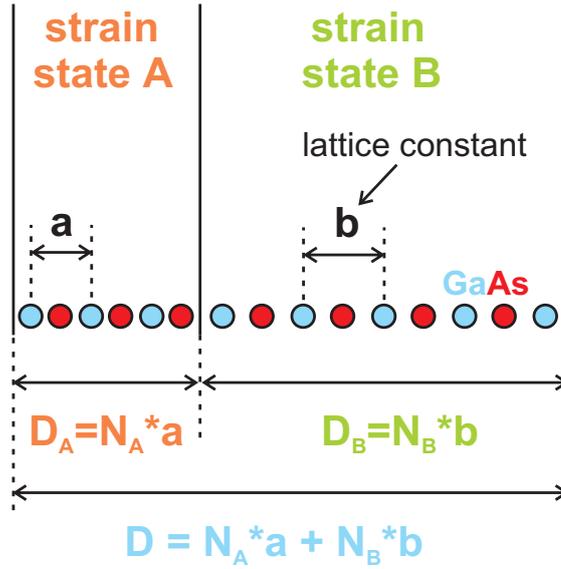


Figure 5.23: Sketch of a linear chain of atoms with two strain states A and B above InAlAs and AlGaAs, respectively: a simple model for the simulation of strain modulations.

Thus, the structure factor F of a Ga-As pair taking into account the phase shift of the two atoms by half a lattice constant yields

$$F_A = f_{Ga} + \exp\left(iQ\frac{a}{2}\right) f_{As} \quad (5.3)$$

$$F_B = f_{Ga} + \exp\left(iQ\frac{b}{2}\right) f_{As} \quad (5.4)$$

$f_{Ga} = 24.82$ and $f_{As} = 26.51$ are the atomic form factors at the (002) reflection.

The scattering amplitude \mathcal{A} of N_A (or N_B) Ga-As pairs is

$$\mathcal{A}_A(Q) = \sum_{n=1}^{N_A} F_A \cdot \exp(iQna) \quad (5.5)$$

$$\mathcal{A}_B(Q) = \sum_{n=1}^{N_B} F_B \cdot \exp(iQnb) \quad (5.6)$$

taking into account the phase shift of one lattice constant a (or b) per repetition n .

The two scattering amplitudes $\mathcal{A}_A(Q)$ and $\mathcal{A}_B(Q)$ have a phase shift of $\exp(iQD_A)$. Therefore, the scattering amplitude of one bilayer of the superlattice is

$$\mathcal{A}(Q) = \sum_{n=1}^{N_A} F_A \cdot \exp(iQna) + \exp(iQD_A) \sum_{n=1}^{N_B} F_B \cdot \exp(iQnb) \quad (5.7)$$

The whole multilayer structure with $Z = 50$ repetitions can be described in real space as the *convolution* of a grating of δ -functions with one bilayer. Its Fourier transform in reciprocal space is the *product* of the grating interference function and the scattering amplitude of one bilayer according to the convolution theorem of the Fourier transform [Bronstein].

In other words, the observed scattering signal is determined by the envelope of the bilayer diffraction modulated with the interference peaks of the grating diffraction function.

The grating interference function is

$$\frac{\exp(iZDQ) - 1}{\exp(iDQ) - 1} \quad (5.8)$$

with $D = D_A + D_B$ being the thickness of one bilayer and Z the total number of repetitions of the bilayer.

Finally, the scattered intensity is calculated as the absolute square of the scattering amplitude

$$I(Q) = \left| \frac{\exp(iZDQ) - 1}{\exp(iDQ) - 1} \left[\sum_{n=1}^{N_A} F_A \cdot \exp(iQna) + \exp(iQD_A) \sum_{n=1}^{N_B} F_B \cdot \exp(iQnb) \right] \right|^2 \quad (5.9)$$

The model used for the *fitting of the measured longitudinal scan* in Fig. 5.13(a) is more sophisticated. It does not only use two strain states with constant lattice parameters but allows for a *continuous change of the lateral lattice constant* always taking care of the correct phase shift of the atoms. In addition, the simulations of different strain profiles were incoherently superposed to account for the relaxation of the strain distribution towards the sample surface. The lateral lattice parameter profiles as a function of depth were chosen according to the FEM calculations based on the nominal growth parameters (see Fig. 5.22) and refined in the subsequent fitting procedure. The following parameters have been varied during this process:

- the thickness of the MBE grown InAlAs and AlGaAs layers,
- the maximum and minimum GaAs lattice parameter in the CEO layer (close to the interface of the multilayer), and
- the gradient of the lateral lattice parameter change as a function of depth.

The GaAs (002) peak originating from the unstrained part of the CEO layer was not simulated.

The thickness of one InAlAs/AlGaAs bilayer strongly influences the position of the observed satellite peaks, which allows for an accurate determination of this size. The ratio between the two layer thicknesses as well as the other fit parameters determine the intensity of the satellites.

The best agreement between simulation and experiment has been obtained for a multilayer thickness of 104Å and 386Å for the InAlAs and AlGaAs layers, respectively. The GaAs lattice parameter varies between 5.649Å and 5.710Å in the probed CEO layer. A compression of the

GaAs lattice even below the lattice parameter of relaxed GaAs (5.653\AA) occurs above AlGaAs. The strongest tensile strain is observed on top of the InAlAs layers. These results are in good agreement with the nominal growth parameters. The best fit is shown in Fig. 5.13(a) as a red solid curve.

Summary

The $(1\bar{1}0)$ oriented cleaved edge of a pseudomorphically strained $\text{In}_{0.1}\text{Al}_{0.9}\text{As}/\text{Al}_{0.33}\text{Ga}_{0.67}\text{As}$ multilayer [grown in (001) direction] was capped with a homogeneous GaAs layer of 10nm thickness. The buried superlattice induces a periodic strain modulation in the overgrown layer which is used for the controlled formation of quantum wires. Thereby, the charge carriers are laterally confined to one dimension .

The technique of grazing incidence x-ray diffraction is ideally suited for the quantitative characterisation of the strained capping layer. The strain modulation due to the overgrown superlattice occurs only within $3\mu\text{m}$ of the total wafer thickness of $150\mu\text{m}$. The average lattice expansion in this narrow stripe of the CEO layer amounts to $\Delta a/a \approx (0.8 \pm 0.1)\%$.

Performing longitudinal and transversal measurements at the (002) and (220) Bragg reflection, the GID technique allows for a clear separation of the strain modulation in the cap layer and the superlattice underneath. Moreover it can be proved that the strain modulation in the CEO layer is not of compositional origin but purely elastic. No surface ripples are present and interdiffusion of In into the CEO layer can be excluded (at the growth temperature of 430°C).

For a quantitative analysis, the strain distribution in the GaAs cover layer was simulated by means of the finite-element method. The depth dependent lattice parameter profile is used as an input parameter for a kinematic scattering model based on a linear chain of atoms to fit the strain sensitive intensity distribution in the longitudinal scan direction.

The experimentally determined strain distribution within the overgrown layer is important for the design and the simulation of devices using strain induced QWRs produced by CEO. Several methods (see [Sabathil02]) have been developed in order to simulate the electronic structure of 3D nanostructures (e.g. 8-band-k.p-models implemented in the program nextnano³ developed at the Walter Schottky Institute, Technical University in Munich [Sabathil02, Hackenbuchner02, nextnano]). All these methods have in common that in a first step the strain distribution in the devices has to be determined. The presented x-ray technique can help to refine these calculations.

Moreover, knowledge of the strain state at the surface of the CEO layer is important as it forms a template for the self-organised ordering of InAs quantum dots [Arai97a, Arai97b, Usami98]. This represents an alternative technique to induced ordering of quantum dots by prepatterned substrates [Kim98, Kim99, Schmidt00, Kitajima01, Schmidt02] or by using highly indexed or tilted substrate surfaces [Zhu99].

Chapter 6

General conclusions and outlook

The main purpose of this thesis was the development and application of novel x-ray scattering methods for the investigation of surface near semiconductor heterostructures with nanometric size dimensions. The generally weak scattering signal mandates the use of highly brilliant x-ray sources like the ESRF in Grenoble, France.

For the characterisation of *free-standing* quantum dots a novel approach has been developed by combining the *surface sensitive technique of grazing incidence diffraction* (GID), the *anomalous dispersion of the atomic scattering factor* close to the absorption edge of a suitable element, and the properties of *superstructure reflections in a binary compound* (like GaAs or InAs).

The analysis is done using the model of *iso-strain scattering* (ISS) which has already been successfully applied for the investigation of free-standing InGaAs quantum dots by measuring at a *fixed* x-ray energy [Kegel01]. Using the tunability of the energy of synchrotron radiation, contrast variation by anomalous diffraction at superstructure reflections allows for an accurate determination of the strain *and* composition profile of *free-standing quantum dots*.

Moreover, the method has the potential to determine the composition of *wetting layers* which has not been exploited so far.

However, it has been demonstrated that structures which do *not* exhibit a *monotonic lattice parameter relaxation with increasing height* exceed the capabilities of the iso-strain approximation and the contrast variation technique which relies on ISS. Especially buried structures, but also e.g. ring-like nanostructures (formed by partial overgrowth of quantum dots) can no longer be treated by this direct analysis method.

Therefore, the evaluation of the scattering data of (partly) buried structures needs a new approach, in which the *finite element method* (FEM) is applied to calculate the displacement field in and around the nanostructures. Using the lateral displacement field in *extensive case studies* for the simulation of GID measurements, the shape, strain, and composition profile of (partly) buried structures can be determined.

For a further element specific analysis of partly buried structures, *anomalous GISAXS* seems to be a promising tool. Unlike anomalous GID, the technique is not strain sensitive and, therefore, the restrictions of the iso-strain model do not apply.

The third part of the thesis deals with an *overgrowth phenomenon on a cleaved edge* (CEO). The investigated CEO layer with a thickness of 10nm is strain modulated in a narrow stripe

of $3\mu\text{m}$ width due to a superlattice of that width buried under the cap layer. For the first time, x-ray techniques, in particular grazing incidence diffraction has been applied to measure the strain modulations in such an overgrown edge. It has been demonstrated that using *finite-element calculations* and a *kinematical scattering model* the measured strain profile can be fitted accurately. Moreover, it can be proved that the strain modulation in the cap layer is purely elastic and not of compositional origin.

The wealth of *detailed structural results* are discussed in the corresponding chapters separately.

Appendix A

Useful formulae

This appendix deals with the use of a linear position sensitive detector (PSD) in the grazing incidence diffraction (GID) geometry.

α_f determination using a PSD on a 4+2 axes diffractometer

For the following a typical GID set-up is assumed (see Fig. 2.13). The sample surface is aligned vertically. The Bragg angle of the lattice planes and the scattering angle are defined by ϕ and δ , respectively. The grazing incident angle α_i is set by μ around the vertical axis. For α_f resolved measurements a position sensitive detector is used which is mounted horizontally on the detector arm. The angular variation along the PSD is considered as a separate degree of freedom β perpendicular to the detector arm. Its zero position is defined by the direct beam with $\nu = 0^\circ$.

Due to the 4+2 axes diffractometer geometry the exit angle α_f relative to the sample surface depends not only on β but also on the position of the detector arm (ν and δ). Only for $\delta = 0^\circ$ the direction β points approximately into the same direction as a movement around the ν axis.

The general case has to be calculated using three-dimensional rotation matrices. I. Kegel has shown how the exit angle α_f is determined as a function of all these rotations [Kegel00b]. Unfortunately, the important final formula contains a typing error. The correct equation using the notation of the 4+2 diffractometer at ID1 is:

$$\begin{aligned} \cos \alpha_f(\mu, \nu, \delta, \beta) &= \cos \alpha_f(\mu, \nu, \delta, \beta) = \\ &= \sqrt{\cos^2 \beta \sin^2 \delta + [\cos \beta \cos \delta \cos(\nu - \mu) - \sin \mu \sin(\nu - \mu)]^2} \end{aligned} \quad (\text{A.1})$$

Generally α_f depends on ν , μ , δ , and β . Fortunately the formula can be simplified dramatically by always using $\mu = \nu$.

$$\cos \alpha_f(\mu = \nu) = \sqrt{\cos^2 \beta \sin^2 \delta + [\cos \beta \cos \delta]^2} = \cos \beta \quad (\text{A.2})$$

$$\Rightarrow \alpha_f = \beta \quad (\text{A.3})$$

If the $\mu = \nu$ condition is not fulfilled, the zero position on the PSD “moves” while increasing

the detector angle del . Therefore, the condition $mu = nu$ should always be fulfilled to allow for an accurate and easy determination of the exit angle α_f and a constant accessible maximum range in the exit angle.

In the experimental set-up, the condition $mu = nu$ is fulfilled if the axes of phi (sample) and del (detector) coincide. For shifting the zero position in the PSD (β) it is possible to mechanically move the mounting of the detector perpendicular to the detector arm. However, nu must not be used for this adjustment.

Shift of the Bragg position along α_f in grazing incidence diffraction

Another peculiarity arises using a PSD for α_f resolved radial scans in the GID geometry. Fig. A.1(a) shows a typical mapping around the (002) Bragg reflection of a sample with quantum dots on its surface at an energy of 11.856keV. The Bragg angle is $\theta_{\text{Bragg}} = 10.656^\circ$. For $\theta > \theta_{\text{Bragg}}$, very close to the Bragg position, a shift of the maximum intensity position along the exit angle α_f versus the radial position θ is observed. This effect occurs since the α_f resolution element of the PSD describes a curved line in reciprocal space. Therefore, the PSD cuts the crystal truncation rod for increasing θ at increasing positions in α_f .

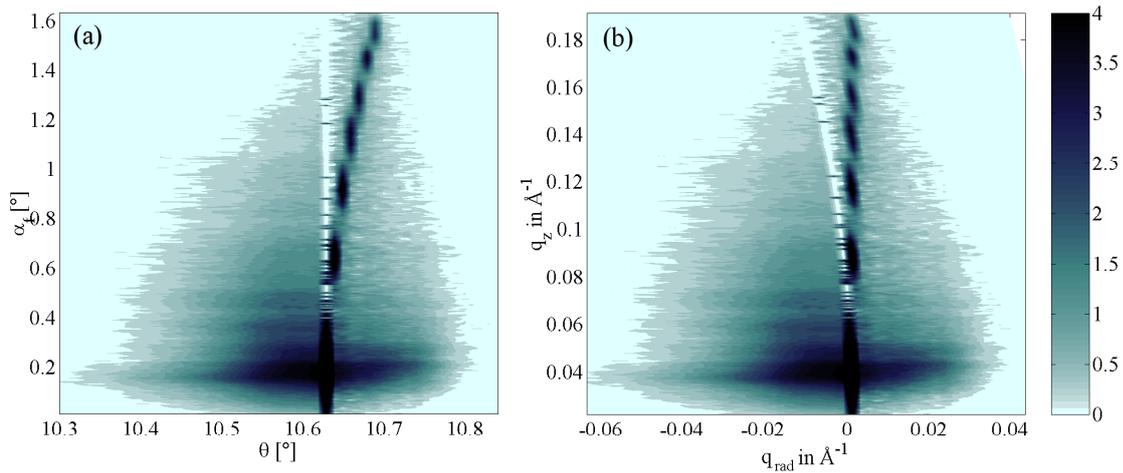


Figure A.1: Shift of the Bragg position along α_f for $\theta > \theta_{\text{Bragg}}$ (a). Fig. (b) shows the corrected data in Q -space.

H. Rhan et al. [Rhan96] have calculated the angular position α_f of the crystal truncation rod as a function of α_i and $\Delta\theta = \theta - \theta_{\text{Bragg}}$.

$$\Delta\theta(\alpha_f) = \theta_{\text{Bragg}} - \arcsin \frac{\sin^2 \alpha_f - \sin^2 \alpha_i + 4 \sin^2 \theta_{\text{Bragg}}}{4 \cos \alpha_i \sin \theta_{\text{Bragg}}} \quad (\text{A.4})$$

Eq. A.4 gives the exit angle-dependent deviation of the measured Bragg position from θ_{Bragg} . It can be used to correct the measured data according to

$$\theta_{\text{corrected}}(\alpha_f) = \theta_{\text{measured}}(\alpha_f) - \Delta\theta(\alpha_f) \quad (\text{A.5})$$

Fig. A.1(b) shows the corrected data. Now the crystal truncation rod is at $q_{\text{rad}} = 0$ for all q_z values.

Appendix B

List of tables

2.1	Theoretical contrast factors between InAs and GaAs scattering as a function of energy.	12
3.1	Growth parameters of the investigated InGaAs quantum dot samples.	38
4.1	Growth parameters of the investigated InAs quantum dot samples (quantum ring series).	59
4.2	Parameters used for the best simulation of the GISAXS data.	67
4.3	Parameters for selected FEM simulations of quantum rings.	73
5.1	Lattice constants and elastic constants of InAs, AlAs, and GaAs.	102

Appendix C

List of figures

1.1	Electronic density of states when the dimensionality is varied from 3D to 0D.	1
1.2	Band gaps and lattice constants of selected semiconductors at 300K.	2
1.3	Schematic illustration of strain relief in Stranski-Krastanov growth	3
2.1	Zinc-blende structure of GaAs.	8
2.2	Calculated (200) intensity for GaAs and InAs as a function of the x-ray energy.	11
2.3	Calculation of the material composition.	13
2.4	Comparison of radial measurements at the (200) and (400) reflection.	14
2.5	The experimental hall of the ESRF.	15
2.6	View of the storage ring.	16
2.7	The 4+2 circle diffractometer at ID1.	17
2.8	Picture of the GID set-up with analyser.	17
2.9	Sample Environment.	17
2.10	Set-up for small angle scattering.	18
2.11	Functional principle of the position sensitive detector.	19
2.12	Sketch of the XRD geometry.	19
2.13	Sketch of the GID geometry.	21
2.14	GID geometry using an analyser crystal.	22
2.15	Parafocusing geometry of a mosaic crystal.	23
2.16	Inelastic scattering background.	23
2.17	Sketch of the GISAXS geometry.	24
2.18	User interface of the FEM preprocessor PATRAN.	31

2.19	FEM model of a buried quantum dot in 2D.	32
2.20	FEM model extruded to a 45° wedge.	33
2.21	FEM model filled with an appropriate mesh.	33
2.22	Displacement field u_x calculated for the 45° wedge.	34
2.23	Displacement field u_x and strain ϵ_{xx} calculated for the x - z plane.	35
3.1	AFM image of a free-standing single layer of InGaAs QDs.	39
3.2	AFM image of a single layer of InGaAs QDs overgrown by 100Å GaAs.	39
3.3	AFM image of the sample with a double layer of InGaAs QDs separated by a spacer layer of 70Å GaAs.	40
3.4	AFM image of the sample with a double layer of InGaAs QDs separated by a spacer layer of 130Å GaAs.	40
3.5	Elastic energy density above buried InGaAs QDs.	41
3.6	Investigation of free-standing InGaAs QDs by radial scans around the (200) reflection at 11.856keV and 12.380keV.	43
3.7	InAs concentration in a single layer of free-standing InGaAs QDs.	44
3.8	Best fits for angular measurements performed on the sample with a single layer of free-standing QDs.	46
3.9	Cross-sectional profile through a QD as determined from AFM micrographs.	46
3.10	Composition profile of free-standing InGaAs QDs as a function of the height in the dots.	46
3.11	Lattice parameter profile of free-standing InGaAs QDs as a function of the height in the dots.	46
3.12	InAs concentration as a function of the lattice mismatch with respect to GaAs.	47
3.13	InAs concentration in the InGaAs QD double structure (70Å spacer).	48
3.14	InAs concentration in a layer of buried InGaAs QDs.	48
3.15	Radial scans at the (200) Bragg reflection at an energy of 11.856keV.	49
3.16	Radial scan at the (200) Bragg reflection at an energy of 12.380keV.	49
3.17	FEM simulation of the in-plane strain ϵ_{xx} of a free-standing InGaAs QD.	50
3.18	FEM simulation of the in-plane strain ϵ_{xx} of a buried InGaAs QD.	50
3.19	FEM simulation of the in-plane strain ϵ_{xx} of a double layer of InGaAs QDs.	50
4.1	Atomic force micrographs of self-organised InGaAs rings.	55
4.2	Scenario of a diffusion-driven transformation from dots to rings.	56

4.3	Model of ring formation promoted by a wetting droplet instability.	57
4.4	AFM images of InAs islands for different overgrowth conditions.	58
4.5	AFM images of sample c10-530.	60
4.6	AFM images of sample c10-450.	61
4.7	AFM images of sample c03-530.	61
4.8	AFM images of sample c03-450.	62
4.9	GISAXS measurement of the sample c03-450.	64
4.10	GISAXS measurements for different azimuthal positions of sample c03-450. . .	64
4.11	Model used for the simulation of the GISAXS measurements.	65
4.12	Best fit for the GISAXS measurements shown in Fig. 4.10.	66
4.13	Form factor of a ring structure.	67
4.14	Radial measurement at the $(2\bar{2}0)$ Bragg reflection.	68
4.15	$q_{\text{rad}} - q_z$ mapping at the $(2\bar{2}0)$ Bragg reflection.	68
4.16	Radial measurement at the (220) Bragg reflection.	69
4.17	$q_{\text{rad}} - q_z$ mapping at the (220) Bragg reflection.	69
4.18	Angular measurement at the $(2\bar{2}0)$ Bragg reflection.	70
4.19	Angular measurement at the (220) Bragg reflection.	70
4.20	$q_{\text{rad}} - q_{\text{ang}}$ mapping at the $(2\bar{2}0)$ Bragg reflection.	71
4.21	$q_{\text{rad}} - q_{\text{ang}}$ mapping at the (220) Bragg reflection.	71
4.22	FEM model of the quantum ring structure.	72
4.23	FEM case study: change of the QR radius.	74
4.24	FEM case study: change of the InAs concentration in the dot rest.	75
4.25	FEM case study: change of the InAs concentration in the ring.	75
4.26	FEM simulation of the displacement field u_x assuming a high InAs concentration in the quantum ring.	77
4.27	FEM simulation of the displacement field u_x assuming a low InAs concentration in the quantum ring.	77
4.28	FEM simulation of the strain ϵ_{xx} assuming a high InAs concentration in the quantum ring.	77
4.29	FEM simulation of the strain ϵ_{xx} assuming a low InAs concentration in the quantum ring.	77
4.30	Best simulation for the radial measurement at the $(2\bar{2}0)$ Bragg reflection. . . .	79

4.31	Best simulation for the radial measurement at the (220) Bragg reflection.	79
4.32	Simulated $q_{\text{rad}} - q_z$ mapping at the ($2\bar{2}0$) Bragg reflection.	80
4.33	Simulated $q_{\text{rad}} - q_z$ mapping at the (220) Bragg reflection.	80
4.34	Simulated $q_{\text{rad}} - q_{\text{ang}}$ mapping at the ($2\bar{2}0$) Bragg reflection.	81
4.35	Simulated $q_{\text{rad}} - q_{\text{ang}}$ mapping at the (220) Bragg reflection.	81
4.36	Selected angular simulations at the ($2\bar{2}0$) Bragg reflection.	82
4.37	Selected angular simulations at the (220) Bragg reflection.	82
4.38	Summary of the quantum ring model.	83
5.1	Schematic overview of the cleaved edge overgrowth (CEO) sample preparation	86
5.2	Schematic view of a (classical) T-shaped quantum wire produced by CEO. . .	88
5.3	Schematic view of a purely strain modulated quantum wire produced by CEO.	89
5.4	Geometry of a strained CEO quantum wire.	89
5.5	Strain components for the quantum wire shown in Fig. 5.4.	90
5.6	Wave function for electron and hole levels in a QWR	90
5.7	Geometry of the investigated CEO sample.	91
5.8	AFM image of Ge grown on top of SiGe/Si strained QWs.	92
5.9	Sketch of the expected intensity distribution around the (002) and (220) Bragg reflections.	94
5.10	Schematic view of the investigated sample.	94
5.11	Experimental set-up - measurement at the (002) reflection.	95
5.12	Experimental set-up - measurement at the (220) reflection.	95
5.13	GID measurements of the cleaved edge at the (002) and (220) Bragg reflection.	97
5.14	Out of-plane XRD measurements of the (001) surface at the (002) and (220) Bragg reflection.	98
5.15	AFM image of the overgrown cleaved edge.	99
5.16	$q_{\text{long}} - q_z$ map at the (002) Bragg reflection in GID geometry	100
5.17	Slices along the q_z direction in Fig. 5.16.	101
5.18	In-plane strain component ε_{xx} calculated by FEM.	103
5.19	Strain component ε_{zz} perpendicular to the CEO surface calculated by FEM. .	103
5.20	In-plane displacement field u_x calculated by FEM.	104
5.21	Displacement field u_z perpendicular to the CEO surface calculated by FEM. . .	104

5.22 FEM calculation of the (001) component of the GaAs lattice parameter distribution in the CEO layer.	105
5.23 Model of a linear chain of atoms.	106
A.1 Shift of the Bragg position along α_f in grazing incidence diffraction.	112

Bibliography

List of publications

2003

- [Sztucki03a] *Strain analysis of a quantum-wire system produced by cleaved edge overgrowth using grazing incidence x-ray diffraction*,
M. Sztucki, T.U. Schüllli, T.H. Metzger, V. Chamard, R. Schuster, D. Schuh, Appl. Phys. Lett. **83**(5), 872-874 (2003) - article selected for publication in Virtual Journal of Nanoscale Science & Technology, August 11, 2003.
- [Sztucki03b] *Depth resolved investigations of boron implanted silicon*,
M. Sztucki, T.H. Metzger, S. Milita, F. Berberich, N. Schell, J.L. Rouvière, J. Patel, Nucl. Instrum. Methods B **200**, 52-59 (2003).
- [Schüllli03a] *Direct determination of strain and composition profiles in SiGe islands by anomalous x-ray diffraction at high momentum transfer*,
T.U. Schüllli, J. Stangl, Z. Zhong, R.T. Lechner, M. Sztucki, T.H. Metzger, G. Bauer, Phys. Rev. Lett. **90**(6), 066105 (2003) - article selected for publication in Virtual Journal of Nanoscale Science & Technology, February 24, 2003.
- [Chamard03a] *Anomalous diffraction in grazing incidence to study the strain induced by GaN quantum dots stacked in an AlN multilayer*,
V. Chamard, T.H. Metzger, M. Sztucki, M. Tolan, E. Bellet-Amalric, B. Daudin, C. Adelman, H. Mariette, Nucl. Instrum. Methods B **200**, 95-99 (2003).
- [Chamard03b] *On the driving forces for the vertical alignment in nitride quantum dot multilayers*,
V. Chamard, T.H. Metzger, M. Sztucki, V. Holý, M. Tolan, E. Bellet-Amalric, C. Adelman, B. Daudin, H. Mariette, Europhys. Lett. **63**(2), 268-274 (2003). 41

- [Chamard03c] *Strain distribution in nitride quantum dot multilayers*,
V. Chamard, T. Schüllli, M. Sztucki, T.H. Metzger, E. Sarigiannidou, J.-L. Rouvière, M. Tolan, C. Adelman, B. Daudin, Phys. Rev. B, accepted for publication (2003)
- [Jiang03] *Influence of Si spacer layers on the structures of Ge/Si quantum dot bilayers*,
X. Jiang, T.H. Metzger, M. Sztucki, Z. Jiang, W. Jiang, D. Xian, Nucl. Instrum. Methods B **200**, 40-45 (2003).
- 2002
- [Sztucki02] *X-ray analysis of temperature induced defect structures in Boron implanted Silicon*,
M. Sztucki, T.H. Metzger, I. Kegel, A. Tilke, D. Luebbert, J. Arthur, J. Patel, J.L. Rouvière, J. Appl. Phys. **92**(7), 3694-3703 (2002).
- [Luebbert02] *X-ray diffuse scattering study of the kinetics of stacking fault growth and annihilation in boron-implanted silicon*,
D. Luebbert, J. Arthur, M. Sztucki, T.H. Metzger, P.B. Griffin, J.R. Patel, Appl. Phys. Lett. **81**(17), 3167-3169 (2002).
- [Schüllli02b] *Anomalous x-ray diffraction on InAs/GaAs Quantum Dot systems*,
T. Schüllli, M. Sztucki, V. Chamard, T.H. Metzger, D. Schuh, Appl. Phys. Lett. **81**(3), 448-450 (2002).
- [Schüllli02a] *Anomalous X-ray Diffraction on InAs/GaAs Quantum Dot Systems*,
T.U. Schüllli, M. Sztucki, V. Chamard, D. Schuh, ESRF Highlights 2002.
- 2001
- [Metzger01] *The lifetime of defects in silicon after ion-implantation and annealing*,
T.H. Metzger, M. Sztucki, M. Servidori, ESRF Highlights 2001.
- 2000
- [Kegel00a] *Clusters and planar defects in boron implanted silicon an x-ray diffuse scattering study*,
I. Kegel, M. Sztucki, T.H. Metzger, D. Luebbert, J. Arthur, J.R. Patel, Mat. Res. Soc. Symp. Vol. **610**, B5.5.1 (2000).

Poster presentations

2003

- *Strain analysis of a quantum-wire system produced by cleaved edge overgrowth using grazing incidence x-ray diffraction*,
M. Sztucki, T.U. Schüllli, T.H. Metzger, V. Chamard, R. Schuster, D. Schuh,
ESRF, Experiments Division Students Day, Grenoble, October 2003

2002

- *GaAs matrix discrimination by anomalous x-ray diffraction in the quantum dot system InAs/GaAs*,
M. Sztucki, T.U. Schüllli, T.H. Metzger, D. Schuh, E. Beham,
E-MRS 2002 Spring Meeting, Strasbourg (France), 18-21 June 2002
- *The "lifetime" of defects in silicon after boron implantation and annealing*,
M. Sztucki, T.H. Metzger, J.-L. Rouvière, D. Lübbert, J. Patel,
ESRF, 13th Users Meeting, Grenoble, 10-14 February 2002

2001

- *Temperature induced defect structures in boron-implanted silicon investigated by modern x-ray methods and atomic force microscopy*,
M. Sztucki, T.H. Metzger, D. Lübbert, J. Arthur, J. Patel,
HERCULES course 2001 and 5th autumn school on "x-ray scattering from surfaces and thin layers", Smolenice (Slovakia), 12-15 September 2001

References

- [Allen87] L.T. Allen, E.R. Weber, J. Washburn, and Y.C. Pao, *Appl. Phys. Lett.* **51**, 670 (1987). 92
- [AlsNielsen01] J. Als-Nielsen and D. McMorrow, *Elements of modern X-ray physics*, Wiley, New York (2001) 7, 10, 15
- [Arai97a] J. Arai, N. Usami, K. Ota, Y. Shiraki, A. Ohga, and T. Hattori, *Appl. Phys. Lett.* **70**, 2981 (1997). 4, 85, 92, 108
- [Arai97b] J. Arai, A. Ohga, T. Hattori, N. Usami, and Y. Shiraki, *Appl. Phys. Lett.* **71**, 785 (1997). 92, 108
- [Asaro72] R.J. Asaro and W.A. Tiller, *Metall. Trans. A*, 1789 (1972). 3
- [Baró94] J. Baró, M. Roteta, J.M. Fernández-Varea, and F. Salvat, *Radiat. Phys. Chem.* **44**, 531 (1994). 11
- [Bayer03] M. Bayer, M. Korkusinski, P. Hawrylak, T. Gutbrod, M. Michel, and A. Forchel, *Phys. Rev. Lett.* **90**, 186801 (2003). 53
- [Bimberg98] D. Bimberg, M. Grundman, and N.N. Ledentsov, *Quantum Dot Heterostructures*. Wiley, Chichester (1998). 1, 4
- [Blossey02] R. Blossey and A. Lorke, *Phys. Rev. E* **65**, 021603 (2002). 53, 54, 55, 56, 57
- [Braess97] D. Braess, *Finite Elements - Theory, fast solvers and applications in solid mechanics*, Cambridge University Press (1997) 24
- [Brault98] J. Brault, M. Gendry, G. Grenet, G. Hollinger, Y. Desières, and T. Benyattou, *Appl. Phys. Lett.* **73**, 2932 (1998). 38, 56
- [BresslerHill92] V. Bressler-Hill, W. Wassermeier, K. Pond, R. Maboudian, G.A.D. Briggs, P.M. Petroff, and W.H. Weinberg, *J. Vac. Sci. Technol. B* **10**, 1881 (1992). 87
- [Bronstein] I.N. Bronstein, K.A. Semendjajew, G. Musiol, and H. Mühlig, *Taschenbuch der Mathematik*, Harri Deutsch, Thun. 107
- [Chang85] Y. Chang, L.L. Chang, and L. Esaki, *Appl. Phys. Lett.* **47**, 1324 (1985). 4, 88
- [Climente03] J.I. Climente, J. Planelles, and W. Jaskolski, *Phys. Rev. E* **68**, 075307 (2003). 53
- [Cowley81] J.M. Cowley, *Diffraction Physics*, North-Holland, Amsterdam (1981). 7

- [Creagh92] D.C. Creagh and W.J. McAuley, in *International Tables for Crystallography - Vol. C*, edited by A.J.C. Wilson, Kluwer Academic Publishers, Dordrecht (1992) 11
- [Crozier01] P.A. Crozier, M. Catalano, R. Cingolani, and A. Passaseo, *Appl. Phys. Lett.* **79**, 3170 (2001). 37
- [Cui03] J. Cui, Q. He, X.M. Jiang, Y.L. Fan, X.J. Yang, F. Xue, and Z.M. Jiang, *Appl. Phys. Lett.* **83**, 2907 (2003). 53, 54, 59
- [Darowski98] N. Darowski, U. Pietsch, U. Zeimer, V. Smirnitzki, and F. Bugge, *J. Appl. Phys.* **84**, 1366 (1998). 94
- [Dosch92] H. Dosch, *Critical phenomena at surfaces and interfaces. Evanescent X-ray and neutron scattering*, Springer, Berlin (1992). 7, 20
- [Fawcett94] P.N. Fawcett, J.H. Neave, J. Zhang, and B.A. Joyce, *J. Vac. Sci. Technol. A* **12**(4), 1201 (1994). 92
- [Ferdos02] F. Ferdos, S. Wang, Y. Wei, A. Larsson, M. Sadeghi, and Q. Zhao, *Appl. Phys. Lett.* **81**, 1195 (2002). 54, 58
- [Flocken70] J.W. Flocken and J.R. Hardy, *Phys. Rev. B* **1**, 2447 (1970). 30
- [Frank49] F.C. Frank and J.H. van der Merwe, *Proc. R. Society A* **198**, 205 (1949). 3
- [Garcia97] J.M. Garcia, G. Medeiros-Ribeiro, K. Schmidt, T. Ngo, J.L. Feng, A. Lorke, J.P. Kotthaus, and P.M. Petroff, *Appl. Phys. Lett.* **71**, 2014 (1997). 4, 53, 54
- [Gershoni90] D. Gershoni, J.S. Weiner, S.N.G. Chu, G.A. Baraff, J.M. Vandenberg, L.N. Pfeiffer, K. West, R.A. Logan, and T. Tanbun-Ek, *Phys. Rev. Lett.* **65**, 1631 (1990). 88
- [Gershoni91] D. Gershoni, J.S. Weiner, S.N.G. Chu, G.A. Baraff, J.M. Vandenberg, L.N. Pfeiffer, K. West, R.A. Logan, and T. Tanbun-Ek, *Phys. Rev. Lett.* **66**, 1375 (1991). 88
- [Goerigk03] G. Goerigk, H.G. Haubold, O. Lyon, and J.P. Simon, *J. Appl. Cryst.* **36**, 425 (2003). 83
- [Goering93] H. Goering, H.-G. Roos, and L. Tobiska, *Finite-Element-Method*, Akademie Verlag 3rd edition (1993). 24
- [Göni92] A.R. Göni, L.N. Pfeiffer, K.W. West, A. Pinczuk, H.U. Baranger, and H.L. Stormer, *Appl. Phys. Lett.* **61**, 1956 (1992). 4
- [Granados03a] D. Granados and J.M. Garcia, *Appl. Phys. Lett.* **82**, 2401 (2003). 58, 62
- [Granados03b] D. Granados and J.M. Garcia, *J. Cryst. Growth* **251**, 213 (2003). 58
- [Grinfeld86] M.A. Grinfeld, *Dokl. Akad. Nauk SSSR*, 1358 (1986). 3

- [Grundmann90] M. Grundmann, U. Lienert, J. Christen, D. Bimberg, A. Fischer-Colbrie, and J.N. Miller, *J. Vac. Sci. Technol. B* **8**, 751 (1990). 90
- [Grundmann97] M. Grundmann and D. Bimberg, *Phys. Rev. B* **55**, 4054 (1997). 4, 88
- [Grundmann00] M. Grundmann, O. Stier, A. Schliwa, and D. Bimberg, *Phys. Rev. B* **61**, 1744 (2000). 4, 85, 86, 89, 90, 91
- [Hackenbuchner02] S. Hackenbuchner, M. Sabathil, J.A. Majewski, G. Zandler, P. Vogl, E. Beham, A. Zrenner, and P. Lugli, *Physica B* **314**, 145 (2002). 108
- [Hajak03] H. Hajak, *Photolumineszenz- und Photolumineszenzanregungsspektroskopie der niedrigdimensionalen GaAs-basiertem Halbleiterstrukturen*, Diplomarbeit, Universität Regensburg (2003). 88, 89, 91
- [Hashizume95] T. Hashizume, Q.K. Xue, A. Ichimiya, and T. Sakurai, *Phys. Rev. B* **51**, 4200 (1995). 56
- [Heidemeyer02] H. Heidemeyer, S. Kiravittaya, C. Müller, N.Y. Jin-Phillipp, and O.G. Schmidt, *Appl. Phys. Lett.* **80**, 1544 (2002). 54, 58, 62
- [Henke93] B.L. Henke, E.M. Gullikson, and J.C. Davis, *At. Data Nucl. Data Tables* **54**, 181 (1993). 11
- [Herminghaus98] S. Herminghaus, K. Jacobs, K. Macke, J. Bischof, A. Fery, M. Ibn-Elhaj, and S. Schlagowski, *Science* **282**, 916 (1998). 56
- [Hesse02] A. Hesse, J. Stangl, V. Holý, T. Roch, G. Bauer, O.G. Schmidt, U. Denker, and B. Struth, *Phys. Rev. B* **66**, 085321 (2002). 5
- [Holmes98] D.M. Holmes, E.S. Tok, J.L. Sudijono, T.S. Jones, and B.A. Joyce, *J. Crystal Growth* **192**, 33 (1998). 87
- [Holý98] V. Holý, U. Pietsch, and T. Baumbach, *X-ray Scattering by Thin Films and Multilayers*, Springer-Verlag, Berlin (1998). 93, 94
- [Holý99] V. Holý, G. Springholz, M. Pinczolits, and G. Bauer, *Phys. Rev. Lett.* **83**, 356 (1999). 30, 41
- [Horikoshi90] Y. Horikoshi, H. Yamaguchi, F. Briones, and M. Kawashima, *J. Cryst. Growth* **105**, 326 (1990). 54, 63
- [Hsu03] C.H. Hsu, H.Y. Lee, Y.W. Hsieh, Y.P. Stetsko, M.T. Tang, K.S. Liang, N.T. Yeh, J.I. Chyi, and D.Y. Noh, *Physica B* **336**, 98 (2003). 37
- [Ice90] G.E. Ice and C.J. Sparks, *Nucl. Instrum. Methods A* **291**, 110 (1990). 21
- [Ishikuro97] H. Ishikuro, T. Hiramoto, *Appl. Phys. Lett.* **71**, 3691 (1997). 1
- [Joyce98] P.B. Joyce, T.J. Krzyzewski, G.R. Bell, B.A. Joyce and T.S. Jones, *Phys. Rev. B* **58**, 15981 (1998). 37, 56

- [Joyce01a] P.B. Joyce, T.J. Krzyzewski, P.H. Steans, G.R. Bell, J.H. Neave, and T.S. Jones, *Surf. Sci.* **492**, 345 (2001). 55
- [Joyce01b] P.B. Joyce, T.J. Krzyzewski, G.R. Bell, and T.S. Jones, *Appl. Phys. Lett.* **79**, 3615 (2001). 54, 62
- [Kamiya99] I. Kamiya, I. Tanaka, and H. Sakaki, *J. Cryst. Growth* **201/202**, 1146 (1999). 54, 58
- [Kegel00b] I. Kegel, *X-ray diffraction from semiconductor quantum dots*, PhD thesis, Ludwig Maximilians University in Munich (2000). 78, 111
- [Kegel01] I. Kegel, T.H. Metzger, A. Lorke, J. Peisl, J. Stangl, G. Bauer, K. Nordlund, W.V. Schoenfeld, and P.M. Petroff, *Phys. Rev. B* **63**, 035318 (2001). 5, 15, 42, 52, 67, 78, 109
- [Kim98] E.S. Kim, N. Usami, and Y. Shiraki, *Appl. Phys. Lett.* **72**, 1617 (1998). 108
- [Kim99] E.S. Kim, N. Usami, and Y. Shiraki, *Semicond. Sci. Technol.* **14**, 257 (1999). 108
- [Kissel95] L. Kissel, B. Zhou, S.C. Roy, S.K. Sen Gupta, R.H. Pratt, *Acta Cryst. A* **51**, 271 (1995). 11
- [Kitajima01] T. Kitajima, B. Liu, and S.R. Leone, *Appl. Phys. Lett.* **80**, 497 (2001). 108
- [Krenner02] H.J. Krenner, A. Zrenner, M. Bichler, and G. Abstreiter, *Proc. 26th ICPS 2002* 38, 40
- [LaBella99] V.P. LaBella, H. Yang, D.W. Bullock, P.M. Thibado, P. Kratzer, and M. Scheffler, *Phys. Rev. Lett.* **83**, 2989 (1999). 56
- [Lazzari02] R. Lazzari, *J. Appl. Cryst.* **35**, 406 (2002). 65
- [Lee98] J.S. Lee, H.W. Ren, S. Sugou, and Y. Masumoto, *J. Appl. Phys.* **84**, 6686 (1998). 54, 58
- [Lequien94] S. Lequien, L. Goirand, and F. Lesimple, *Rev. Sci. Instrum.* **66**, 1725 (1995). 16
- [Liu00] N. Liu, J. Tersoff, O. Baklenov, A.L. Holmes, Jr., and C.K. Shih, *Phys. Rev. Lett.* **84**, 334 (2000). 4, 37
- [Lorke98] A. Lorke and R.J. Luyken, *Physica B* **256-258**, 424 (1998). 53, 54
- [Lorke00] A. Lorke, R.J. Luyken, A.O. Govorov, and J.P. Kotthaus, *Phys. Rev. Lett.* **84**, 2223 (2000). 53, 54
- [Lorke01] A. Lorke, R.J. Luyken, J.M. Garcia, and P.M. Petroff, *Jpn. J. Appl. Phys.* **40**, 1857 (2001). 53, 54, 55, 56

- [Lorke02] A. Lorke, R. Blossey, J.M. Garcia, M. Bichler, and G. Abstreiter, *Mat. Sci. Eng. B* **88**, 225 (2002). 53, 54, 55, 62
- [Lorke03] A. Lorke, J.M. Garcia, R. Blossey, R.J. Luyken, and P.M. Petroff, *Adv. Solid State Phys.* **43**, 125 (2003). 4, 54, 55, 56
- [Loss98] D. Loss and D.P. DiVincenzo, *Phys. Rev. A* **57**, 120 (1998). 1, 37
- [Love44] A.E.H. Love, *A treatise on the mathematical theory of elasticity*, Dover Publications, New York (1944). 24
- [Madelung92] O. Madelung, *Data in Science and Technology: Semiconductors Group IV Elements and III-V Compounds*, Springer, Berlin (1992). 34
- [Materlik94] G. Materlik, C.J. Sparks, and K. Fisher, *Resonant Anomalous X-ray Scattering: Theory and Applications*, North-Holland, Amsterdam (1994). 10
- [Mayer01] P. Mayer, *Finite-element calculation of the elastic relaxation in PbSe quantum dots and quantum dot superlattices*, Diploma thesis, University of Linz (2001). 29, 30
- [Moriarty01] P. Moriarty, *Rep. Prog. Phys.* **64**, 297 (2001). 4
- [nextnano] nextnano³ device simulation package, see website <http://www.nextnano.de> 108
- [Okada01] H. Okada and H. Hasegawa, *Jpn. J. Appl. Phys. Part 1* **40** (4B), 2797 (2001). 1
- [Pettersson00] H. Pettersson, R.J. Warburton, A. Lorke, K. Karrai, J.P. Kotthaus, J.M. Garcia, and P.M. Petroff, *Physica E* **6**, 510 (2000). 53, 54
- [Pfeiffer90] L. Pfeiffer, K.W. West, H.L. Stormer, J.P. Eisenstein, K.W. Baldwin, D. Gershoni, and J. Spector, *Appl. Phys. Lett.* **56**, 1697 (1990). 4, 85, 86, 87
- [Pryor98] C. Pryor, J. Kim, L.W. Wang, J. Williamson, and A. Zunger, *J. Appl. Phys.* **83**, 2548 (1998). 30
- [Raz03] T. Raz, D. Ritter, and G. Bahir, *Appl. Phys. Lett.* **82**, 1706 (2003). 53, 54, 58
- [Regelman99] D.V. Regelman and D. Gershoni, 24th International Conference on the Physics of Semiconductors (ICPS24), Jerusalem, Israel, August 2-7, 1998. in "The Physics of Semiconductors", Editor D. Gershoni, World Scientific Publishing Co. 1999. 4, 85, 89, 90
- [Rhan96] H. Rhan, J. Peisl, *Z. Phys. B* **100**, 365 (1996). 112
- [Rio98] M. Sánchez del Río, M. Gambaccini, G. Pareschi, A. Taibi, A. Tuffanelli, and A. Freund, *Proceedings SPIE*, Vol. **3448**, 246 (1998). 21, 22

- [Rosenauer00] A. Rosenauer, W. Oberst, D. Litvinov, and D. Gerthsen, Phys. Rev. B **61**, 8276 (2000). 37
- [Sabathil02] M. Sabathil, S. Hackenbuchner, J.A. Majewski, G. Zandler, and P. Vogl, Journal of Computational Electronics **1**, 81 (2002). 108
- [Schedelbeck97] G. Schedelbeck, W. Wegscheider, M. Bichler, and A. Abstreiter, Science **278**, 1792 (1997). 88
- [Schmidbauer03] M. Schmidbauer, *X-ray diffuse scattering from Self-organized Mesoscopic Semiconductor Structures*, Springer (2003). 24
- [Schmidt00] O.G. Schmidt, N.Y. Jin-Phillipp, C. Lange, U. Denker, K. Eberl, R. Schreiner, H. Gräbeldinger, and H. Schweizer, Appl. Phys. Lett. **77**, 4139 (2000). 108
- [Schmidt02] O.G. Schmidt, S. Kiravittaya, Y. Nakamura, H. Heidemeyer, R. Songmuang, C. Müller, N.Y. Jin-Phillipp, K. Eberl, H. Wawra, S. Christiansen, H. Gräbeldinger, and H. Schweizer, Surf. Sci. **514**, 10 (2002). 108
- [Schuh03] D. Schuh, personal communication. 93
- [Schüllli03b] T.U. Schüllli, *Anomalous X-ray Diffraction from Semiconductor Nanostructures*, Dissertation, Universität Linz (2003). 5
- [Schuster03] R. Schuster, personal communication. 91
- [Shahid88] M.A. Shahid and S. Mahajan, Phys. Rev B **38**, 1344 (1988). 13
- [Sokolnikoff56] I.S. Sokolnikoff, *Mathematical theory of elasticity*, MacGraw-Hill, New York (1956). 24
- [Songmuang03] R. Songmuang, S. Kiravittaya, and O.G. Schmidt, J. Cryst. Growth **249**, 416 (2003). 54, 58
- [Srolovitz89] D.J. Srolovitz, Acta Metall. **37**, 621 (1989). 3
- [Stangl01] J. Stangl, A. Daniel, V. Holý, T. Roch, G. Bauer, I. Kegel, T.H. Metzger, Th. Wiebach, O.G. Schmid, and K. Eberl, Appl. Phys. Lett. **79**, 1474 (2001). 5
- [Stranski38] I.N. Stranski, L. Krastanov, *Sitzungsbericht der Akademie der Wissenschaften in Wien, Abt. IIb, Chemie* **146**, 797 (1938). 3
- [Sudijono92] J. Sudijono, M.D. Johnson, C.W. Snyder, M.B. Elowitz, and B.G. Orr, Phys. Rev. Lett. **69**, 2811 (1992). 38, 56
- [Takehana03] K. Takehana, F. Pulizzi, A. Patane, M. Henini, P.C. Main, L. Eaves, D. Granados, and J.M. Garcia, J. Cryst. Growth **251**, 155 (2003). 54, 58
- [Teichert02] C. Teichert, Physics Reports **365**, 335 (2002). 4

- [Ulyanenkov99] A. Ulyanenkov, N. Darowski, J. Grenzer, U. Pietsch, K.H. Wang, and A. Forchel, Phys. Rev. B **60**, 16701 (1999). 93, 94
- [Usami98] N. Usami, J. Arai, E.S. Kim, K. Ota, T. Hattori, and Y. Shiraki, Physica E **2**, 137 (1998). 4, 85, 92, 108
- [Vegard21] L. Vegard, Zeit. f. Physik **5**, 17 (1921). 2, 46
- [Vlieg97] E. Vlieg, J. Appl. Cryst. **30**, 532 (1997). 16
- [Volmer26] M. Volmer and N. Weber, Z. Phys. Chem. **119**, 227 (1926). 3
- [Walther01] T. Walther, A.G. Cullis, D.J. Norris, and M. Hopkinson, Phys. Rev. Lett. **86**, 2381 (2001). 37
- [Warren69] B.E. Warren, *X-ray diffraction*, Dover, New York (1969). 7, 9
- [Warburton00] R.J. Warburton, C. Schäflein, D. Haft, F. Bickel, A. Lorke, K. Karrai, J.M. Garcia, W. Schoenfeld, and P.M. Petroff, nature **405**, 926 (2000). 53
- [Wassermeier94] M. Wassermeier, H. Yang, E. Tournie, L. Daeweritz, and K. Ploog, J. Vac. Sci. Technol. **B 12**(4), 2574 (1994). 92
- [Wegscheider93] W. Wegscheider, L.N. Pfeiffer, M.M. Dignam, A. Pinczuk, K.W. West, S.L. McCall, and R. Hull, Phys. Rev. Lett. **71**, 4071 (1993). 88
- [Wegscheider97a] W. Wegscheider, L.N. Pfeiffer, K.W. West, A.A. Kiselev, M. Hagn, R.E. Leibenguth *Optical Spectroscopy of Low Dimensional Semiconductors*, 127, Kluwer Academic Publishers (1997). 87
- [Wegscheider97b] W. Wegscheider, G. Schedelbeck, G. Abstreiter, M. Rother, and M. Bichler, Phys. Rev. Lett. **79**, 1917 (1997). 4, 87, 88
- [Wegscheider97c] W. Wegscheider, G. Schedelbeck, M. Bichler, and G. Abstreiter, Phys. Stat. Sol. (a) **164**, 601, (1997). 4, 86, 87, 88
- [Wegscheider98] W. Wegscheider, G. Schedelbeck, M. Bichler, and G. Abstreiter, Physica E **3**, 103 (1998). 4, 87, 88
- [Xie94] Q. Xie, P. Chen, and A. Madhukar, Appl. Phys. Lett. **65**, 2051 (1994). 55
- [You99] H. You, J. Appl. Cryst. **32**, 614 (1999). 16
- [Zener55] *Élasticité et anélasticité des métaux*, Dunod, Paris (1955). 24
- [Zhu99] J.H. Zhu, K. Brunner, and G. Abstreiter, Appl. Phys. Lett. **73**, 620 (1999). 108
- [Zienkiewicz87] O. Zienkiewicz, R. Taylor, *The finite-element method*, McGraw-Hill (1987). 24



©Werner Konrad Mayer (Dissertation), 1981

Acknowledgements

I would like to acknowledge here the important contributions that many people have made over the last years which have allowed me to get where I am today. In particular, I like to thank

- **Dr. Till Hartmut Metzger** as my direct supervisor and responsible for the beamline ID1 at the ESRF in Grenoble for his continuous support, for sharing his experimental knowledge during several beamtimes, for the time and energy he invested in countless fruitful discussions, and for the nice atmosphere in his group. Last, but not least I'd like to thank him for the first contact with this nice place in the French alps during a first beamtime in 1999.
- **Prof. Dr. Jörg P. Kotthaus** as professor of the semiconductor group at the Ludwig Maximilians university in Munich, that he agreed to supervise my thesis and for his continuous interest in the progress of my work.
- **Prof. Dr. Václav Holý**, professor at the Masaryk university in Brno, Czech Republic, for the theoretical support of this thesis and for providing several useful Fortran simulations (incl. their quick adaptation to my problems).
- **Prof. Dr. Günther Bauer** for the hospitality at the institute of semiconductor physics at the Johannes Kepler university in Linz, Austria during three weeks in spring 2002. In addition, he made it possible to perform the finite-element calculations at the computer centre in Linz.
- **Anke Hesse** for the introduction into finite-element calculations and for providing the necessary FEM input scripts. Moreover, I'd like to thank her, **Ulrich Denker** and all people of the semiconductor physics division for the productive and nice time in Linz.
- **Robert Schuster**, **Dieter Schuh**, and **Evelin Beham** for the fruitful collaboration in the framework of SFB348, especially for providing the CEO and quantum dot samples.
- **Dr. Winston Schoenfeld** at the University of California, Santa Barbara, USA for providing the quantum ring samples.
- **Dr. Virginie Chamard** for the productive collaboration and her support during two important beamtimes.
- **Dr. Tobias Schüllli**, **Dr. Bärbel Krause**, **Angelo Malachias**, and **Luciana Capello** for the nice atmosphere in our office and for interesting discussions concerning the interpretation of the measurements.

- **Dr. Bruno Jean, Dr. Olivier Plantevin, Dr. Peter Bösecke, Dr. Angel Mazuelas, Dr. Cristian Mocuta, Dr. Myles Hamilton, Hamid Djazouli, Francis Lesimple, Roland Taffut, and David Fernandez** as my colleagues for the pleasant working climate and for intellectual and technical assistance at the beamline.
- **Dr. Samantha Warren** for the first proof-reading of this thesis.
- Deutsche Forschungsgemeinschaft under **SFB 348** and the **ESRF** for their funding.
- **my parents** who made my studies possible and constantly encouraged me, despite living more than 700km away.

Curriculum Vitae

MICHAEL SZTUCKI

born in Augsburg, Germany, on June 29th, 1974

Primary education

1981 - 1985 Elementary school, Augsburg

Secondary education

1985 - 1994 Gymnasium bei St. Stephan, Augsburg

1994 Abitur

Civil service

1994 - 1995 Bayerisches Rotes Kreuz (emergency medical services), Augsburg

University

1995 - 2000 Ludwig Maximilians University, Munich

1997 *Vordiplom* in Physics

Jan. 2001 *Diplom* in Physics (thesis: *The "lifetime" of defects in silicon after boron implantation and annealing.*)

Doctoral degree

2001 - 2004 PhD thesis at the European Synchrotron Radiation Facility (beamline ID1), Grenoble, France
as an employee of the Ludwig Maximilians University in Munich